

TEMPERATURE AND FORCE MODELING ON GRINDING

by

MERT KOCAEFE

Submitted to the Graduate School of Engineering and Natural Sciences
in partial fulfillment of
the requirements for the degree of
Master of Science

Sabanci University
January 2017

TEMPERATURE AND FORCE MODELING ON GRINDING

APPROVED BY:

Prof.Dr. Erhan Budak
(Thesis Supervisor)



Assoc. Prof.Dr. Bahattin Koç



Asst. Prof.Dr. Umut Karagözel



DATE OF APPROVAL:

05.01.2017

© Mert Kocaefe 2017

All Rights Reserved

To my family

ABSTRACT

Grinding operations are commonly used in machining industry as they offer high precision level for applications such as increasing the surface quality of parts, and even machining of hard alloy in the aviation and space technology, automotive, biomedical equipment and electronics. Super abrasive grinding operations has gained importance through increasing usage of super alloys in these sectors. Excessive temperature rise occurs on workpiece during hard metal grinding, which can cause residual stresses, micro cracks, surface burns etc. Process modeling is crucial for examining these effects to control them within optimization of grinding parameters in less costly and less time consuming way. Investigation of grinding operations has been held by researchers since the industrial revolution, and it became state of the art with its stochastic nature. At present there is no suitable method to identify process temperature and forces without calibration and experimental data. The advantage of these studies is that consistent model results according to the calibrated data, but nevertheless, the wide range of adaptability remained limited. The goal of this thesis is to define the geometrical identification of grinding operations and usage of these into thermomechanical and temperature modeling of the process as a whole model to reduce dependence on calibration via experimental data. In this content, the hypotheses of this study are that temperature calibration on the thermomechanical model can be solved via iteratively with the calculation of attained and resultant temperature values in it. Furthermore, geometrical approaches for wheel and grain geometry is crucial to develop comprehensible force and temperature modeling. Temperature and force parameters were investigated by the established models and experimental data. After all, comprehensive process models were established for wide range of usage. This thesis is divided into four chapters in these directions; starting with the geometrical investigation and followed by force modeling and temperature modeling and finally a review of them in the experimental verifications and discussions.

Keywords: Surface grinding, Thermomechanical Force Model, 3D Temperature Distribution Model, Grinding Geometry

ÖZET

Taşlama operasyonları metal işleme endüstrisinde yüzey kalitesini arttırmak ve yüksek hassasiyet için kullanılmaktadır. Son yıllarda sert metallerin işlenmesi için de süper aşındırıcı taşlama operasyonları kullanılmaya başlanmıştır. Havacılık, uzay, otomotiv, biyomedikal ve elektronik endüstrilerinde süperalaşımın kullanımının artması ile taşlama operasyonu da önem kazanmıştır. Sert metallerin taşlama operasyonları ile işlenmesi sırasında iş parçası üzerinde çok yüksek ısı kalmaktadır, bu da kalıntı gerilmelere, yüzey yanıklarına, mikro çatlaklara ve malzeme yapısının değişmesine neden olabilmektedir. Proses modelleme bu etkilerin incelenmesi ve operasyonun daha düşük maliyetle ve daha kısa sürede iyileştirilebilmesi için son derece önemlidir. Taşlama operasyonlarının incelenmesi sanayi devriminden bu yana bir çok araştırmacı tarafından yapıldı ve skotastik doğası ile başlı başına bir dal haline geldi. Literatürdeki bir çok model kalibrasyon ve test datalarına bağlı bir aralıkta çalışmaktadır. Taşlama operasyonunun artan takım ve iş parçası çeşitliliği ile bu modellerin kullanımı kısıtlı kalmaktadır. Bu tezin amacı geometrik olarak incelenebilen bir takımın kurulan geometrik, termomekanik ve sıcaklık modeller ile proses parametrelerinin belirlenmesi ve böylece kalibrasyon ve testlere bağlılığının azaltılmasıdır. Bu bağlamda, bu çalışmada öne sürülen hipotez termomekanik modelde kullanılan sıcaklık değerinin kurulan modeller yardımıyla iteratif olarak çözülüp kalibrasyon ve test parametrelerinin azaltılabileceğidir. Bunun yanı sıra, geometrik inceleme ve modelleme proses modellerinin çalışması için son derece önemlidir. Kurulan modeller ve yapılan ölçümlerle sıcaklık ve kuvvet değerleri incelenmiş ve geniş kapsamlı bir proses modeli oluşturulmuştur.

Anahtar Kelimeler: Satıh Taşlama, Termomekanik Kuvvet Modeli, 3D Sıcaklık Dağılımı Modeli, Taşlama Geometrisi

ACKNOWLEDGEMENTS

It was a challenging and intense learning period for me not only in scientific area, but also on a personal perspective. This thesis process had a large impact on me with working and living at Sabancı University, both scientifically and socially. I would like to appreciate the people who have supported and helped me throughout this period.

I would like to address my thanks to Prof. Dr. Erhan Budak, who has patiently guided me to complete this dissertation. I would like to thank to Dr. Emre Özlü for his participations in this thesis. I would also like to thank the members of my committee: Dr. Mustafa Bakkal, Dr. Bahattin Koç.

I would also like to appreciate the assistance of the Maxima R&D members, Suleyman Tutkun, Erugtul Sadıkoğlu, Veli Nakşiler, Esmâ Baytok, Anıl Sonugür, Ahmet Ergen, Tayfun Kalender, and Dilara Albayrak. Their assistance and experience on the field make it easier to overcome problems.

I would like to thank each member of the manufacturing research laboratory family for their friendships, collaboration and help: Especially to grinding team as Batuhan Yastıkçı, Mert Gürtan and Hamid Jamshidi. I would also like to thank other friends; Cihan Özener, Ekrem Can Unutmazlar, Samet Bilgen, Gözde Bulgurcu, Turgut Köksal Yalçın, Mehmet Albayrak, Emre Uysal, Muhammad Hassan Yaqoob, Milad Azvar, Esra Yüksel, Kaveh Rahimzadeh, Amin Bagherzadeh, Faraz Tehranizadeh, Zahra Barzegar for their opinions and shares.

Finally, I also would like to thank to Sabancı University Subaqua Society members, especially to Alper Gül. Without their moral supports and friendships, my social life would have never been that great during this thesis study.

At last but not the least, I am most thankful to my parents Aziz and Naciye, and to my dear sister Merve for their great guidance, supports, patience and sacrifices during this study.

TABLE OF CONTENTS

1	INTRODUCTION	8
1.1	Introduction and Literature Survey	8
1.2	Objective	14
1.3	Layout of the Thesis	16
2	GEOMETRIC APPROACH AND MODELS FOR SURFACE GRINDING	17
3	THERMO-MECHANICAL FORCE MODEL FOR SURFACE GRINDING	30
3.1	Mechanistic and semi analytical force model	32
3.2	Thermomechanical force model	35
3.2.1	Oblique Thermomechanical Force Model	36
3.2.2	Edge Forces Thermomechanical Force Model	42
3.2.3	Grinding Application of Thermomechanical Force Model	49
4	3D TEMPERATURE DISTRIBUTION MODEL ON WORKPIECE WITH MOVING HEAT SOURCE	54
4.1	Heat Partitioning Model on Grinding	58
4.2	Temperature Distribution Model	63
4.2.1	Stationary Point Heat Source Model	63
4.2.2	Moving Heat Source Model for Point Heat Source	65
4.2.3	Heat Flux Model into Temperature Distribution	68
5	MODEL DISCUSSION AND EXPERIMENTAL VERIFICATION	73
5.1	Model Discussion	73
5.1.1	Calibration of material model parameters	75
5.1.2	Calibration of sliding & sticking friction coefficients	75
5.1.3	Shear angle rake angle predictions	77
5.1.4	Temperature effect on shear zone	78
5.1.5	Temperature full solution in 3D	81
5.1.6	Experimental Setups	84
5.1.7	Grain Measurements & Grinding Wheels Parameters	90
5.2	Experimental Force Verification	96
5.2.1	Experimental Temperature Verification	102
6	SUGGESTIONS FOR FURTHER RESEARCH	108
7	RESULTS AND DISCUSSIONS	109
8	CONCLUSIONS	112
	APPENDICES	120
	APPENDIX A – Active grain percentage with random grain distribution	120
	APPENDIX B – Force vibration for grinding	122

LIST OF FIGURES

Figure 1: Basic geometry of the chip formation on grinding	18
Figure 2: 2D Z-Map for grinding with trochoidal kinematic [65].....	19
Figure 3: Kinematic path of grinding	20
Figure 4: Chip contact length and chip thickness on Z-map technique [69]	22
Figure 5: Simulated grain paths over workpiece	23
Figure 6: Simulation results for surface roughness and literature comparison.....	24
Figure 7: Simulation of uncut chip thickness vs. depth of cut.....	25
Figure 8: Instantaneous uncut chip thickness comparison for low r/ae ratio.....	25
Figure 9: Instantaneous uncut chip thickness comparison for high r/ae ratio	26
Figure 10: Contact length analysis.....	27
Figure 11: Maximum uncut chip thickness analysis.....	27
Figure 12: Surface roughness analysis.....	28
Figure 13: Grit properties vs. surface roughness	29
Figure 14: Single grit interaction & cutting schematic [71]	31
Figure 15: Schematic illustration of the process forces and chip formation in cutting [74].	32
Figure 16: Schematic illustration of oblique cutting [41].....	33
Figure 17: Illustration of cutting geometry	37
Figure 18: Illustration of oblique cutting geometry [40]	38
Figure 19: Sample shear angle estimation	41
Figure 20: Edge force model on rake face with geometrical illustrations	43
Figure 21: Grinding wheel illustration on cutting (a) operational image (b) uncut chip.....	50
Figure 22: Uncut chip thickness illustration (a) side view (b) section view.....	51
Figure 23: Uncut chip thickness illustration with exaggerated time interval	51
Figure 24: Force distribution to absolute coordination during immersion angle effect	52
Figure 25: Grain distribution illustration on per area	53
Figure 26: Temperature distribution for conventional machining [87]	55
Figure 27: Heat generation during grinding [88].....	56
Figure 28: Triangular heat source illustration [52].....	57
Figure 29: Grain-workpiece contact illustration during heat partitioning [22]	59
Figure 30: AL2O3 vs. AISI1050 heat partitioning simulation with different depth of cut ..	61
Figure 31: CBN vs. AISI1050 heat partitioning simulation with different depth of cut	61
Figure 32: CBN vs. AISI1050 heat partitioning simulation with different spindle speed....	62
Figure 33: Moving coordination system in x direction.....	65
Figure 34: Moving point heat source simulation	67
Figure 35: Heat flux distribution on moving coordinate system	68
Figure 36: Uniform heat source distribution.....	69
Figure 37: Triangular heat distribution	70
Figure 38: Heat distribution with triangular heat source considering one thermocouple.....	70
Figure 39: Heat distribution model inspired by Malkin reverse engineering study	71
Figure 40: 3D temperature distribution on workpiece considering z=0	72

Figure 41: Working diagram of the models.....	74
Figure 42: Sticking friction angle vs. cutting speed	76
Figure 43: Shear angle vs. rake angle	77
Figure 44: Effect of initial temperature on forces for thermomechanical model	78
Figure 45: The error ratio for attained and calculated temperature values	80
Figure 46: Temperature calculation and estimation graph	80
Figure 47: Simulated temperature for different x position	81
Figure 48: Simulated temperature for different depth beneath the surface	82
Figure 49: 3D temperature simulation of the workpiece	82
Figure 50: Filtered temperature measurement for the grinding condition.....	83
Figure 51: CNC grinding machine.....	84
Figure 52: NanoFocus surface topography measurement equipment (a) small wheel holder (b) large wheel holder.....	85
Figure 53: Workpiece design (a) section view for thermocouple holes (b) produced workpiece	86
Figure 54: Assembly of the workpiece on dynamometer	86
Figure 55: Thermocouple fixation with syringe	87
Figure 56: Thermal camera -FLIR.....	88
Figure 57: Thermal data acquisition system (a) Device Configuration (b) Device	88
Figure 58: Dynamometer	89
Figure 59: 3D scanned grain images.....	91
Figure 60: Exaggerated image of grain on cutting	91
Figure 61: Illustrated grain geometry (a) width and oblique angle (b) height, rake angle and edge radius.....	92
Figure 62: Sample program interface and analysis display	92
Figure 63: Rake angle investigation on histogram	93
Figure 64: Conventional wheels 01,02,03	94
Figure 65: CBN wheels 01,02,03.....	95
Figure 66: Sample force measurement	96
Figure 67: The comparison of grinding forces with CONV01 with wheel speed 23,04 m/s and workpiece velocity (a) 0,0083 m/s (b) 0,0166 m/s	97
Figure 68: The comparison of grinding forces with CONV02 with wheel speed 15,7 m/s and workpiece velocity (a) 0,0083 m/s (b) 0,0166 m/s	97
Figure 69: The comparison of grinding forces with CONV03 with wheel speed 15,7 m/s and workpiece velocity (a) 0,0083 m/s (b) 0,0166 m/s	98
Figure 70: Error comparison of different wheels' forces with 0,083 mm/s feed and different depth of cut.....	98
Figure 71: The comparison of grinding forces with CBN01 with wheel speed 53,19 m/s and depth of cut 100 μ m on Inconel718 (a) Forces at different workpiece velocity (b) Error comparison	99
Figure 72: The comparison of grinding forces with CBN02 with wheel speed 13,49 m/s and depth of cut 100 μ m on Inconel718 (a) Forces at different workpiece velocity (b) Error comparison	99

Figure 73: The comparison of grinding forces with CBN03 with wheel speed 15,08 m/s and feed 150 mm/min on AISI1050 Steel (a) Forces at different depth of cut (b) Error comparison	100
Figure 74: Error histogram between proposed model and experiments in normal forces ..	101
Figure 75: Error histogram between proposed model and experiments in tangential forces	101
Figure 76: Thermal camera calibration.....	102
Figure 77: Sample thermal camera measurement along with force measurement	102
Figure 78: Thermocouple measurements raw data	103
Figure 79: Heat flow comparison between experimental and model base calculations	103
Figure 80: Comparison of CBN01 with Inconel 718 Temperature measurements and predictions	104
Figure 81: Comparison of CBN03 with AISI1050 temperature measurements and predictions	105
Figure 82: Temperature distribution at various z depth beneath surface.....	105
Figure 83: Comparison of different workpieces and wheels for temperature	106
Figure 84: Error histogram between proposed model and experiments in temperature	107
Figure 85: Active Grain Percentage vs Feed	120
Figure 86: Active Grain Flow Chart	121
Figure 87: Force vibration flow chart	122
Figure 88: Dynamic properties	122
Figure 89: Force vibration on force and deflection	123
Figure 90: Dynamic properties	123
Figure 91: Force vibration on force and deflection	124

LIST OF TABLES

Table 1 Grinding simulation parameters	24
Table 2: Thermal properties of workpieces and tools.....	60
Table 3: Grinding conditions for model investigations	74
Table 4: Johnson-Cook material model parameters	75
Table 5: Sliding friction equations for different materials	76
Table 6: Iteration data for initial temperature prediction.....	79
Table 7: Mechanical and thermal properties of typical grain materials	94
Table 8: Geometrical properties of conventional wheels	94
Table 9: Geometrical properties of grains on conventional wheels.....	95
Table 10: Geometrical properties of CBN wheels.....	95
Table 11: Geometrical properties of grains on CBN wheels	95

1 INTRODUCTION

1.1 Introduction and Literature Survey

Victor Hugo thought that the patterns created by the movement of sand grains were responsible for the shape and feel of the natural world in which we live. Now, small hard particles play an important role in today's industry, and one of them is abrasive technology. Abrasive operations are one of the oldest known methods of physical deformation with the shaping of a softer material with harder material by rubbing each other to increase the sharpness of it. Nowadays, grinding tools such as aluminum oxide, silicon carbide, boron nitride and diamond have been used for abrasive operations in all sectors where high precision production is requirement such as aviation, automotive, electronics and biomedical. As in every machining processes, grinding has advantages and disadvantages as high precision along with high temperature on the workpiece. The low cutting tool costs and high surface quality are prominent reasons for the wide range of usage of them. As a matter of fact, there is a number of grinding tools for the operations in different performance and price range. For example, super-abrasive tools can be used for supper alloy grinding, but their prices are higher comparatively to conventional tools.

The use of superalloy materials, which are usually nickel based metalloids and non-metals alloys, increasing with the developing technologies. CBN abrasive wheels provide an ideal solution for machining of super alloys thanks to high hardness, thermal conduction and abrasion resistance properties [1] [2]. High temperature increase occurs during grinding of exceeding strength and tough materials, since the requirement of specific energy relatively higher [3] [4]. Prediction of the force and temperature values during grinding of such materials is essential regarding operation efficiency. Many techniques and applications were

used for selection of these in the industry mostly with trial and error methods, and improvement these techniques has been seen as both costly and time-consuming. It has no difference in metal machining either, and even more in grinding operations due to nature of it. The aim of this work is to predict process parameters as force and temperature and output parameter surface roughness, which are the basis of these optimizations within mathematical considerations.

In general, machining operations modeling start with the geometric representation to obtain physical conditions and the mechanical interactions. Grinding operation geometry begins with the grinding wheel, which includes hard abrasive grains with sharp edges in random geometric properties. Different type of abrasives could be attached to grinding wheels in many ways, but we could assume that they are randomly distributed cutting tool on a circular wheel [5]. The randomness of the locations and shapes of the grits leads to grinding operations as a complicated manufacturing process. In historical view, the majority of grinding models has been constructed on the empirical relations.

Empirical equations has been used by many researchers based on the main grinding parameters as spindle speed, depth of cut, feed rate, and equivalent diameter of the wheel [6] [7]. After all surface roughness, grinding energy, the geometry of the workpiece, wheel wear, and chatter models could be conducted in quantitative relations [8] [9]. Shaw and Malkin aggregate fundamental models for grinding operations [10] [11]. Drawbacks of working with an empirical model are; limited ranges and a requirement of adapting for each different combination of workpiece and wheel materials, and cutting conditions. Hunting up the best conditions means lots of test within costly and time-consuming by this way. Way out is modeling all the process kinematics and mechanics to create faster and cheaper solutions in a variety of grinding configurations.

It is easy to say that construct analytical model of grinding operation has assumptions since material of the workpiece is assumed isotropic instead of anisotropic as in real, and the random structure of the grits are reconstructed in geometrical representation with simplifications [12]. Finite element models can offer more consistent results compare to analytical one with constructing better material models and physical interaction in the

process, albeit it takes almost one month to compute one combination of parameters [13]. It takes only minutes in the consistent analytical model.

In this study, the model takes a step with developing a geometrical model of the single grit in kinematic approaches which investigates the interaction between the grains and workpiece. Abrasive grains on the wheel are assumed as in a certain geometrical shape which is mainly spherical, conic and pyramid in the literature. These shapes are chosen based on the literature [14] [15] [16] works with the main aspect of domination of high negative rake angle coming with high strain rate. Gilormini [17] assumed the conical single grit approach in his studies with consistent results in conventional grinding operations. In this study, the geometrical definition is done as a sphere edge conical shape, which is based on the measurement of grit with rake angle, oblique angle, height, and width and edge radius.

Contact length and chip thickness analysis are required after the geometric shape of grain was defined, since it defines the undeformed chip thickness which enhances the process forces with consideration of each active grain contact to the workpiece. In the literature, average contact length calculation has been formulated with Hahn's approach [8]. Contact length has been investigated via thermocouple measurements [18] [19] [20]. It was determined that contact length also related to applied force and the elastic modulus of the wheel after these measurements [21]. Contact length has been represented as a combination the deformation and geometric contact length [22]. Afterward, the kinematic path consideration has been investigated by many researchers to calculate mainly surface roughness parameter via contact length and maximum uncut chip thickness equations [23] [24]. The effect of the trochoid path was considered to be negligible in these studies, in this study uncut chip thickness and contact length has been modeled as instantaneous for surface roughness, force and temperature modeling and combined with [22] deflection model.

There have been some significant established grinding force models in the literature [25] [26]. In these studies, material removal rate parameter is related with the process forces with experimentally determined and formulated equations, and it is used by numerous researchers for the operation [27] [28]. In the later studies showed that the chip thickness modeling also has a significant influence on process forces [29]. After all, the normal and tangential forces with chip formation relation have been investigated and formulated as

mechanistic force model [30]. Then, this model was developed with sliding and cutting zone with mechanical approaches to predict chip formation in more detail with neglecting plowing forces since it is considerably less than chip formation forces [31]. Substitution of strain rate and undeformed chip thickness analyses has been made to develop mechanistic model with experimentally calibrated force coefficients [32]. The forces in surface grinding operations for each grain analyzed and combined with these models to predict forces more precisely [33] [34]. These models, which are constructed by the mechanical force model approach, require experimental data for each set of grinding parameters, tool, and workpiece combinations. Another modeling approach has been made by Oxley with slip line theory along with the primary deformation zone investigation by Johnson-Cook material model to predict forces on chip formation [35] [36]. Although FEM models can be modeled without calibration requirement, they can be very time-consuming. Nevertheless, they were suitable to investigate the insight of the operations and used by many researchers to understand the process and to develop analytical models based on the insight information [37] [38] [39]. Fully analytical approach was used by Ozlu to predict forces on turning operations with dual zone contact model on thermomechanical base [40]. Consideration of this study was that; material at the exit of primary shear zone creates two zones on the rake face of the tool as sticking and sliding regions depend on materials and cutting parameters. The basic of the cutting operation is dislocation of the material lattice structure for forming a plastic deformation until it breaks away. The plastic deformation occurs in the primary shear zone which is creating the chip formation along with secondary shear zone which is mainly friction effect with a combination of sliding and sticking area. The last cutting phenomenon is the plowing force which occurs on both elastic and plastic indentation of workpiece [41]. In grinding, the single grit interaction is considered as cutting tips and the interaction between the active grits and workpiece investigated in the manner of process forces. In this study, a thermomechanical approach was adapted into surface grinding operation to minimize these calibrations and experimental data.

The determination of the cutting zone temperature is crucial for the thermomechanical model and even more for the grinding operations. Thermally induced stress to the workpiece is also an important parameter in cutting interaction. The temperature increase changes the stress-strain behavior of the material and causes to less stress requirement for plastic

deformation of workpiece [42] [43]. Correct prediction of cutting zone temperature is crucial in grinding operations for accurate force predictions where high workpiece temperature rise arises. In this manner temperature distribution on the workpiece was modeled and temperature increase on grinding zone iteratively solved with a combination of thermomechanical force model and temperature distribution model.

The temperature in grinding operations is one of the main problems, which is caused by the accumulation of heat and friction effect on the workpiece. Residual stresses, micro cracks, deterioration of material structure and even surface burn occurs on the workpiece due to thermal effects. The modeling of the temperature process parameter is crucial to eliminate these process outputs. The generated heat cannot be removed by the chip contrary to conventional metal cutting. Grinding temperatures can be reaching 1200 degrees Celsius during the operation which is ten times larger than conventional cutting operations [44]. Heat generation over the grinding zone depends upon the friction angle, forces and grinding zone area [45]. Heat partition ratio is still a challenging problem in thermal modeling, and it is also crucial for temperature distribution predictions especially in liquid cooling grinding operations [46] [47] [48]. Heat flow into the workpiece is firmly depended on the heat partitioning which is affected by materials of workpiece and wheels, and cutting parameters. In this manner, the thermal conductivity of the CBN and conventional abrasives was studied by many researchers [49] [50] to predict heat partitioning values. It is stated that heat energy into the workpiece with CBN grinding is much smaller compared to aluminum oxide wheels [48]. The grain-scale interaction was studied and formulated as heat partitioning equations on the grain geometry, materials properties and cutting parameters [22]. In this study energy partitioning equation of Rowe [51] was used to distribute calculated heat energy into the workpiece. The heat flow as an input of thermal modeling was usually taken from the measurements or material removal rate based experimental energy equations. In the proposed model, it is related with the calculated thermomechanical forces and friction coefficient, measured grain geometry, and geometrical grinding zone calculation.

A numerous researcher studied temperature distribution on the workpiece, and most of the analytical approaches were based on the moving heat source theory developed by Jaeger [52]. Mathematical complexity of the problem resulted in a simplification of the problem into a moving heat point, line or plane source. Several contributions have been made on the

solution of steady state and quasi-state based on Jaeger's point heat source theory [53]. More detailed investigation of thermal aspect can be seen on Malkin's study [54], and on moving heat source problems in manufacturing examination of Kuo [55]. Analytical solution of moving heat source problems have been attempted by many researchers [56] [10] [57]. However, many aspects of the process remain because of the complicated nature of grinding operations. In this study, heat flux modeling was created based on the Malkin's reverse engineered heat flux estimation [58] via established heat flux distribution model. In this study moving heat source modeled as a parabolic equation with the heat flux consideration and the analytical solution was solved by a combination of numerical and Bessel function approaches within 3D coordinate system depend on time. Finally, the obtained maximum temperature rise on the workpiece is used as input in the thermomechanical model, and the both temperature and force calculation is solved iteratively to predict process parameters precisely. Then these obtained data was experimentally verified via force and temperature measurements. The most common method dynamometer measurement is used for the force measurement. However, various methods have been utilized in the literature for temperature measurements as a thermocouple, infrared radiation measurement techniques and vapor deposited film method [59] [60] [61]. For temperature measurement, a thermal camera was used, but the expected efficiency cannot be reached. Thermocouple measurement method was used as main temperature measurement in this study. In the early thermocouple measurement method; welding was used to attach thermocouple on the workpiece, but the error could as large as 40% with increasing tip of the thermocouple with welding [62]. Thermocouple fixation method for grinding temperature measurement was developed with epoxy usage on blind hole beneath the surface [63]. The same approach of thermocouple fixation was used in this study with different z-position to investigate temperature distribution on the workpiece.

1.2 Objective

Abrasive manufacturing processes implementations are increasing especially for the materials which are hard to machine, and requiring high surface quality. Especially machining of hard alloys results in excessive heat, and majority of it remains on workpiece in grinding operations. For this reason, thermal modeling is important for identification of residual stresses, micro cracks, surface roughness and surface burn on workpiece. Due to the complex and unpredictable geometry of the abrasives, process mechanics are considerably different compared to other machining operations. Thus, obtainment of desired part quality and performance by using try and error methods are quite time-consuming, and costly even in some cases may be impossible in grinding operations. The process models, which are based on analytic and experimental techniques, are proposed for analyzing the process parameters and obtaining the optimum cutting conditions. They compose the aim and the objective of the thesis. Within the scope of the thesis, abrasive geometry, grinding forces and temperature are investigated in detail, and mathematical models are developed. The developed, and experimentally verified process models can be used for obtaining the desired quality for shortest time and lowest cost in the applications on industrial parts.

The main purpose of this thesis is the development of model-based methods to improve the performance of abrasive manufacturing methods. In this objective, temperature, force and geometrical model approaches are investigated and modeled for surface grinding operation. Established models can be used in a broad spectrum since the main purpose of modeling case is the minimization of calibration and experimental dependence of the predictions. On the contrary, process conditions can be selected without the non-systematic and time consuming experimental investigation of the conditions. One of the principal purpose of engineering is to predict the problem before it happens, and it can be done better with the help of modeling of the process. Process modeling with using the finite element analysis methods can take a long time to obtain results even if calibration and experimental data are unnecessary for them. For this reason, modeling parts have been carried out with analytical approaches in this study.

The each model has its purpose in the complete model. For example, the geometrical model developed for predict surface roughness resulting from the grinding operations in an acceptable precision for a different combination of abrasives and workpiece, but also it is used for predict grinding contact zone length and uncut chip thickness on the operation for thermomechanical force model and temperature model. Force modeling has its local purpose as a prediction of applied loads during operation. The grinding parameters can be selected by predictions with force model within considering limitations of machine and tool. Besides that thermomechanical force model supply total heat generation on grinding zone for thermal calculations with the assumption of total energy turns into heat form. It is known that the workpiece surface exposed to high temperatures during the grinding. Excessive temperatures can cause surface burns, dimensional deformations, residual stresses and undesirable changes in material microstructure. Process temperature distribution model is developed to enable selection of parameters to prevent these problems during operation. Moreover, heat partitioning and temperature distribution model supplied a temperature data for thermomechanical model and resulted in the better prediction of process parameters with iterative working principle.

The motivation of this study is to understand the relationship between geometry, force, and temperature and fulfill the lack of analytical approaches as a whole solution of the process in the literature. Furthermore, one of the prospective aims of this study is to create scientific methods for the usage of models in industrial scale.

1.3 Layout of the Thesis

The thesis is organized as follows;

In Chapter 2, the geometrical approach is presented to calculate contact length of grinding zone and undeformed chip thickness and surface roughness with considering the trochoid path of the chip. Assumption and formulations which are based on the measurement and analysis of the grains on the wheel are given.

In Chapter 3, thermomechanical force model is presented with the adaptation into surface grinding operations in the form of oblique and dual zone approaches. The detailed formulation and simulation methodology is proposed for grinding operation.

In Chapter 4, thermal investigation for the grinding operations are presented. Heat flow equation depending on the thermomechanical model is proposed. Heat partitioning model is used to distribute the calculated heat flow into the workpiece. 3D time-dependent moving heat source temperature distribution model with heat flux modeling is presented to predict workpiece temperature distribution.

In Chapter 5, complete solution procedure of thermomechanical model with temperature predictions is proposed. Shear angle and friction angle values are investigated through the negative rake angle. The thermomechanical force with temperature effects and temperature distribution on the workpiece is presented and verified by the several experiments.

In Chapter 6 & 7, the suggestions for the further research and conclusions are presented.

2 GEOMETRIC APPROACH AND MODELS FOR SURFACE GRINDING

In this section, geometrical properties of the surface grinding operations were investigated and modeled with corresponding approaches. Unlike normal cutting tools, the geometrical structure of grinding cutting particles are random in a range mainly depend on abrasive particle type and bonding material. For these reasons, analysis of the geometry is crucial for process modeling.

In contrast extensive literature, this study presents a variation of grits in the calculation instead of taking the single chip formation based on the grinding parameters. Simulated wheel topography has more accurate results with the creation of different shape properties of the grits on the wheel.

The number of the cutting points above the certain height, which are specified as active grains, are detected with optical image device. Active grains on wheel refers to cutting edges or number of flute on milling tool in the analogy. Geometrical properties of the single grit are way difficult to observe and done by the same device with bigger lenses. It gives specific properties like height, width, rake angle, oblique angle and edge radius of the grit in a range of standard deviation to more accurate predictions of the models.

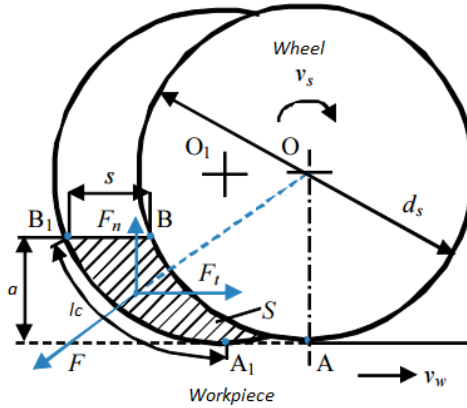


Figure 1: Basic geometry of the chip formation on grinding

The kinematic relationship between the grinding wheel and workpiece considered on single abrasive grit cutting range. Peklenik [64] suggest the first analytical investigation of kinematic in grinding with a simple milling material removal analogy and many researchers follow his footsteps. Figure 1 shows the basic kinematic of chip formation on grinding operations with exaggerated illustration. In this figure up grinding operation held with v_w workpiece velocity and v_s wheel speed, cutting with the depth of cut a creates s maximum uncut chip thickness in l_c contact length. In general, these basic kinematic models adhere to macro scale with the parameter of feed rate, spindle speed, depth of cut and wheel diameter which leads to avoiding micro parameters such as density of active grains or grain properties. In order to overcome this simplification modified 2D z-map technique is used to predict workpiece surface roughness and kinematic path of grain [65].

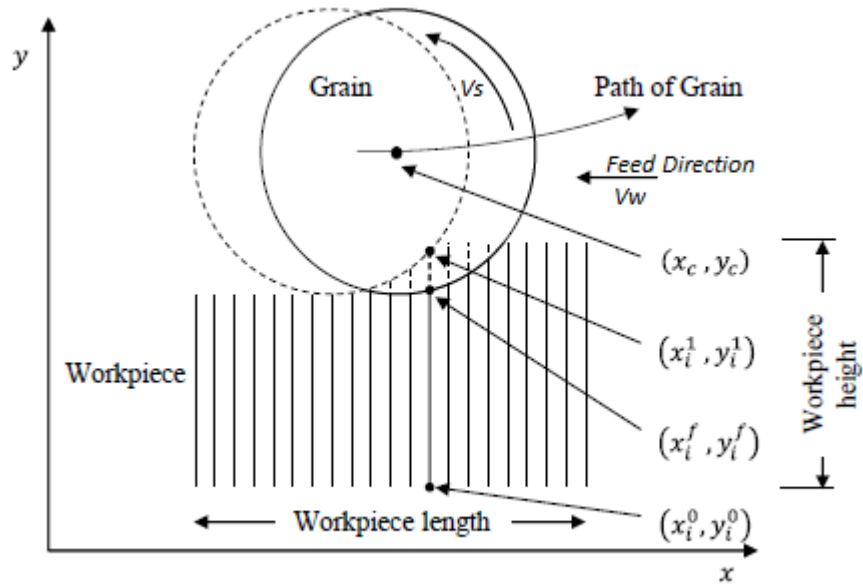


Figure 2: 2D Z-Map for grinding with trochoidal kinematic [65]

The grain trajectory is a combination of the circular movement from spindle speed and linear translation from feed velocity. This trochoidal path definition is crucial for determining contact length and uncut chip formation which ends up with a surface roughness of workpiece. In this simulation, grains are assumed as 2D spherical geometrical shapes. Darafon [66] mentioned 2D and 3D kinematic modeling on FEM with the result in the less than 1% difference between them. The workpiece is defined with infinitesimal line segments corresponding to feed velocity and wheel speed as in above Figure 2. The spacing between the lines is defined by optimization of accuracy and calculation time with the study of line segment density definition by Warkentin [67].

In this simulation trochoidal path is created over the line segments, and each grain center positions are calculated as expressed in below equations. In this coordinate system, y is referred to a depth of cut and x is referred to feed direction. Grain geometry is constructed stochastically as in Deniz model [68], and each grain kinematic trochoid path is calculated as expressed in below equations with corresponding coordinates.

$$\theta = \cos^{-1} \left(1 - \frac{a}{D/2 + h_{grit}} \right) \text{ up grinding angles} \quad (1)$$

$$t_{\theta} = \left(\frac{60}{n}\right) \frac{\theta}{2\pi} \quad \text{time for } \theta \text{ angle} \quad (2)$$

$$x_{i_0} = (i - 1)dt_{\theta}v_{ws} - v_w/(Cn), \quad x_{i_1} = i(r \sin(\theta) d\theta + dt_{\theta}v_{ws}) \quad (3)$$

$$y_{i_0} = r(1 - \cos(\sin^{-1}(x_{i_1} - x_{i_0})/r)), \quad y_{i_1} = r(1 - \cos(id\theta)) \quad (4)$$

$$h_{instantenous} = \begin{cases} (a - y_{i_1})/\cos(id\theta) & \text{if } y_{i_0} > a \\ (y_{i_0} - y_{i_1})/\cos(id\theta) & \text{if } y_{i_0} < a \end{cases} \quad (5)$$

In kinematic calculation, grinding tool cutting start and exit angle θ are derived from up milling analogy as expressed. Immersion angle time divided into equal parts which is defined by time for complete the angle t_{θ} . $id\theta$ is instantaneous cutting angle that define the where is the edge of the grain. Model can track the x and y coordination while center of wheel O is moving across to O' as illustrated in Figure 3. Kinematic position of the grains are calculated by this method and instantaneous uncut chip thickness, material removal rate and kinematic contact length could be extracted from this simulation.

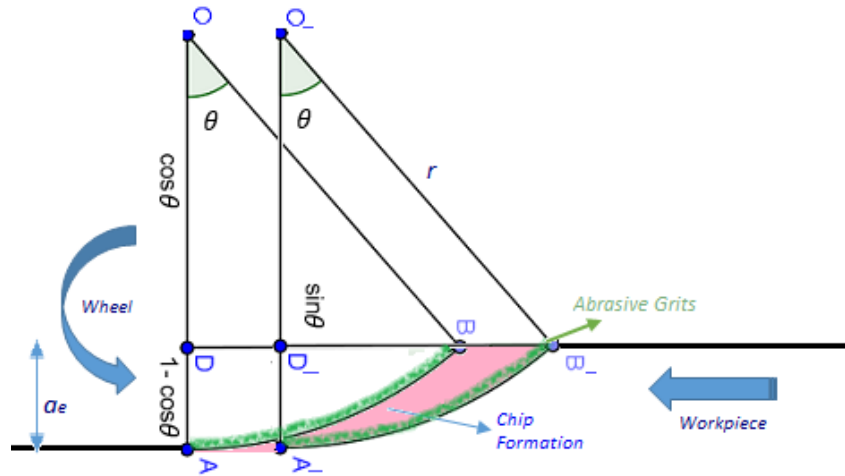


Figure 3: Kinematic path of grinding

Single grit trajectory could be foreseen as above method, but we need to complete this cycle with all the active abrasive grains. Contact length calculation is necessary for this step, and it is crucial for calculation of force and temperature in the next chapters. The contact length

is proportional to rubbing area between workpiece and grains. It is also effective on wearing mechanism since longer contact length triggers grain fracture. There is three type of calculation for contact length; geometric, kinematic and deflected contact length which sum up as total contact length. Geometric and kinematic contact length already defined above methods.

Super abrasive machining grinding wheels are usually vitrified wheels and resin bond wheels with the usage of CBN. Rowe [22] stated that deflections play a significant role in the determination of total contact length, since deflection length is more efficient on geometric contact length, especially for super abrasive machining. The deflection model needs to normal process force per unit width during grinding to compute deflection quantity. Negative feedback system from the force model can lead to better estimation of this deflection mechanism. Deflections are depended on combined elastic modulus (E) of workpiece and wheel with a roughness factor (R_r) range in 5 to 15. Equation (6) defines the deflection contact length.

$$l_d = \sqrt{\frac{16 \times R_r \times F_n \times (r + h_{grit})}{\pi \times E}} \quad \text{deflection contact length} \quad (6)$$

Total contact length is also needed in the kinematic model to calculate active grain in a particular area with the multiplication of contact length and width of the wheel. Moreover, it is also a great deal when process forces are calculating. Equation (7) defines the total contact length with a combination of kinematic and deflection one.

$$l_t = \sqrt{l_d^2 + l_k^2} \quad \text{total contact length} \quad (7)$$

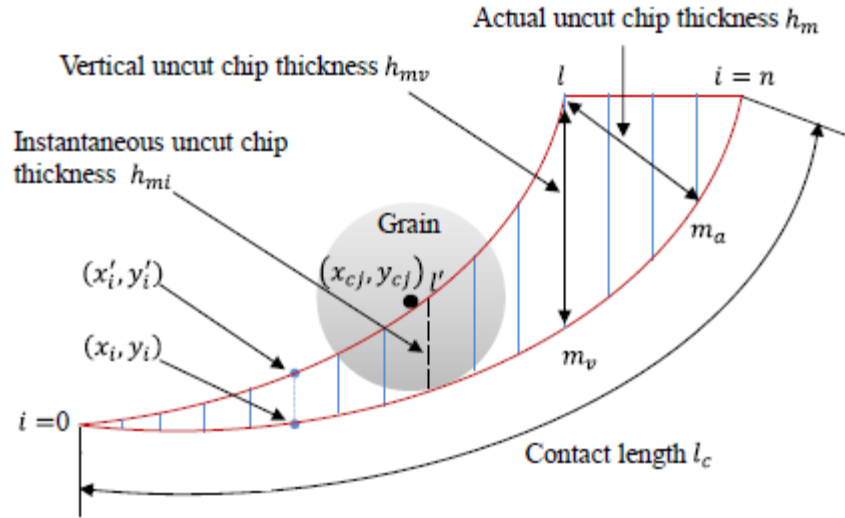


Figure 4: Chip contact length and chip thickness on Z-map technique [69]

Chip volume per grit is also calculated with corresponding 2D coordinate multiplication with a width of the grit. Uncut chip thickness is obtained in the same analysis with finding the maximum gap between consecutive trochoid lines. Multiplication of chip thickness in the y-direction with x-direction length depend on workpiece velocity defines the 2D projected area of the chip. Grain width multiply with the projected chip area is used to obtain chip volume per grain movement. Vertical uncut chip thickness obtained from the kinematic coordination of y, and it is tilted with a corresponding θ angle to get actual uncut chip thickness. Grain movement is assumed as stationary on an x plane at first and creates the first trajectory, then x coordinate frame to next step to create the second trajectory for active grains on contact length. The simulation results for the chip formation as illustrated in Figure 5.

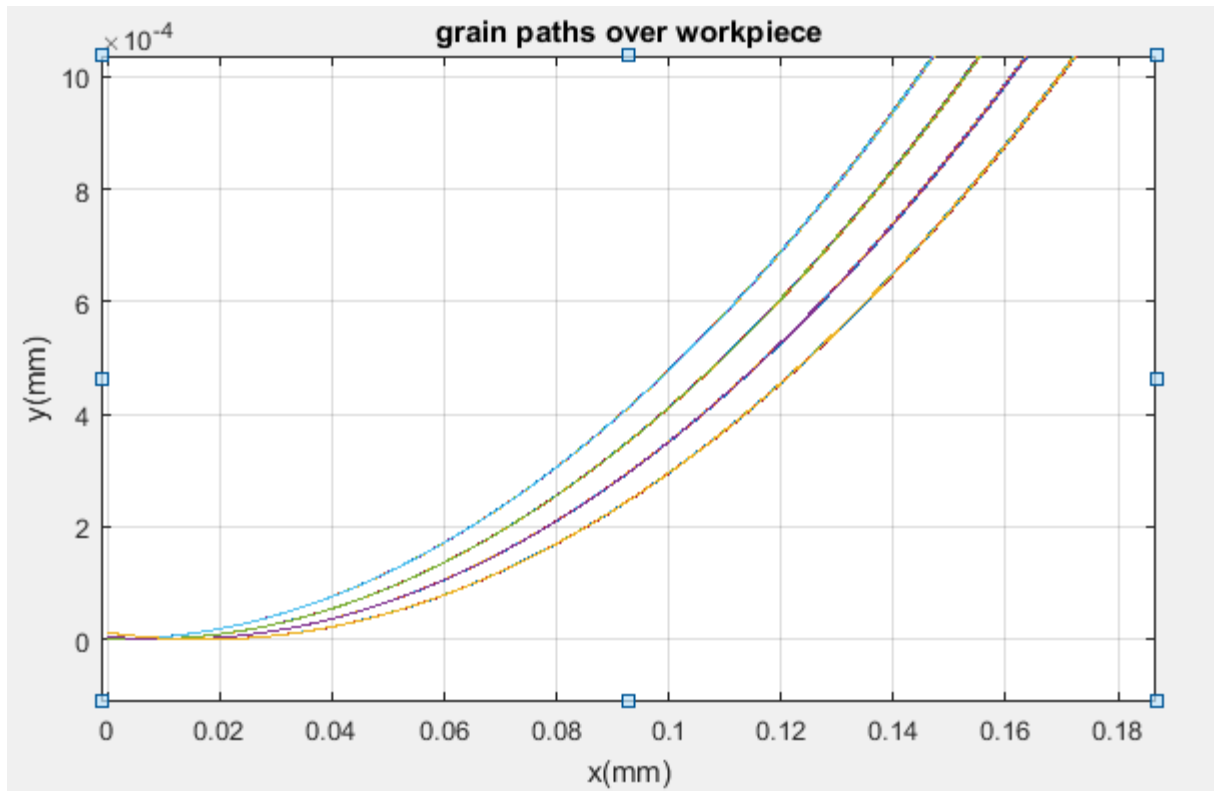


Figure 5: Simulated grain paths over workpiece

Each line segments in Figure 5 represents cutting lines of the active grits, and each x movement creates another set of lines, which are correlated in the z direction to get surface roughness on one set. Surface roughness profile prediction is impossible due to randomness nature of the grinding process. However, upper and lower bound created for it to define a range for the process. The experimental and simulated data are set up with the parameters as $V_s=30$ mm/s, $V_w=120$ mm/s with the depth of cut 100 micrometers 20 mm diameter CBN wheel are used as seen in Figure 6. Comparison with literature is made with Inasaki [70] model and experiment to correct it. Results are correlated with simulation which is held by FEM with sphere grains.

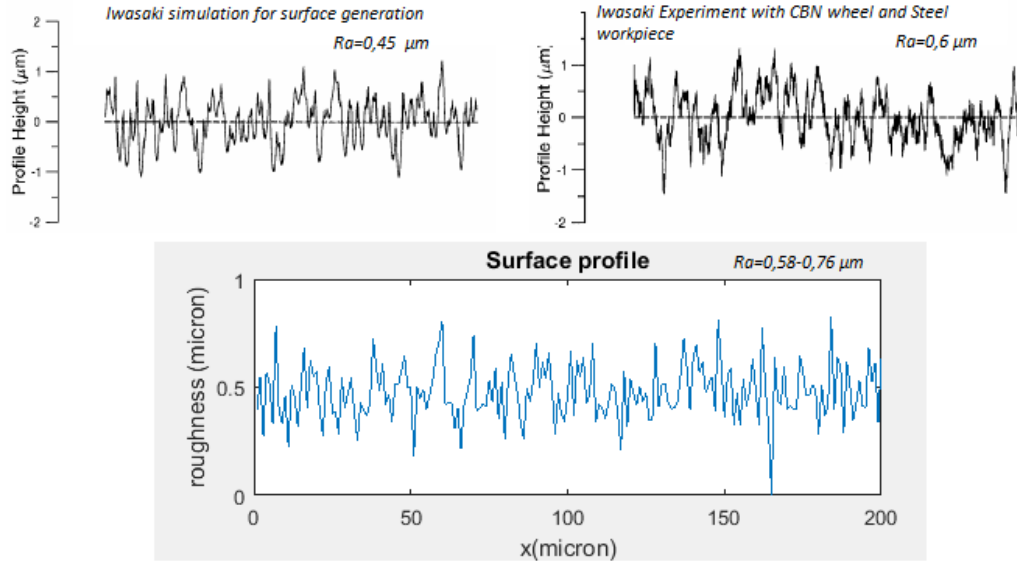


Figure 6: Simulation results for surface roughness and literature comparison

Surface roughness predictions are quite consistent although the stochastic nature of grits location and geometry disallow to generate an exact surface profile. In this content, generation of different surface roughness values give a range for prediction of reality. Simulation comparisons are provided on Figure 7 with substitute parameters.

Parameter	Symbol	Data	Unit
Depth of cut	a	0.01-0.1	mm
Wheel Diameter	ds	200	mm
Wheel Speed	vs	30	m/s
Feed Speed	vw	0.3	m/s
Grain Spacing	Lg	0.372	mm
Grain Width	dg	0.143	mm
Grain Height	hg	0.118	mm

Table 1 Grinding simulation parameters

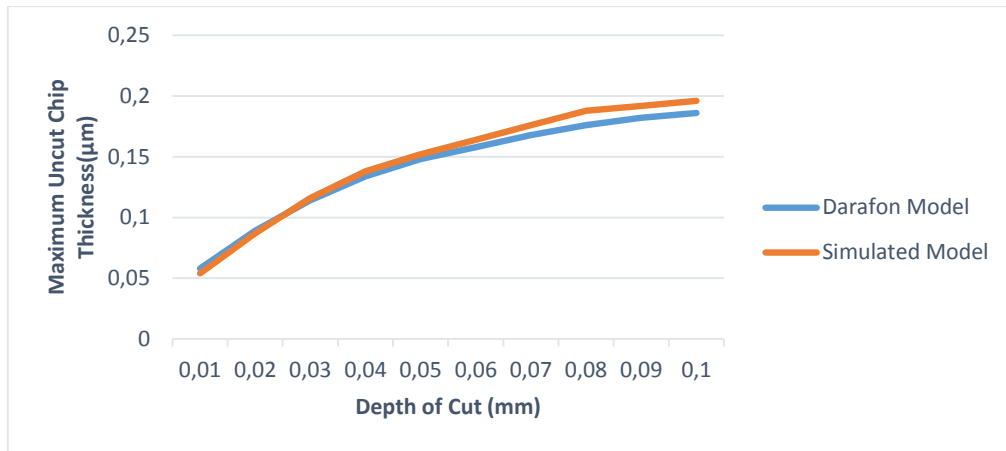


Figure 7: Simulation of uncut chip thickness vs. depth of cut

In the thermomechanical force model, instantaneous chip thickness calculation is very crucial for model results. In this study, an uncut chip thickness calculation was performed on the trochoid path with above formulations. The modeled uncut chip thickness and conventional approach of feed rate multiply with sinus immersion angle were compared.

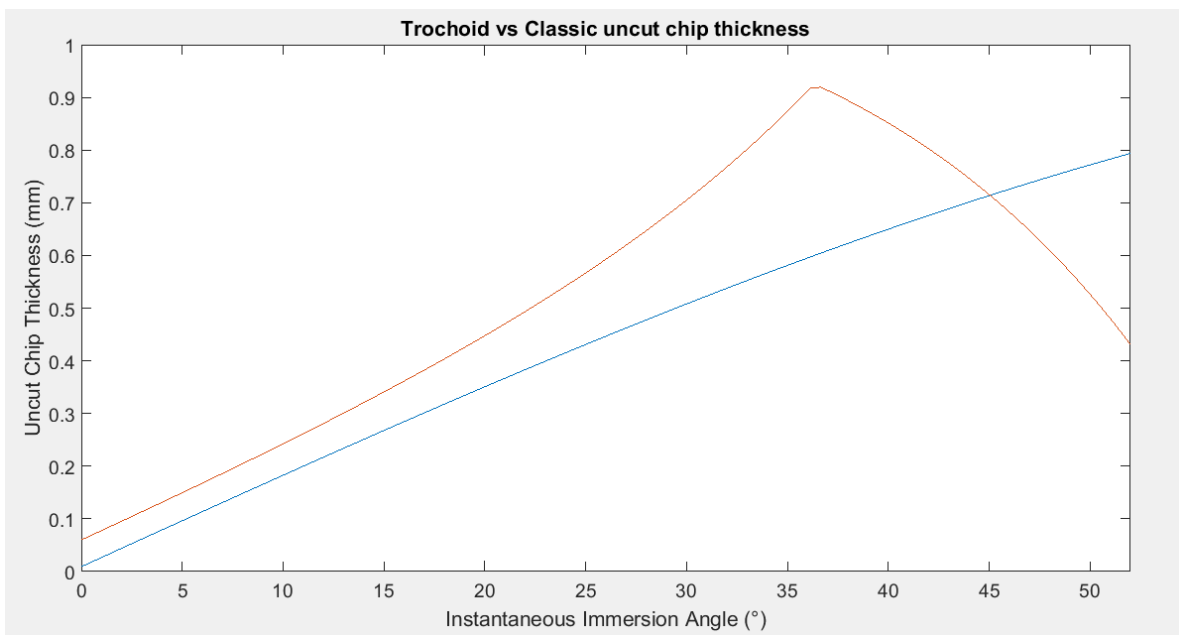


Figure 8: Instantaneous uncut chip thickness comparison for low r/ae ratio

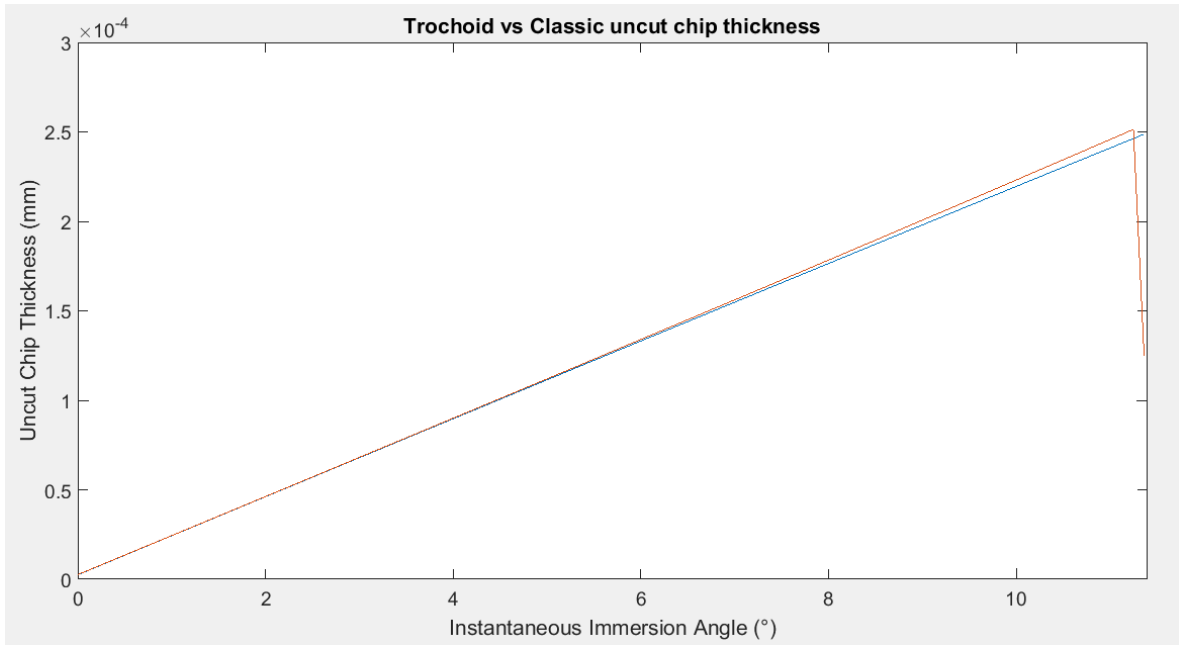


Figure 9: Instantaneous uncut chip thickness comparison for high r/ae ratio

The difference between the classical model and the presented model is very low since a low cutting depth is held in the grinding operations. For this reason, it can be employed in both form of calculation, but it should be noted that trochoid path effect will be higher in micro grinding operations regarding instantaneous uncut chip thickness.

The ground surface morphology is calculated by considering the overlapping scratches and peaks-valleys pattern which is generated by the random nature of grinding process compare to ideal cutting operations. The topography of workpiece surface is dependent mainly on process parameters as illustrated in below figures. The surface roughness simulation and geometric approach idealize the grinding process with considering the stochastic approach of abrasive grit locations and shapes. Moreover, interruption of cutting process by wear mechanism and process heat can be effective on these values. The fracture of abrasive grit can lead to some unanticipated peaks or craters. High process temperature can also alter the workpiece material properties which lead to increasing contact length and surface roughness related to residual stress by temperature.

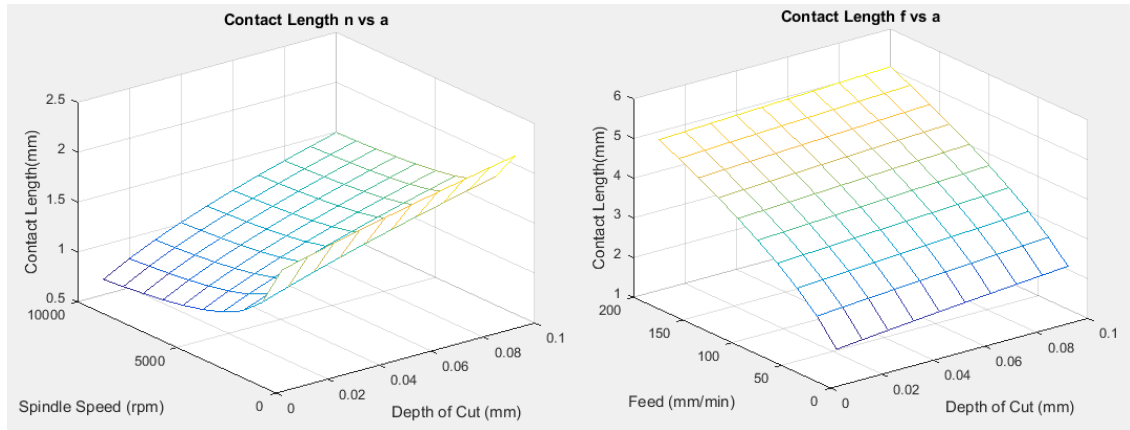


Figure 10: Contact length analysis

According to kinematic approach contact length analysis done by different spindle speed and feed rate in Figure 10. An analysis of the contact length data for surface grinding operations of the AISI 1050 steel with 20 mm diameter CBN wheel implies a dependence of contact length in the order of feed, depth of cut and spindle speed.

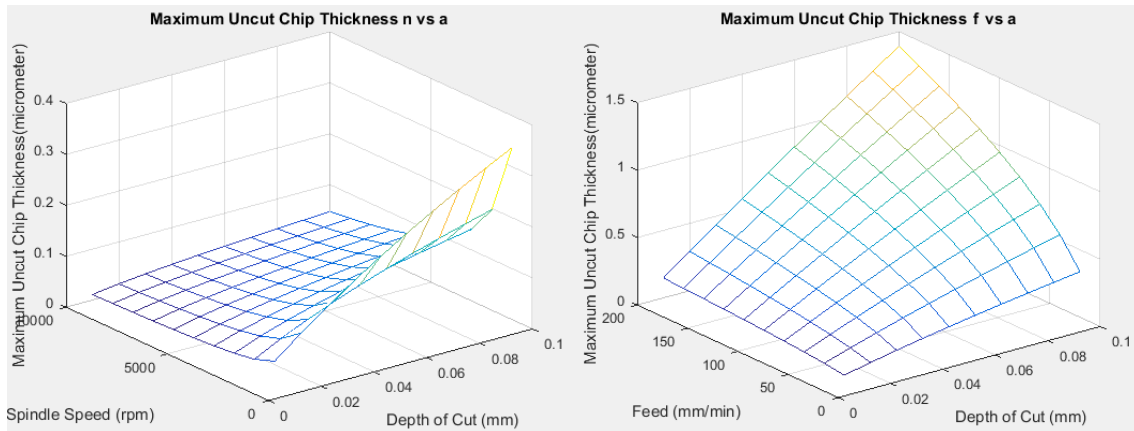


Figure 11: Maximum uncut chip thickness analysis

Analogously to other machining operations, maximum uncut chip thickness analysis is theoretically the first step to calculate process forces and temperature. Maximum uncut chip thickness analysis is done by kinematic analysis as explained in this chapter with uniform wheel topography to maintain consistency. The ideal maximum uncut chip thickness values can be obtained with grinding parameters in Figure 11. The fact remains that calculation of uncut chip thickness is varying in a range of random distribution of grit height mainly. The idealized maximum uncut chip thickness is created on each abrasive grits while their

properties are changing according to a random distribution. The corresponding non-uniform surface profile is generated by calculation of each active cutting grit on the equivalent cutting area, which is calculated by contact length times grain width. Considering this situation, the non-uniform cutting paths and surface roughness obtained with grinding parameters as seen in Figure 12.

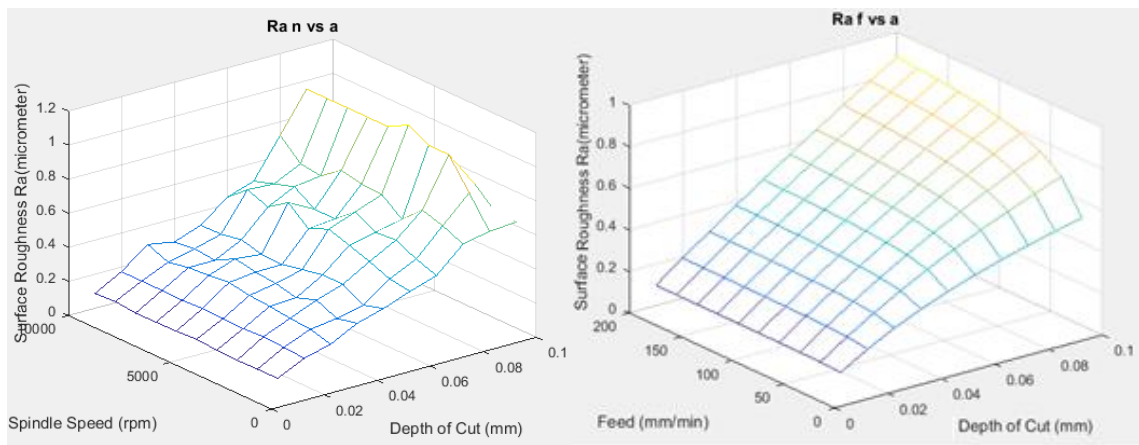


Figure 12: Surface roughness analysis

Simulation of surface roughness model illustrates that depth of cut is the main parameter on the grounded workpiece topography. It is theoretically harder to create an absolute solution for surface roughness due to nature of grinding mechanism. In this study different aspects of the kinematics and mechanical approaches are used to create this simulation. The results are quite consistent with literature as compared. Furthermore, the dependency of surface roughness should be considered with abrasive grit types and shapes. By this purpose, simulation was run with different abrasive grit properties with corresponding material removal rate as seen in Figure 13.

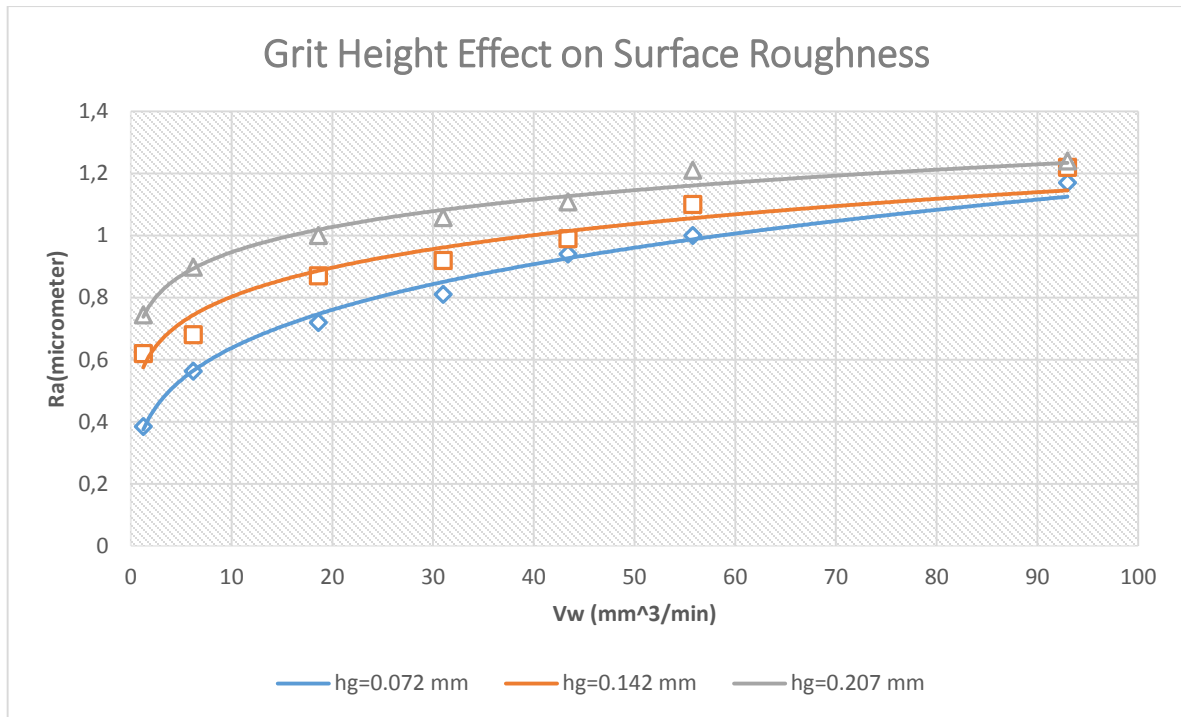


Figure 13: Grit properties vs. surface roughness

The above results are obtained with the 100-micrometer depth of cut, 5000 rpm spindle speed and 20 mm CBN wheel diameter on AISI 1050 steel. Larger values of grit height apply rougher surface texture on the workpiece with creating bigger craters. However, sensitivity to grit size is decreasing when feed speed and corresponding material removal rate are increasing. CBN wheels are much predictable on surface roughness case with the more definable structure of grits on the wheel. The geometric approach results show that finer grit size leads to smoother surface finish up to a point. Grinding parameters and wheel properties related with grit geometry can be selected to obtain approximate intended surface roughness results.

In summary, the effects of grinding parameters on geometry are examined and modeled in this section. Uncut chip thickness and grinding length models, which are important in process modeling, have been applied with a new approach of the trochoid path as a contribution of this study. In addition grain geometry parameters are investigated as detailed in the above section. Moreover, active cutting grain percentage is modeled with a new stochastic approach depend on grinding parameters and grain geometry properties which can be found in Appendix A.

3 THERMO-MECHANICAL FORCE MODEL FOR SURFACE GRINDING

This chapter begins with the description of semi-analytical force model in the analogy of micro milling operations. Force analyses are implied on each active single grain which is already modeled in geometric approach chapter. Force prediction on machining has been used in a range of variety along with empirical, semi-analytical and analytical approaches. Earlier, Shaw [14] has stated that tangential force can be calculated by power consumption and torque which are proportional to material removal rate. Calculation of material removal rate is a nuisance since the exact geometrical shape and interaction of cutting teeth is unpredictable compared to milling operations. Therefore the obtained grit measurements are fitted to Gaussian distribution to perform consistent results. Chip formation investigation for abrasive grain implemented on other grits in this distribution, and more trustworthy force model can be developed.

The thermomechanical approach is used to calculate shear stress at grit workpiece interaction. Primary shear zone calculation is necessary to predict a force on grit shearing area. In this study, micro milling analogy is adapted to grinding operations in grit scale interaction, and it is applied on each grit on contact zone according to the normal distribution of grits as explained in geometrical approach section. Johnson Cook material model and thermomechanical approach on this study require less calibration and experiments to calculate process forces on grinding operations.

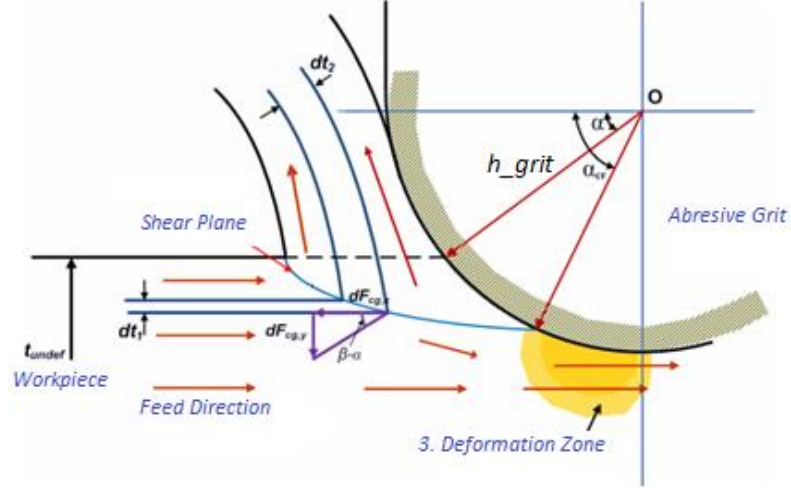


Figure 14: Single grit interaction & cutting schematic [71]

As described in the geometric approaches section, the spherical edge of grain approaches can be used for modeling of grain. As seen in Figure 14 shear plane definition is starting with the definition of cutting zone on stagnation point up to exit angle. Stagnation point from critical rake angle (α_{cr}) is defined by incipience of third deformation zone and defined by the following equation (8) with respect to grit radius ($h_{grit}/2$) and minimum uncut chip thickness (t_m).

$$\alpha_{cr} = \sin^{-1} \left(\frac{h_{grit}/2 - t_m}{h_{grit}/2} \right) \quad (8)$$

Critical rake angle is considered by previous works; different theories and calculation methods are applied in this manner. The result in earlier studies [72] [73]; the minimum uncut chip thickness is mainly depended on edge radius of the cutting tool. The literature based stagnation angle is used in this study which is around 37 degree, and the corresponding minimum uncut chip thickness is 0.2 times cutting edge radius value. Below that region, plowing forces take place in third deformation zone which can be calculated in thermomechanical approach with edge force analysis.

3.1 Mechanistic and semi analytical force model

The cutting regime, which is between start angle and stagnation point, includes two phenomena as; first deformation zone on a shear plane and second deformation zone on rake face of grit. Semi-analytical approaches stated that forces in these zones are depended on specific grinding force coefficients, and are distributed by a geometrical occurrence which can be modeled from orthogonal to oblique cutting. The force equation in each direction per abrasive grains can be written mechanistically as in equation (9).

$$F_{t_{grain}} = K_{tc} \times Area_{grain} + ploughing_{force_t} \quad (9)$$

$$F_{n_{grain}} = K_{nc} \times Area_{grain} + ploughing_{force_n}$$

$$F_{r_{grain}} = K_{rc} \times Area_{grain} + ploughing_{force_r}$$

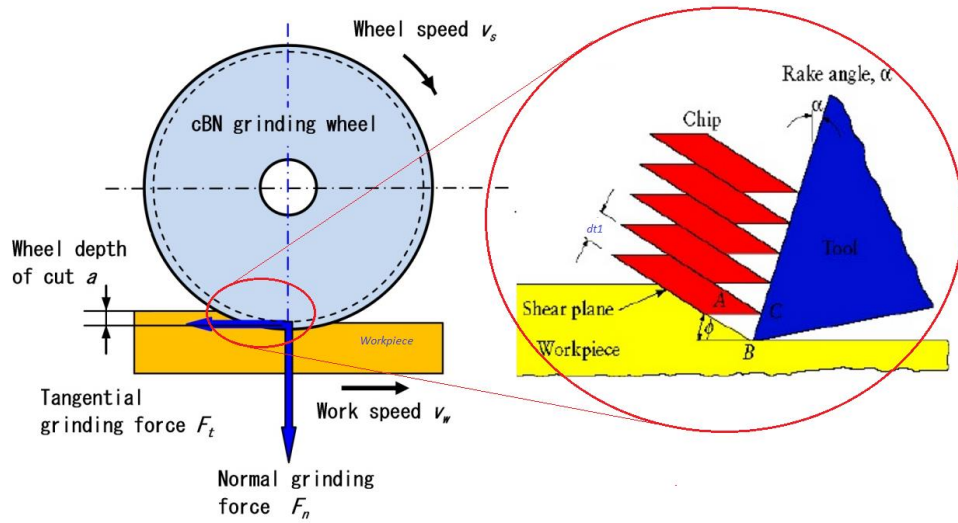


Figure 15: Schematic illustration of the process forces and chip formation in cutting [74]

Formation of chip process is considered as in two dimension space with corresponding tangential and normal grinding forces as shown in Figure 15. Single grit workpiece interaction is divided into infinitesimal parts by dt with corresponding instantaneous normal rake angle is α_i , instantaneous friction angle is β_i and instantaneous shear angle is ϕ_i . Because of the fact that abrasive grits random locations and shapes the general rake angle in grinding operations is around negative 30 degree.

$$dF_n = -\frac{\tau \times \cos(\beta_i - \alpha_i)}{\sin \phi_i \times \cos(\phi_i + \beta_i - \alpha_i)} dt \quad (10)$$

$$dF_t = -\frac{\tau \times \sin(\beta_i - \alpha_i)}{\sin \phi_i \times \cos(\phi_i + \beta_i - \alpha_i)} dt \quad (11)$$

In machining force simulations, shear angle ϕ regulate primary shear zone deformation. Predicting shear angle with the calculating ratio between uncut and cut chip thickness is relatively harder than other machining operations since the cut chip thickness are varying randomly from 1 to 50 micrometer due to nature of grinding process. Nevertheless, the assumption of Merchant's minimum energy principle can lead to not the best but modest equation (12).

$$\phi = \frac{(\pi + \alpha - \beta)}{2} = \tan^{-1} \left(\frac{r_m \times \cos \alpha}{1 - r_m \times \sin \alpha} \right) \quad (12)$$

Oxley's model [75] of the oblique cutting theory is used to calculate normal, tangential and radial direction disintegrations in the manner of geometrical approaches. Tilted edge of cutting plane entail the chip flow angle which is different from the cutting velocity direction compare to orthogonal one.

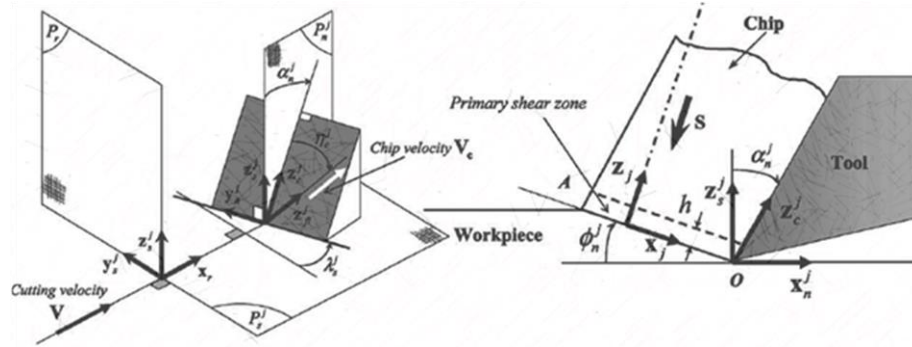


Figure 16: Schematic illustration of oblique cutting [41]

Figure 16 illustrates the oblique angle effect on the geometry of tool-workpiece interaction. Oblique angle or shear flow angle λ_s is forming the chip flow angle η_c . Normal friction angle

β_i can be calculated with multiplication of tangent shear flow angle and cosine chip flow angle. Cutting coefficients obtained as follows equations according to Budak's lecture notes.

$$dF_n = - \frac{\tau \times \cos(\beta_i - \alpha_i) + \tan \lambda_s \times \tan \eta_c \times \sin \beta_i}{\sin \phi_i \times \sqrt{\cos^2(\phi_i + \beta_i - \alpha_i) + \tan^2 \eta_c \times \sin^2 \beta_i}} dt \quad (13)$$

$$dF_t = - \frac{\tau \times \sin(\beta_i - \alpha_i)}{\sin \phi_i \times \cos \lambda_s \sqrt{\cos^2(\phi_i + \beta_i - \alpha_i) + \tan^2 \eta_c \times \sin^2 \beta_i}} dt \quad (14)$$

$$dF_r = \frac{\tau \times \cos(\beta_i - \alpha_i) \times \tan \lambda_s - \tan \eta_c \times \sin \beta_i}{\sin \phi_i \times \sqrt{\cos^2(\phi_i + \beta_i - \alpha_i) + \tan^2 \eta_c \times \sin^2 \beta_i}} dt \quad (15)$$

Oblique theory leads to different parameters as shear flow angle, and chip flow angle which are studied by researchers earlier [76] [77] [78] The chip flow angle is calculated by the following equations (16) [40];

$$0 = (A^2 + B^2) \times (\sin \eta_c)^4 - 2AC \times (\sin \eta_c)^3 + 2(AC + CD) \times \sin \eta_c \quad (16)$$

$$+ (C^2 + B^2 - 2A^2 - 2AD)(\sin \eta_c)^2 + (A^2 + D^2 + 2AD)$$

$$A = -\tan \lambda_s (\tan \phi_i \sin \alpha + \cos \alpha)$$

$$B = \tan \phi_i$$

$$C = \tan \lambda_s$$

$$D = \tan \lambda_s \tan \beta (\tan \phi_i \cos \alpha - \sin \phi_i)$$

According to oblique theory calculations, three input is considered; normal rake angle α_i , inclination angle λ_s and rake face friction angle β_i to calculate chip flow angle η_c , normal shear angle ϕ_i . Hence, the calculated force coefficients are geometrically distributed on normal, tangential and radial planes. The incremental analysis on grit workpiece interaction with dt step size adapted to the chosen sphere grit shape which will define cross sectional area to calculate forces on each grit. The corresponding equivalent interaction area of spherical grit is calculated with basic spherical projected area formulas. Integration from stagnation point to exit angle with respect to instantaneous rake angle gives total forces on the grit workpiece interaction. Equations (18, 19) are the semi-analytical models of grain size

chip formation forces without shear stress calculation, it will be considered in thermomechanical aspect.

$$\alpha_{start} = \cos^{-1}\left(\frac{h_{grit} - t_m}{h_{grit}}\right) \cong 0.183 \times h_{grit}/2 \quad (17)$$

$$\alpha_{exit} = \sin^{-1}\left(\frac{h_{grit} - a}{h_{grit}}\right)$$

$$F_{n_{grain}} = \int_{\alpha_{start}}^{\alpha_{exit}} \frac{\tau \times \cos(\beta_i - \alpha_i) + \tan \lambda_s \times \tan \eta_c \times \sin \beta_i}{\sin \phi_i \sqrt{\cos^2(\phi_i + \beta_i - \alpha_i) + \tan^2 \eta_c \times \sin^2 \beta_i}} \times 2h_{grit}^2 \cos^2 \alpha_i d\alpha_i \quad (18)$$

$$F_{t_{grain}} = \int_{\alpha_{start}}^{\alpha_{exit}} \frac{\tau \times \sin(\beta_i - \alpha_i)}{\sin \phi_i \cos \lambda_s \sqrt{\cos^2(\phi_i + \beta_i - \alpha_i) + \tan^2 \eta_c \times \sin^2 \beta_i}} \times 2h_{grit}^2 \cos^2 \alpha_i d\alpha_i \quad (19)$$

3.2 Thermomechanical force model

Mechanistic and semi analytical approaches always requires calibration with tests for cutting coefficients. One of the most efficient methods for minimization of calibration is the thermomechanical model, which is based on materials properties and cutting parameters. In this study, the model was adapted to high-speed surface CBN grinding operations. Structurally, the working principle of the thermomechanical model is to calculate the shear forces in the shear zone from Johnson-Cook material model and geometrically distribute it on the chip formation with the effective surface friction coefficient on the rake face generated by this force. Temperature due to plastic deformation and chip tool contact, change the properties of the material, which can only be found by iterative solution of the thermomechanical model. The most important factor in cutting models is the calculation of shear angle. In this manner the effect of negative rake angle on shear force and shear angle was investigated for grinding operations. Shear angles were scanned from -50 to -10 degrees to obtain the minimum energy with corresponding forces in an iterative cycle and applied to the cutting particles of grinding wheel to get process forces mainly in tangential and normal directions.

In this section, as a first step; thermomechanical force model is considered oblique with the mean rake angle and oblique angle to calculate shear angle within minimum energy principle consideration along with the grit distribution. The second step is the calculation of the thermomechanical forces considering edge force analysis with the calculated shear angle on the grit scale within immersion angle of grinding operation, which effects the undeformed chip thickness. In the last step, process forces were obtained by applying the calculated forces on randomly distributed structure of the active cutting grits on the grinding wheel. The resultant forces are ready to use for workpiece temperature distribution calculation with the heat partitioning model.

3.2.1 Oblique Thermomechanical Force Model

Oblique theory on the thermomechanical model is used to calculate forces in grinding operations. Since, the geometry of the each grain that perform of cutting process are different and unpredictable, with their random oblique and rake angles, height and width. The force that each grain creates during grinding operation is different, and it is in the oblique plane. The model includes shear zone calculation, normal and friction force calculation on rake face and shear angle calculation with minimum energy approximation and process forces with combining them.

3.2.1.1 First Deformation Zone and Shear Force

Once material model parameters are known for the workpiece, it is feasible to use on different process parameters as spindle speed, feed et cetera. Molinari and Dudzinski [42] studied primary shear zone analysis with the assumption of constant chip thickness on shear zone without plastic deformation on the process. Once the primary shear zone stress is calculated according to this theory, dual zones approach takes over to calculate stress and friction coefficients on rake face to acquire more accurate results. The first zone model used can be found in detail [43]. There are assumptions utilized by the model; these are the constant thickness of the cutting zone and there is no plastic deformation in this region before and after cutting and uniform pressure distribution on the shear plane. Figure 17 is the schematic representation of cutting mechanism with negative rake angle which includes

parameters as V cutting speed, w width of grain, h_1 uncut chip thickness, ϕ shear angle and α the rake angle.

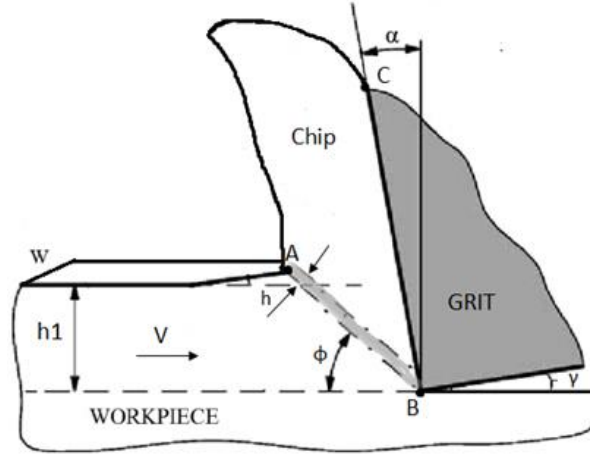


Figure 17: Illustration of cutting geometry

Johnson-Cook material model is used to calculate τ_0 using data based values. The parameters A, B, n, m and v are calibrated by workpiece material. When parameters are known, the shear stress can be calculated by solving the equation (20) with Runge-Kutta iteration method within boundary conditions which can be found in detail [79].

$$\tau_0 = \frac{1}{\sqrt{3}} \left[A + B \left(\frac{\gamma}{\sqrt{3}} \right)^n \right] \left[1 + \ln \left(\frac{\gamma}{\gamma_0} \right)^m \right] [1 - T^v] \quad (20)$$

Shear stress at the exit of the primary shear zone τ_1 can be calculated by momentum conservation on the shear plane.

$$\tau_1 = \rho(V \sin(\phi) \cos(i))^2 \gamma_1 + \tau_0 \quad (21)$$

If the shear stress distribution is assumed to be uniform over the AB plane, the shear force F_s can be obtained by;

$$F_s = \tau_1 \frac{wh_1}{\sin(\phi) \cos(i)} \quad (22)$$

According to the above calculation on the AB plane, analysis on rake face introduced two zone contact model approach.

3.2.1.2 Dual Zone Contact Model

According to Zorev [80] studies, the zone called dual contact zone [40] is divided into two regions as sticking and sliding during chip formation on the rake plane. From the point of initial contact of the chip on the rake face is exposed to the high pressure and called sticking when the sliding region remains lower. The phenomena that the value of the sliding friction coefficient governed by Coulomb Friction, which cannot exceed 1.0 on metallic contact has been examined and verified by a number of researchers [81] [82] [83]. Stress distributions on the rake plane are represented in Figure 18.

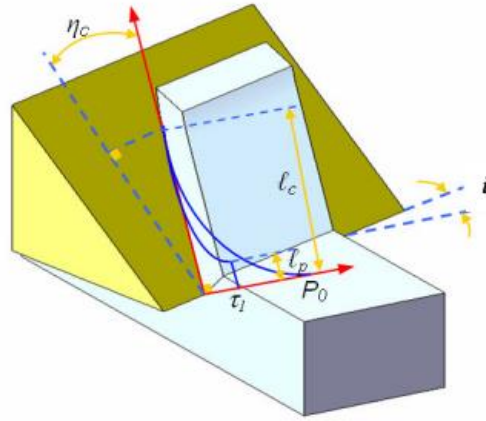


Figure 18: Illustration of oblique cutting geometry [40]

Oblique cutting theory changing geometry with the inclination angle. Based on this angle, chip flow angle and shear flow angle η_s occurs and apparent friction angle $\lambda_a = \tan^{-1}(\mu_a)$ is oriented as β . Below equation is rearranged as nonlinear function and solved by iteratively to get chip flow angle η_c . It is solved in other equations after finding the chip flow angle.

$$\tan(\phi + \lambda_a) = \frac{\tan(i) \cos(\alpha)}{\tan(\eta_c) - \sin(\alpha)\tan(i)} \quad (23)$$

$$\tan(\eta_s) = \frac{\tan(i) \cos(\phi - \alpha) - \tan(\eta_c) \sin(\phi)}{\cos(\alpha)} \quad (24)$$

$$\beta = \tan^{-1}(\mu_a \cos(\eta_c)) \quad (25)$$

In the application of the stress distribution, the applied shear stress is constant and equal to sticking stress and the sliding stress is proportional to it with friction coefficient(μ).

$$\begin{aligned} \tau &= \tau_1 & x &\leq l_p \\ \tau &= \mu P & l_p &\leq x \leq l_c \end{aligned} \quad (26)$$

Rake face pressure distribution on BC plane is started at the tip of the grain. The momentum equation at the tip of the grain can be written as $M_{AB} = M_{BC}$. Considering these two equations (27,28), we can get the l_c contact length on the rake face.

$$M_{AB} = F_n \frac{AB}{2} = F_s h_1 \frac{\cos(\eta_s)(\tan(\phi + \beta - \alpha))}{2 \sin(\phi)} \quad (27)$$

$$M_{BC} = \int_0^{l_c} x P_0 \left(1 - \frac{x}{l_c}\right)^\zeta w dx = F_s \frac{l_c}{\zeta + 2} \frac{\cos(\eta_s) \cos(\eta_c) \cos(\beta)}{\cos(\phi + \beta - \alpha)} \quad (28)$$

Total contact length can be obtained as follows;

$$l_c = h_1 \frac{\zeta + 2}{2} \frac{\cos(\phi + \beta - \alpha)}{\sin(\phi) \cos(\beta) \cos(\eta_c)} \quad (29)$$

In order to calculate the normal force on the rake, the value of P_0 needs to be obtained. In this manner, normal forces are written in the form of normal pressure and shear force and P_0 is obtained depending on shear stress, uncut chip thickness and contact length on the rake face.

$$N = \int_0^{l_c} P_0 \left(1 - \frac{x}{l_c}\right)^\zeta w_c dx = P_0 \frac{w l_c}{\zeta + 1} \frac{\cos(\eta_s)}{\cos(i)} \quad (30)$$

$$N = F_s \cos(\eta_s) \frac{\cos(\beta)}{\cos(\phi + \beta - \alpha)} \quad (31)$$

Equations (30, 31) are equalized to obtain P_0 and formulation for it as follows;

$$P_0 = \tau_1 \frac{h_1(\zeta + 1)}{l_c} \frac{\cos(\eta_s)}{\sin(\phi) \cos(\eta_c)} \frac{\cos(\beta)}{\cos(\phi + \beta - \alpha)} \quad (32)$$

Once the pressure is obtained, the contact length division can be done with Coulomb friction coefficient μ on sliding to get sticking region length;

$$l_p = l_c - l_c \left(\frac{\tau_1}{P_0 \mu} \right)^{\frac{1}{\zeta}} \quad (33)$$

Force calculation on the rake face is divided into two parts with normal and friction forces. Friction force can be obtained with l_p by the formula as;

$$F = \int_0^{l_p} \tau_1 w_c dx + \int_{l_p}^{l_c} \tau_1 \left(1 - \frac{x - l_p}{l_e} \right)^{\zeta} w_c dx = \tau_1 w \left(l_p + \frac{l_e}{\zeta + 1} \right) \frac{\cos(\eta_c)}{\cos(i)} \quad (34)$$

The friction coefficient is calculated from the ratio of calculated frictional and normal forces.

$$\mu_a = F/N \quad (35)$$

In this solution process, the friction coefficient is scanned from 0.2 to 0.8. The apparent friction coefficient obtained when the difference between assigned and calculated value difference less than 0.01.

3.2.1.3 Cutting Forces and Shear Angle Calculation

Primary and secondary shear zone analysis are combined to calculate process forces with equations (36,37);

$$F_t = \frac{\tau_1 wh_1 (\cos(\beta - \alpha) + \tan(i) \tan(\eta_c) \sin(\beta))}{\sin(\phi) \sqrt{\cos^2(\phi + \beta - \alpha) + \tan(i) \tan^2(\eta_c) \sin^2(\beta)}} \quad (36)$$

$$F_n = \frac{\tau_1 wh_1 \sin(\beta - \alpha)}{\cos(i) \sin(\phi) \sqrt{\cos^2(\phi + \beta - \alpha) + \tan(i) \tan^2(\eta_c) \sin^2(\beta)}} \quad (37)$$

The shear angle calculation, which is the core parameter for the obtained force values, must be performed. The shear angle is calculated in thermomechanical force model from the assigned shear angle from 10 to 40 degrees with the given cutting parameters. Corresponding tangential force value is multiplied by the cutting speed to obtain required power to cut. According to minimum energy principle, a shear angle was chosen which gives the lowest value of the calculated power requirements. Shear angle vs. power graph shows how the shear angle was chosen. Shear angle is most affected by rake angle, in the following example the rake angle is considered -15 degrees to be suitable for grinding operations and calculated shear angle 17 degrees.

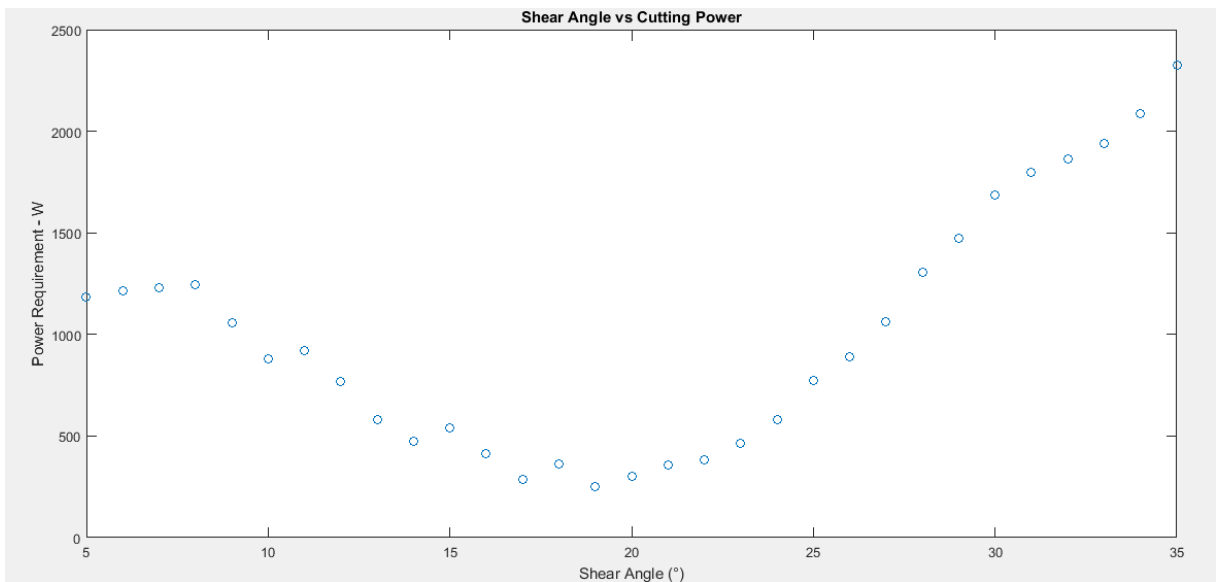


Figure 19: Sample shear angle estimation

In the machining operations, shear angle estimation is usually based on the experimental data. Traditionally Merchant approach has been used, but the model does not include negative rake angle effect. In another method for shear angle calculation from literature [71] is done on FEM with sensitivity analysis and the coefficient are calibrated to calculate the shear angle with the parameters as friction angle and rake angle;

$$\phi = 35.316 - 0.208(\beta - \alpha) \quad (38)$$

Despite these models in the literature, the model proposed in this study adds more parameter to the calculation of shear angle instead of trend fitting approaches. The correlation between thermomechanical model and calibrated formulation is checked on the simulation and adjusted according to it. Nevertheless, it gives inconsistent results at high negative rake angles such as -50 degrees, because the proposed model is tied to a certain cutting dynamics.

3.2.2 Edge Forces Thermomechanical Force Model

The presented oblique model is calculated by ignoring the influence of the edge radius on the primary and secondary deformation zones. However, two basic mechanisms influence the generated forces during the process; which are chip formation with the cutting of the material, and plowing as plastic and elastic deformation zone below stagnation point. Plowing forces on grinding operations can be negligible with less than 3% effect on total forces unless the operation is micro grinding with the depth of cut below 15 micrometers [71]. However, even at 5-micron depth of cut is considered, plowing forces are up to 15% of the total force. Although the third deformation zone is not very influential on the process forces, the chip formation and the results obtained by modeling the tool tip are more realistic.

The rake contact modeled as a straight line without the hone effect in the previous section. In this section, rake contact is modeled as a straight line and a curved shape originating from edge radius. Chip formation line BC is divided into three regions for the convenience of mathematical calculations, although second and third regions act as one unified region.

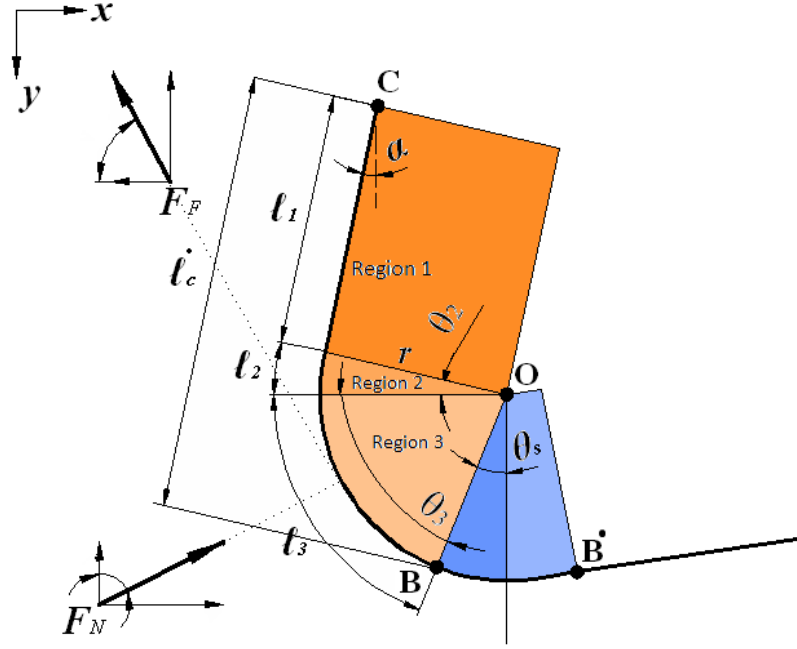


Figure 20: Edge force model on rake face with geometrical illustrations

The rake contact along with the edge radius effect is modeled as shown in Figure 20. The stagnation angle θ_s must be known to examine the chip formation along contact length l_c . The position of the stagnation point depends on the radius of the edge. Previous studies show that the stagnation angle in the metal cutting processes varies from 20 to 30 degrees [84]. In these operations where the rake angle is usually positive, the stagnation angle is considered equal to shear angle. However, the negative rake angles on grits are considered by the nature of the grinding operation. As described above, the calculation of α_{cr} requires minimum uncut chip thickness which can be obtained experimentally in conventional machining. Conversely, observing minimum uncut chip thickness in grinding operations is impossible because the resulting chip is so small with chip breakage even in the muddy powder form and also randomness will give inconsistent results. Basuray's [72] work with blunt tools investigated the effect of the negative rake angle on the stagnation angle, and it is predicted constant and equal to 37 degrees.

Contact length on the rake face is divided as illustrated in Figure 20. Assumed contact length l_c is calculated as in the previous section and r is the hone radius. The lengths of each region calculated by following equations;

$$l_c = l_1 + l_2 + l_3 \quad (39)$$

$$l_1 = l_c - r \cos(\theta_s - \alpha) \quad (40)$$

$$l_2 = r\alpha \quad (41)$$

$$l_3 = r(\pi/2 - \theta_s) \quad (42)$$

After the calculation of the contact lengths, the angular values of the regions formed by edge radius effect are calculated by the following equations;

$$\theta_2 = \frac{\chi}{r} - 90 + \theta_s \quad (43)$$

$$\theta_3 = \frac{\chi}{r} + \theta_s \quad (44)$$

The positioning angles are varying along regions in terms of χ .

3.2.2.1 Force Calculation on Rake Contact Regions

In this section, normal and friction forces acting on the rake contact for each region are calculated [85]. The force representations are shown in Figure 20, and each region represents derivation and orientation of them.

3.2.2.1.1 Forces on Region 1

The normal forces with the w as width of cut parameter defined as;

$$F_{N1} = \int_{l_2+l_3}^{l_c} P_0 \left(1 - \frac{x}{l_c}\right)^\zeta w dx \quad (45)$$

$$F_{N1x} = FN1 \cos(\alpha) \quad (46)$$

$$F_{N1y} = FN1 \sin(\alpha) \quad (47)$$

In the first region, chip contact on the rake face is either in sticking condition or in sliding condition. Calculated l_p sticking contact length which is investigated in the previous section is define the condition.

Only sliding friction force;

$$F_{F1} = \int_{l_2+l_3}^{l_c} \mu P_0 \left(1 - \frac{x}{l_c}\right)^\zeta w dx \quad \text{if } lp < l_2 + l_3 \quad (48)$$

Sliding and sticking friction force together;

$$F_{F1} = \int_{l_p}^{l_c} \mu P_0 \left(1 - \frac{x}{l_c}\right)^\zeta w dx + \int_{l_2+l_3}^{l_p} \tau_1 w dx \quad \text{if } lp > l_2 + l_3 \quad (49)$$

$$F_{F1x} = F_{F1} \sin(\alpha) \quad (50)$$

$$F_{F1y} = F_{F1} \cos(\alpha) \quad (51)$$

3.2.2.1.2 Forces on Region 2

The normal forces with the w as width of cut parameter defined as;

$$F_{N2x} = \int_{l_3}^{l_2+l_3} P_0 \left(1 - \frac{x}{l_c}\right)^\zeta \cos(\theta_2) w dx \quad (52)$$

$$F_{N2y} = \int_{l_3}^{l_2+l_3} P_0 \left(1 - \frac{x}{l_c}\right)^\zeta \sin(\theta_2) w dx \quad (53)$$

Only sliding friction force *if* $lp < l_3$;

$$F_{F2x} = \int_{l_3}^{l_2+l_3} \mu P_0 \left(1 - \frac{x}{l_c}\right)^\zeta \sin(\theta_2) w dx \quad (54)$$

$$F_{F2y} = - \int_{l_3}^{l_2+l_3} \mu P_0 \left(1 - \frac{x}{l_c}\right)^\zeta \cos(\theta_2) w dx \quad (55)$$

Sliding and sticking friction force together *if* $l_3 < lp < l_2 + l_3$;

$$F_{F2x} = \int_{l_p}^{l_2+l_3} \mu P_0 \left(1 - \frac{x}{l_c}\right)^\zeta \sin(\theta_2) w dx + \int_{l_3}^{l_p} \tau_1 w \sin(\theta_2) dx \quad (56)$$

$$F_{F2y} = - \left(\int_{l_p}^{l_2+l_3} \mu P_0 \left(1 - \frac{x}{l_c}\right)^\zeta \cos(\theta_2) w dx + \int_{l_3}^{l_p} \tau_1 w \cos(\theta_2) dx \right) \quad (57)$$

Only sticking friction force *if* $l_2 + l_3 < l_p$;

$$F_{F2x} = \int_{l_3}^{l_2+l_3} \tau_1 w \sin(\theta_2) dx \quad (58)$$

$$F_{F2y} = - \int_{l_3}^{l_2+l_3} \tau_1 w \sin(\theta_2) dx \quad (59)$$

3.2.2.1.3 Forces on Region 3

The normal forces with the w as width of cut parameter defined as;

$$F_{N3x} = \int_0^{l_3} P_0 \left(1 - \frac{x}{l_c}\right)^\zeta \sin(\theta_3) w dx \quad (60)$$

$$F_{N3y} = \int_0^{l_3} P_0 \left(1 - \frac{x}{l_c}\right)^\zeta \cos(\theta_3) w dx \quad (61)$$

Only sliding friction force *if* $l_p = 0$;

$$F_{F3x} = - \int_0^{l_3} \mu P_0 \left(1 - \frac{x}{l_c}\right)^\zeta \cos(\theta_3) w dx \quad (62)$$

$$F_{F3y} = - \int_0^{l_3} \mu P_0 \left(1 - \frac{x}{l_c}\right)^\zeta \sin(\theta_3) w dx \quad (63)$$

Sliding and sticking friction force together *if* $l_p < l_3$;

$$F_{F3x} = - \left(\int_{l_p}^{l_3} \mu P_0 \left(1 - \frac{x}{l_c}\right)^\zeta \cos(\theta_3) w dx + \int_0^{l_p} \tau_1 w \cos(\theta_3) dx \right) \quad (64)$$

$$F_{F3y} = - \left(\int_{l_p}^{l_3} \mu P_0 \left(1 - \frac{x}{l_c}\right)^\zeta \sin(\theta_3) w dx + \int_0^{l_p} \tau_1 w \sin(\theta_3) dx \right) \quad (65)$$

Only sticking friction force if $l_3 < l_p$;

$$F_{F3x} = - \int_0^{l_3} \tau_1 w \cos(\theta_3) dx \quad (66)$$

$$F_{F3y} = - \int_0^{l_3} \tau_1 w \sin(\theta_3) dx \quad (67)$$

3.2.2.1.4 Solution Procedure of Edge Forces and Cutting Forces

As discussed in the oblique modeling section, τ_1 is calculated in shear zone based on Johnson Cook material model with Runge-Kutta iteration method. The following parameters should be obtained for the calculation of process forces; P_0 normal pressure on rake face, contact lengths of the regions, sliding friction coefficient based on the coulomb friction with cutting speed relation and the last one is the apparent friction coefficient.

The normal and friction forces are obtained on the rake surface within hone radius effect. However, this distribution, which is caused by the edge radius, also includes the calculation of the equivalent rake surface different from the force distribution on the straight line rake contact. When calculating the equivalent rake angle c , the geometric approach over the merchant circle has been formulated as follows;

$$N_x = P_0 (F_{N1x} + F_{N2x} + F_{N3x}) \quad (68)$$

$$N_y = P_0 (F_{N1y} + F_{N2y} + F_{N3y}) \quad (69)$$

$$c = \tan^{-1} \left(\frac{N_y}{N_x} \right) \quad (70)$$

Once equivalent rake angle is calculated, the normal pressure P_0 is obtained by writing normal forces regarding normal pressure and shear stress as mentioned in the previous section.

$$N = \sqrt{N_x^2 + N_y^2} = F_s \frac{\cos(\lambda_a)}{\cos(\phi + \lambda_a - c)} \quad (71)$$

$$P_0 = \frac{F_s}{\sqrt{N_x^2 + N_y^2}} \frac{\cos(\lambda_a)}{\cos(\phi + \lambda_a - c)} \quad (72)$$

Momentum for contact length calculation is made on the centroid of the equivalent normal force $\tilde{\chi}$ to ease of calculation [40]. Same procedure in the oblique model is applied here, and momentum equilibrium between shear zone and rake zone $M_{AB} = M_{BC}$ is written as follows and contact length is calculated in the iteration loop.

$$M_{AB} = F_s h_1 \frac{\tan(\phi + \lambda_a - c)}{2 \sin(\phi)} \quad (73)$$

$$M_{BC} = N M_L \quad (74)$$

$$\tilde{\chi} = \frac{l_c}{\zeta + 2} \quad (75)$$

The momentum calculation on the rake face varies according to whether the centroid of the equivalent normal force is on the hone or not.

$$M_L = 2r \sin\left(\frac{\tilde{\chi}}{2r}\right) \sin\left(\theta_s + \frac{\tilde{\chi}}{2r} - c\right) \quad \text{if } \tilde{\chi} \leq l_2 + l_3 \quad (76)$$

$$M_L = \tilde{M}_L \sin\left(\tan^{-1}\left(\frac{\tilde{\chi} - l_2 - l_3}{r}\right) + \alpha - c\right) \quad \text{if } \tilde{\chi} > l_2 + l_3 \quad (77)$$

$$\tilde{M}_L = \sqrt{(\tilde{\chi} - l_2 - l_3)^2 + L^2 - 2L(\tilde{\chi} - l_2 - l_3)\cos\left(\frac{3\pi + 2\theta_s - 2\alpha}{4}\right)} \quad (78)$$

$$L = 2r \sin\left(\frac{\pi/2 - \theta_s + \alpha}{2}\right) \quad (79)$$

The last step is the calculation of apparent friction coefficient with the same iterative method on oblique one. Friction coefficient is obtained with the ratio of friction force to calculated normal force.

$$F = \sqrt{(F_{F1x} + F_{F2x} + F_{F3x})^2 + (F_{F1y} + F_{F2y} + F_{F3y})^2} \quad (80)$$

$$\mu_a = \frac{F}{N} \quad (81)$$

After all, parameters are iteratively obtained, cutting forces are calculated using the same method as in the previous section. Here, it is possible to calculate without using the oblique angle, which is utilized in the oblique model, and the orthogonal forces obtained as follows;

$$F_t = \frac{\tau_1 w h_1 \cos(\lambda_a - c)}{\sin(\phi) \cos(\phi + \beta - c)} \quad (82)$$

$$F_n = \frac{\tau_1 w h_1 \sin(\lambda_a - c)}{\sin(\phi) \cos(\phi + \beta - c)} \quad (83)$$

As a result of the calculations, a stationary thermomechanical model was prepared, and process forces were obtained. Now the adaptation of this mechanism into the grinding process at variable chip thickness investigation remains.

3.2.3 Grinding Application of Thermomechanical Force Model

The proposed model in the chapter 3.2.1 and 3.2.2 can be applied to other machining operations with an adaptation of the geometry. The geometry of the surface grinding operation is similar to plain horizontal milling operations if the random distribution of cutting particles are ignored and structured uniformly. Randomness is effective on rake angle, oblique angle height and width of the grit and most importantly on active cutting particles. Further investigation will be done in this section.

The procedure of adaptation of thermomechanical model into grinding operation is dealt with as follows. The force generated during each cutting grit was obtained by the uncut chip thickness, which is varied by the instantaneous immersion angle. Force is integrated on this chip thickness by dividing infinitesimal fragments. When the force on each grit on the circumference of the wheel is calculated, it is applied to the other particles on the wheel width which are cutting at the same and the resulting force is obtained.

In the approach of cutting mechanism, cutting grits are modeled within the range of measurement. In this model, the cutting particle distribution on the wheel is modeled according to the coefficient C . Idealized grinding tool has cutting grits evenly spaced with spacing factor L around the periphery of the wheel. For a tool 10 mm in diameter, the particles having a rake angle of -20 degrees at a height and width of 200 microns were visualized realistically with a cutting depth (a) of 100 microns in up grinding as follows.

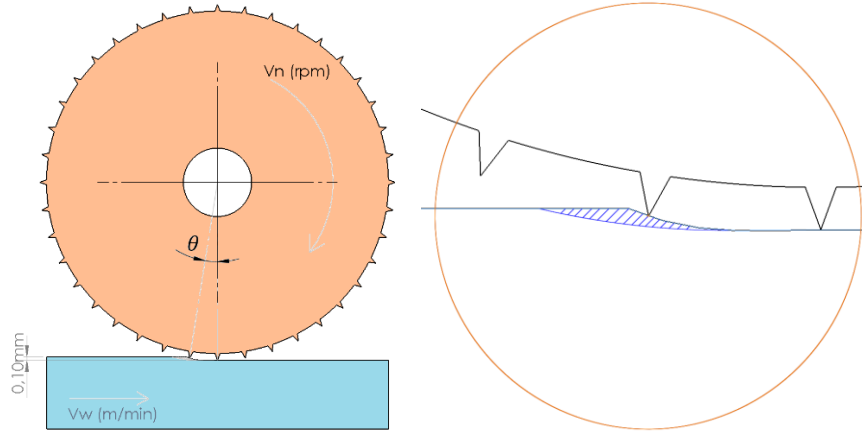


Figure 21: Grinding wheel illustration on cutting (a) operational image (b) uncut chip

Grinding wheel with diameter D rotating at constant V_n speed and the workpiece coming towards it with V_w speed. Instantaneous immersion angle θ is start from $\theta_{start} = 0^\circ$ and scan up to θ_{exit} , which is mainly depend on depth of cut and wheel diameter, but also on the lengths of the active grit height. θ_{exit} is formulated with grit effect as follows;

$$\theta_{exit} = \cos^{-1} \left(1 - \frac{a}{D/2 + h_{grit}} \right) \quad (84)$$

Grit height effect can be negligible for large wheels, but the effect is increased in smaller tools.

After the immersion angle is obtained, the simultaneous uncut chip thickness at each angle should be calculated. Tool path is modeled as a trochoidal trajectory in chip formation by cutting particles as seen in Figure 22. Cross section of uncut chip thickness was assumed that the cutter fragment behaved as rectangular on this trochoid path to ease of adaptation on the thermomechanical model and based on grit measurements. It is illustrated with grain width w and uncut chip thickness h as follows;

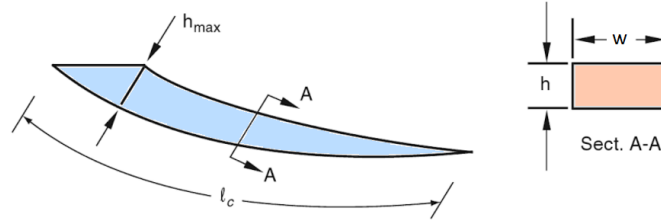


Figure 22: Uncut chip thickness illustration (a) side view (b) section view

The feed rate f_t is defined based on milling analogy and the number of cutting grit N_g on circumference defined by the equations;

$$f_t = v_w / (v_n N_g) \quad (85)$$

$$N_g = \pi D / (w_g + L) \quad (86)$$

When the feed rate is known, instantaneous uncut chip thickness can be calculated as follows in the traditional way.

$$h_i = f_t \sin(\theta) \quad (87)$$

Another way to model uncut chip thickness on the trochoid path as investigated in the geometric approach section is formulated. Also uncut chip thickness can be formulated basically as follows;

$$h_i = \sqrt{\frac{4 v_w}{Cr v_n} \sqrt{1 - 2 \sin^2(\theta/2)}} \quad (88)$$



Figure 23: Uncut chip thickness illustration with exaggerated time interval

Thermomechanical force model is applied to the each uncut chip thickness h_i part as shown in Figure 23 which is divided by $d\theta$. Force model operates for each θ with the corresponding uncut chip thickness until θ_{exit} reached. However calculated forces on thermomechanical force model need to be oriented into the absolute coordination system as shown in Figure 24 by these equations;

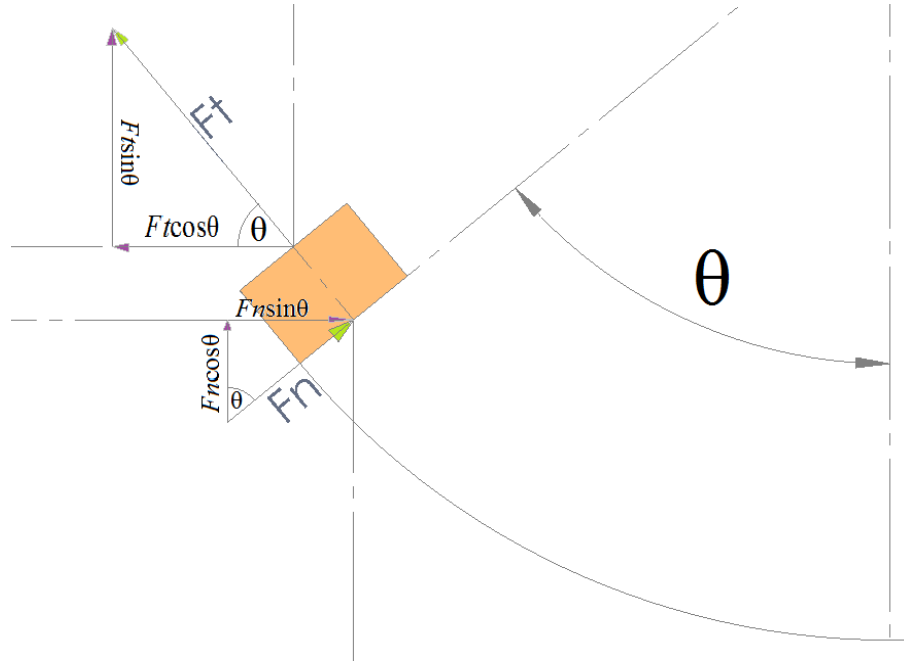


Figure 24: Force distribution to absolute coordination during immersion angle effect

$$F_T = F_t \cos(\theta) - F_n \sin(\theta) \quad (89)$$

$$F_N = F_t \sin(\theta) + F_n \cos(\theta) \quad (90)$$

The analytical thermomechanic force model is solved numerically for each infinitesimal part and multiplied by the transformation matrix and added together to obtain force per active grit. The total process forces are calculated as the sum of the generated forces by each grit which is cutting on the same contact length on the width of grinding wheel. In this manner, a total number of cutting particles on the contact length needs to be calculated. Number of active grits on the cutting zone is illustrated and formulated as follows;

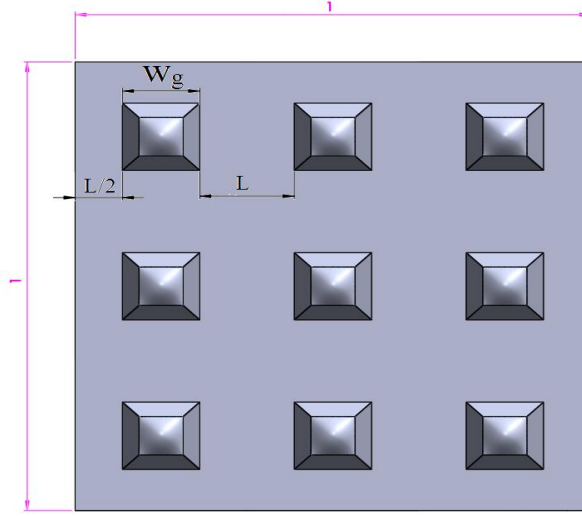


Figure 25: Grain distribution illustration on per area

$$L = \frac{1 - w_g \sqrt{C}}{\sqrt{C}} \quad (91)$$

Spacing factor L is calculated with the rectangular uniform distribution of the grit assumption on the measurement zone one-mm². If each cutting grit is considered to have average characteristics, total process forces can be calculated on the contact zone as follow;

$$TF_T = F_T \frac{wl_g}{(w_g + L)^2}$$

$$TF_N = F_T \frac{wl_g}{(w_g + L)^2} \quad (93)$$

In summary, the thermomechanic force model is investigated and adapted to the grinding operations by the uniform distribution of grains within micro milling analogy. First, single grain is used to find shear angle in oblique thermomechanical force model. After that, the value of shear angle is used in edge force model to find each grain forces which are uniformly distributed in height. As a contribution of this work, the thermomechanic force model is adapted to dynamic computation from static computation. In addition, total process forces has been formulated with the presence of active particles in the grinding zone which is described in Appendix A. Moreover, initial inception of force vibration is implemented to established force model and described in Appendix B.

4 3D TEMPERATURE DISTRIBUTION MODEL ON WORKPIECE WITH MOVING HEAT SOURCE

In this chapter, a three-dimensional analytical model depends on time for the thermal aspects of a grinding is presented. The complete model includes the previous chapter with the calculation of geometrical parameters and process forces. The calculated force is converted to total generated energy and distributed into the workpiece with heat partitioning model. Heat flux is modeled on the workpiece with based on that amount of heat on the workpiece as parabolic distribution in a rectangular cutting zone, when the heat flows on the workpiece is calculated and distributed in the cutting zone based on the grinding parameters. The temperature distribution on the workpiece is obtained by the finite difference method within the moving heat source theory and calculated with thermocouple coordination on the workpiece by time.

Atoms and interaction between them have existed since the beginning of the time. Philosophers and scientist examined it for ages; the four main principles of interaction between atoms were set forth. These are gravitational, electromagnetic, strong nuclear and weak nuclear interactions, and each of them should be considered in dynamic domains. The first two are mostly examined in the classical physics and the rest in the field of quantum. In the field of classical physics, the state of attraction between atoms creates energy output which can be in the different form of energy. In 1871, James Clerk Maxwell indicated that heat would pass from one body to another in the form of energy in motion at his book "*Theory of Heat*" which is summarize the lots of research on heat [86]. In those years, three laws of thermodynamics were established based on these foundations. This energy form, which is associated with motion, is a many different uncoordinated vibration modes or motion of individual molecules. The combination of these bonds between atoms or molecules creates a crystal structure which defines mechanical properties of the material in smallest scale. The

properties of the metallic crystal structure are commonly used in statistical mechanics. When the stress is applied on these bond, it can be deformed as plastically or elastically. Plastic deformation occurs when a minuscule part of these bonds breaks on the material. In fact, if all the crystal bonds in 10^{-21} m^2 area wanted to be broken; required stress would be 10GPa, whereas a glass would be broken with a stress of 70MPa. This plastic deformation, which is usually considered as cutting in machining, leads to heat energy during operation.

In the metal cutting process, plastic deformation is ensured by applying stress to the workpiece which is softer than cutting tool to create plastic deformation on the workpiece. Almost all of the mechanical energy used in the machining operation converted into thermal energy. The formation of heat take on the three zones; called as a primary, secondary and third zone. In the primary zone shearing is taking place; as the crystal structure is broken, plastic deformation induced heat arises in the shear plane. In the second region, friction heat is being held with the moving chip on the rake face with friction effect. In the third region, the heat is generated by the burnishing influence between flank of the tool and the machined surface. The distribution of this heat depends on material properties and the geometry of operation.

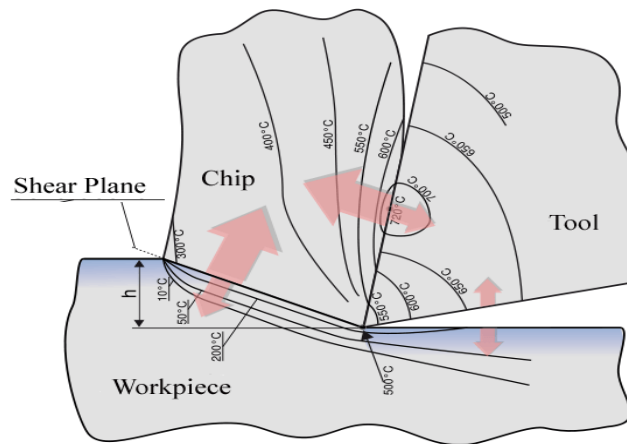


Figure 26: Temperature distribution for conventional machining [87]

In the conventional machining processes, the heat generated on the chip is increasing from the first region to the end of the second region. A large part of generated heat is carried out with a chip with conduction along the tool, so the temperature gradient on the tool is maximum during the operation as seen in Figure 26. However, in the grinding operations;

the time-dependent heat conduction onto tool is much smaller than workpiece compared to turning or milling. Negative rake angle causes the breakage in chips, so the heat flow mechanism between chip and tool should be occurred in smaller time in grinding. Besides all these, thermal diffusivity of CBN, Al2O3 materials used as a cutter in grinding much lower than tungsten carbide tools which lead to less temperature increase on the tool. The other way round, the generated temperature would go into the workpiece in this situation. This is why the temperature distribution on the workpiece during grinding operation is the motivation of this work. This study is based on the calculation of total energy during grinding which is converted into thermal energy. After that, we can apply the heat partitioning to predict what percentage of heat conducted into the workpiece. When constant heat flux is created on the workpiece, moving heat source theory used to model temperature distribution for temperature rise by coordination and time. The proposed analytical model in this study is solved by a numerical method.

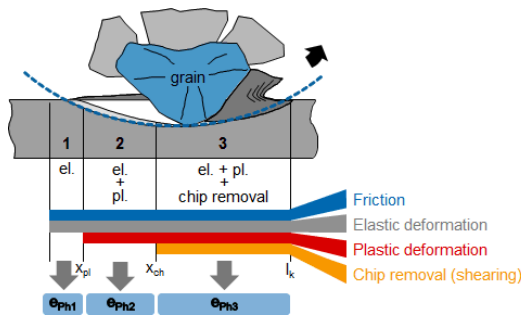


Figure 27: Heat generation during grinding [88]

One of the first studies on the grinding temperature belongs to Jaeger. The basis of the detailed temperature analysis in the grinding operation can be found in these studies [52]. Carslaw and Jaeger have approached to the problem starting from modeling the stationary point source to calculate temperature distribution. Adapting of this model to the moving heat source model was crucial in grinding operations. Generated heat during the chip formation examined by many researchers to predict temperature which is calculated by the slip theory. Despite the fact that the thermal aspects of the grinding were studied and researched by many, shadowy parts are remaining. The contribution of this work is the new way of calculation in grinding force with enhanced geometrical model and application of these into the temperature model to predict more accurate results with less calibration and measurement.

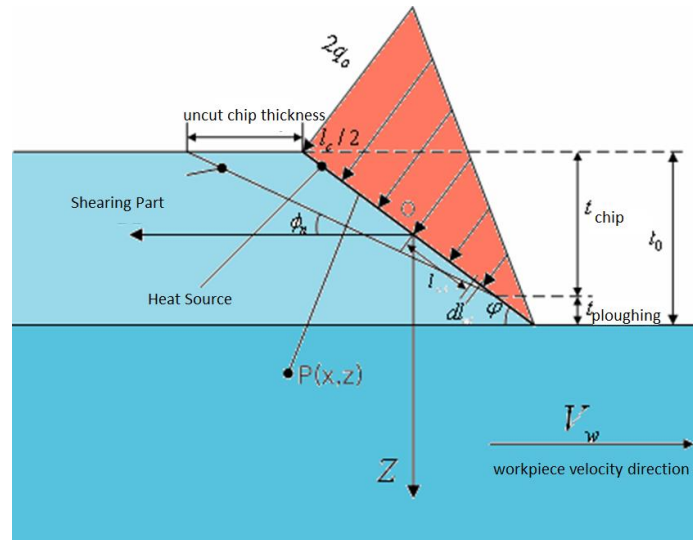


Figure 28: Triangular heat source illustration [52]

Thermal aspects of the grinding operation were studied whereafter, the calculation of the forces in regions. In this study, Jaeger's triangular moving heat source theory was examined to understand the basics of the temperature distribution. Thermally induced stress is applied within motion on workpiece by each abrasive cutting grit, depending on the workpiece and wheel material properties. During chip formation, the contact between workpiece and cutter occurs in a very short time, and it makes very difficult to analyze and measure separately. Stationary heat source model is considered at the beginning of the solution, and it is applied to the moving coordination. Numerous studies have been done on the heat source modeling as in linear, point, parabolic and triangular shapes. These studies have been experimentally investigated by researchers in grinding operations, and it has been observed that the triangular heat source approach for creep feed grinding and parabolic approach for high speed grinding gives the most consistent results [89].

In this manner, calculated force is converted into the specific grinding energy and this energy is distributed by heat partitioning with the following model. When heat flux into the workpiece is known parameter, temperature distribution with moving heat source model calculate the corresponding results.

4.1 Heat Partitioning Model on Grinding

Grinding energy is dissipated as a form of energy in heat at the grinding zone where the interactions between workpiece and grain are the main concern. Total energy should be known to calculate the amount of energy going into the workpiece with a fraction. Specific grinding energy produced in the grinding zone is calculated as the total power generated on the grinding within contact length. Total power analyses on grinding process based on multiplication of the grinding forces with a relative motion which is mainly the cutting speed (wheel linear speed- V_s) with negligible effect of workpiece speed (V_w). The normal direction that is often neglected in turning operations become critical in analyzing power consumption in grinding as described on force modeling [54]. Generated power is in Watt (Joule per second) and considered as a heat source in the cutting zone. The total heat flux (Watt per m²) is generated by the applying force on the deformation zones is expressed as following;

$$q_{total} = \frac{(\mu F_n + F_t)(V_s \pm V_w)}{l_c w_g 2 \cos(\theta_s)} \quad (94)$$

The assumption is the total energy generated in the grinding zone is distributed over the mediums according to the material properties. Total heat is partitioned over these bodies which applied by conduction into the workpiece, chip, cutting grit and by convection to coolants.

$$q_{total} = q_{workpiece} + q_{chip} + q_{grain} + q_{fluid} \quad (95)$$

The partition ratio of each segment can be expressed as the proportion of the total generated heat conducted into the body. The ratio of the total heat into workpiece R_w expressed as;

$$R_w = q_{workpiece} / q_{total} \quad (96)$$

Since the amount of heat removed by chips are considered as negligible based on many researchs, but it is still crucial for micro grinding [90]. Nonetheless, a theoretical model for energy partitioning can be considered between the workpiece and grinding wheel in dry surface grinding.

$$\frac{R_w}{(R_w + R_g)} = \left(1 + \frac{h_g}{h_w}\right)^{-1} \quad (97)$$

In the dry grinding operations, heat is transferred into three regions in total by neglecting convective heat loss. The assumption of specific absorption by chips tends to be small, and it can be assumed as $R_c = 6/q_{total}$ [91]. It can be seen that energy transfer to the chips will increase when specific grinding energy is lower for ferrous materials.

Generated heat tends to be moving towards the closest contact, and the contact length of grinding zone remains insignificant compared with the total convection area of the workpiece in grinding. The coolant fluid reduces the workpiece temperature effectively on the CBN grinding operations with convective heat transfer compare to conventional ones. Meanwhile, the CBN wheel absorb more heat comparatively, and the heat can be carried away with coolant more efficiently [92]. To sum up, effective partition coefficient for the workpiece written as follows;

$$R_w = \left(1 + \frac{h_g}{h_w}\right)^{-1} (1 - R_c - R_f) \quad (98)$$

Archard studied sliding contact frictions between materials and summed up in the solution of a heat transfer coefficient [93]. Abrasive grain and workpiece material interaction was modeled based on this assumption. Abrasive grain contact on the cutting zone has been modeled with a conical shape as illustrated in figure [94].

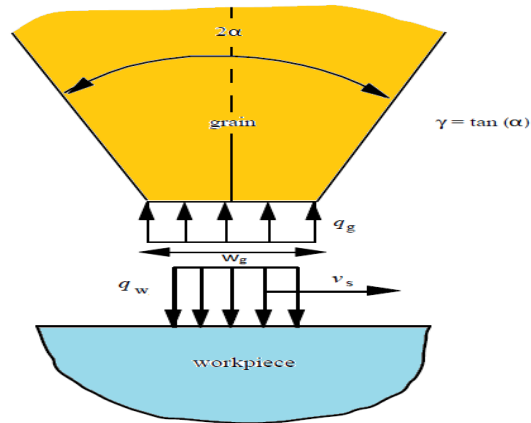


Figure 29: Grain-workpiece contact illustration during heat partitioning [22]

Lavine's solution for this geometry is applied on both workpiece and grain with the function of geometry and thermal diffusivity α . The following equations are used to calculate heat partitioning into the workpiece with neglecting lubrication.

$$R_w = \left(1 + f(\xi) \sqrt{\left(\frac{w_g/2}{l_c}\right) \left(\frac{(\kappa\rho c_p)_g}{(\kappa\rho c_p)_w}\right)} \right)^{-1} \quad (99)$$

$$f(\xi) = \frac{\xi^3}{1 + \xi^2 - (2/\pi^{1/2})\xi - e^{\xi^2} \operatorname{erfc}(\xi)} \quad (100)$$

$$\xi = \sqrt{\frac{2\gamma^2 \alpha l_c}{w_g V_s}} \quad (101)$$

Where thermal properties κ , thermal conductivity and c_p , specific heat capacity should be defined in order to evaluate the heat partitioning ratio. In this manner, following Table 2 gives information about the materials usually used for this study and tungsten carbide for comparison conventional machining.

Materials	Thermal Conductivity (W/mK)	Specific Heat Capacity (J/kgK)	Density (kg/m ³)	Thermal Diffusivity (mm ² /s)
AISI 1050 Steel	51,90	486,00	7870,00	13,57
Inconel 718	12,80	435,00	8190,00	3,59
CBN	30,00	1610,00	1900,00	9,81
Al2O3	18,00	880,00	3720,00	5,50
Tungsten Carbide	58,00	238,00	14800,00	16,47

Table 2: Thermal properties of workpieces and tools

Thermal diffusivity of the material defines roughly what percentage of heat energy will be absorbed by this material at a time. As seen in the table; tungsten carbide, which is mainly used in conventional machining operations, tends to heat up when compared to grit materials.

Model is validated with the literature data. Contact length is changed according to a depth of cut and given parameters as in Rowe experiments [51]. The depth of cut is proportional to contact length which is calculated by the geometrical model as discussed earlier and the

contact length is proportional to the conduction band. When the l_c is increasing, the more heat conducted into a wheel within enhanced time and area on contact. The fraction of heat passing into the workpiece will be reduced as the wheel partitioning increase. It is confirmed when the experimental results are compared with the model results in following figures.

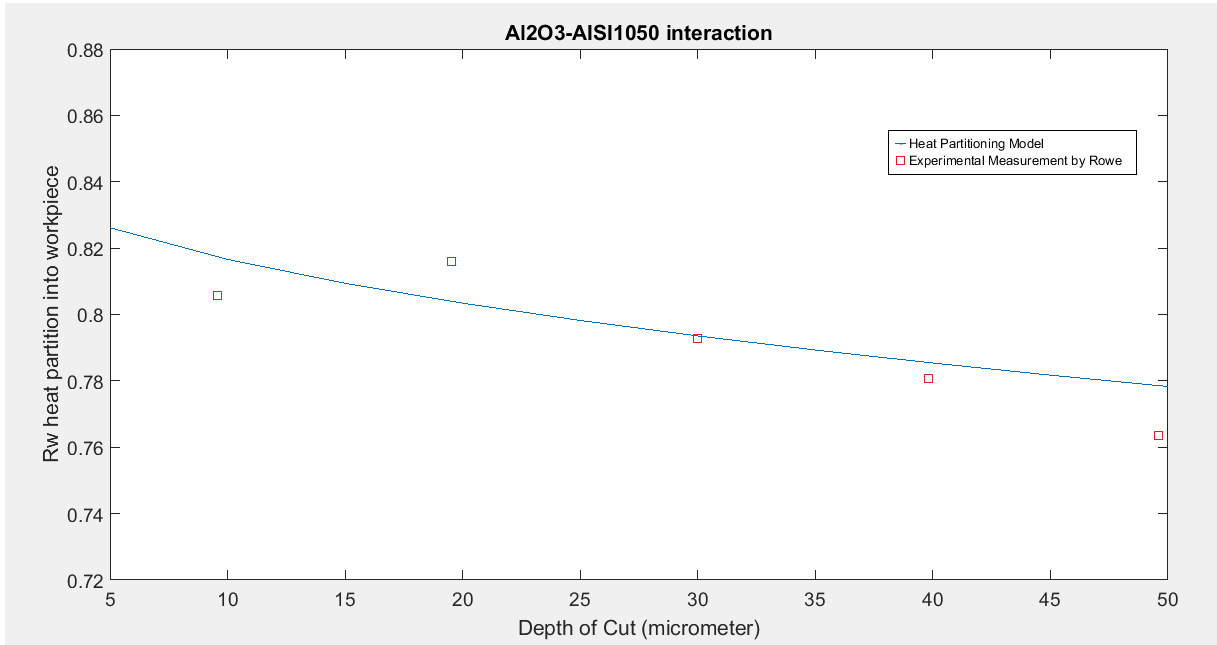


Figure 30: AL2O3 vs. AISI1050 heat partitioning simulation with different depth of cut

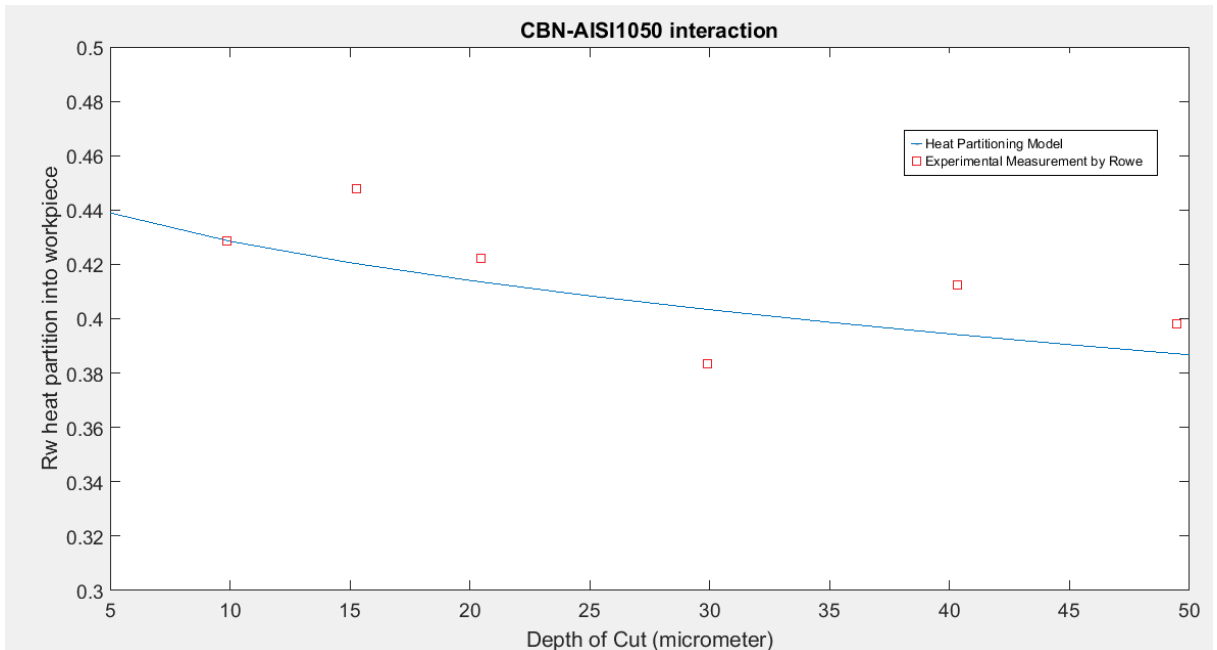


Figure 31: CBN vs. AISI1050 heat partitioning simulation with different depth of cut

Simulation results for CBN and Al₂O₃ show compatibility with the literature. Al₂O₃ has an average value of 80% for heat partition on the workpiece, whereas 40% heat partitioning is obtained when CBN wheel is used. The usage of CBN wheels has a significant advantage to minimize thermal damage to the workpiece and suitable for more reliable residual stress control.

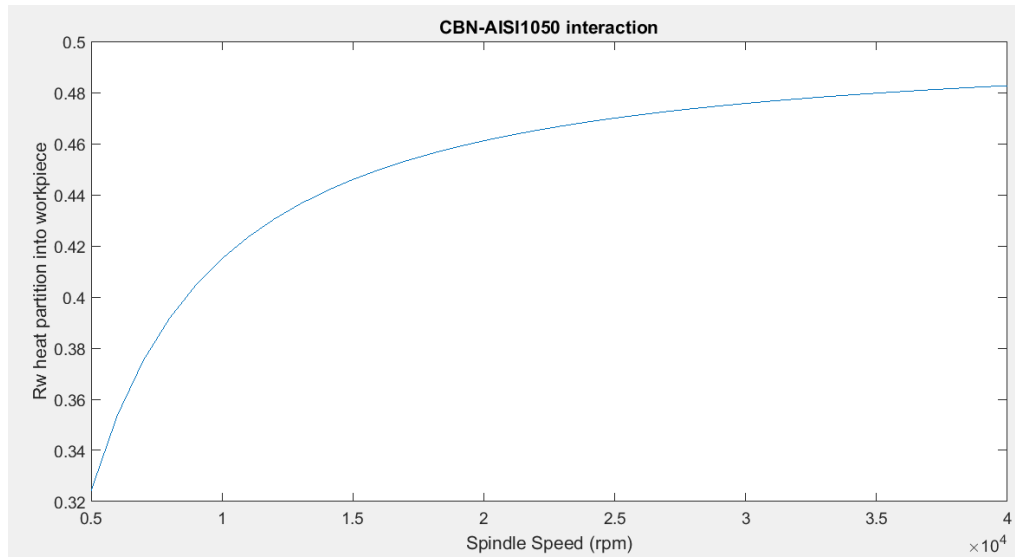


Figure 32: CBN vs. AISI1050 heat partitioning simulation with different spindle speed

CBN wheels are usually considered in high-speed machining with corresponding spindle speed. In this work, heat partitioning ratio is simulated on different spindle speed and the results are shown in in Figure 32. The phenomenon of thermal conduction are time dependent, and contact time with tool and workpiece will drop at high speed. It leads to increasing of heat transfer into the workpiece. This increase was up to 90% in Al₂O₃ wheels while CBN tools up to 48% in the maximum speed of the machine which is used in this study.

4.2 Temperature Distribution Model

The temperature distribution model is derived from the moving heat source theory. The inputs of the model are heat rate, thermocouple coordination, workpiece dimensions, workpiece speed, and cutting area. Thermocouple coordination, dimensions of workpiece and workpiece speed is user inputs. The total cutting contact area is defined by the geometrical model. Heat rate is the important part to develop a consistent model, and it is calculated from thermomechanical force model and partitioned by heat partitioning model above. When the constant heat source on the workpiece is derived as described, the temperature distribution on the workpiece is taken place.

In this section, general solutions for the transients state and corresponding temperature rise on the workpiece are derived. The rectangular shape parabolic plane heat source occurred in the grinding zone, and it is formulated in this study. The present model starts with a dividing variables into a three-dimensional space within stationary point heat source solution. In this study, the convective term is associated as small with relative workpiece speed and conduction band analyses. Point heat source solution is obtained with this approximation. Temperature rise solution for the point heat source is applied in integral, and the calculated initial values as the contact area, and heat source are integrated into the model to obtain temperature solution. Obtained temperature distribution solution for point heat source is further expanded to the moving heat source with the modeling heat source as a plane in parabolic distribution, and the moving coordination approach is used to obtain time-dependent three-dimensional temperature distribution on the workpiece within moving heat source model.

4.2.1 Stationary Point Heat Source Model

The heat transfer problem starts with a solution of the stationary point heat source on the workpiece, and the heat equations are solved in one-dimensional time-dependent solution. Assumptions for constructed models are; independence for mechanical properties of the material which are density ρ , specific heat capacity C_p and thermal conductivity K , and the workpiece is defined as an infinite body in x and y directions. The workpiece speed v_w is

taken as a heat source based on the relative motion between the body and heat source. The general heat equation can be applied to the grinding zone with the subsequent energy equation (102);

$$\rho C_p \frac{\partial T}{\partial t} - \nabla(K \nabla T) + \rho C_p v_w \frac{\partial T}{\partial x} = 0 \quad (102)$$

In the first place, the convective term is ignored in the analytical solution of fixed system without relative motion. Then it will be adapted into the system in the moving heat source solution.

General temperature solution can be written in terms of x and t in the form of linear differential equation, and combination with the equation (102) gives one-dimensional energy equation (103) as follows;

$$\frac{\partial^2 T_x(x, t)}{\partial x^2} = \frac{1}{\alpha} \frac{\partial T_x(x, t)}{\partial t} \quad (103)$$

The solution of this equation can be found on Jaeger's "*Conduction of Heat in Solids.*" Particular solution of the one-dimensional temperature rise explanation converted into a general equation (104) as follows;

$$T_x(x, t) = \frac{1}{\sqrt{\pi}} \int_{-\infty}^{\infty} C(x + \eta \sqrt{4\alpha t}) e^{-\eta^2} d\eta \quad (104)$$

$$\eta = \frac{\dot{x} - x}{\sqrt{4\alpha t}}$$

If the initial conditions are defined as $f_x(x)$ the equation (105) can be written as temperature rise solution in one dimension;

$$T_x(x, t) = \frac{1}{\sqrt{4\pi\alpha t}} \int_{-\infty}^{\infty} f_x(\dot{x}) e^{-\eta^2} d\dot{x} \quad (105)$$

The initial state is associated with the produced heat in the contact point between grit and workpiece; the produced heat energy is already calculated via heat partitioning along with thermomechanical total energy calculation. Initial condition is applied via Dirac's delta

functions, which are suitable for time domain concept, and the temperature distribution on one dimension for the stationary point heat source q_{pt} (J/s) is equated as;

$$T_x(x, t) = \frac{q_{pt}}{\rho C_p \sqrt{4\pi\alpha t}} \int_{-\infty}^{\infty} e^{-\frac{(x-\dot{x})^2}{4\alpha t}} \delta(\dot{x}) d\dot{x} \quad (106)$$

4.2.2 Moving Heat Source Model for Point Heat Source

Equation (14) is used to express temperature distribution on the workpiece as stationary point heat source. In this section, the equation is introduced into moving plane to create moving heat source. Moving direction and speed of the heat source is assumed as equal to the workpiece speed v_w while spindle fixed at the position.

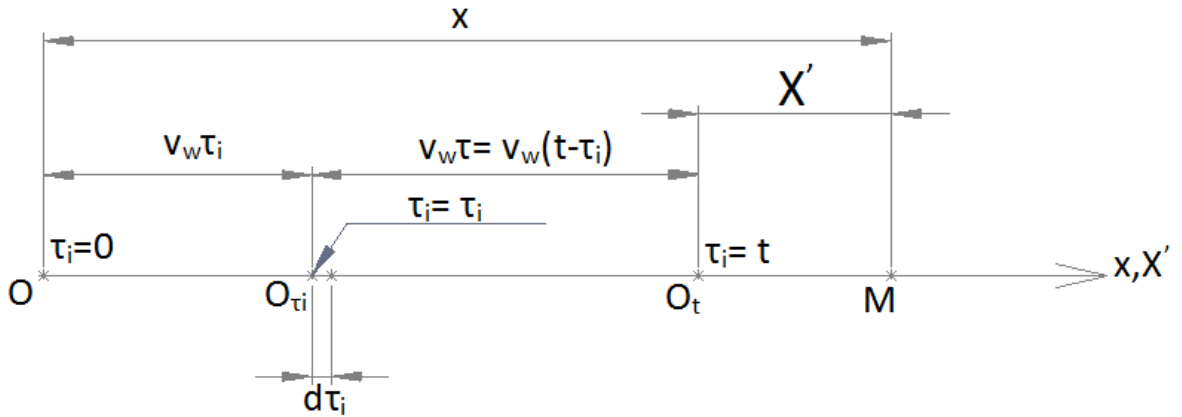


Figure 33: Moving coordination system in x direction

The point heat source is moving at speed v_w in the x direction until observation time t is reached. Temperature estimation is obtained for point M as thermocouple position from time zero to t . Coordination system is shifted for each time interval $d\tau_i$. If point heat source is moved for a time τ_i , then the new origin of the system will be O_{τ_i} . In the mean time, remaining time for observation τ can be calculated as $(t-\tau_i)$. When heat source is reached to the observation time, temperature distribution was investigated for each infinitesimal time period $d\tau_i$ with the following equation.

$$dT_x = \frac{q_{pt}d\tau_i}{\rho C_p \sqrt{4\pi\alpha\tau}} e^{-\left(\frac{X'}{4\alpha\tau}\right)} \quad (107)$$

Geometric relationships between coordination and parameters can be expressed as follows;

$$x - v_w\tau_i = x - v_w(t - \tau) = (x - v_w t) + v_w\tau \quad (108)$$

$$X' = x - v_w t \quad (109)$$

$$x - v_w\tau_i = X' + v_w\tau \quad (110)$$

Time-dependent moving point heat source solution for temperature on point M can be obtained by integrating the equation (107) with the above geometric relations. Temperature rise depend on x and t are given as follows;

$$T_x(x, t) = \frac{q_{pt}}{\rho C_p \sqrt{4\pi\alpha t}} \int_0^t \frac{1}{\sqrt{\tau}} e^{-\left(\frac{(X'+v_w\tau)^2}{4\alpha\tau}\right)} d\tau \quad (111)$$

Adaptation of this solution into a three-dimensional solution is made by using Dirac's delta functions for each direction. Consideration is taken only in the x direction along with the movement; the following equation can be used in the temperature distribution of the moving point heat source on the workpiece.

$$T(x, y, z, t) = \frac{q_{pt}}{\rho C_p (\sqrt{4\pi\alpha t})^3} \int_0^t \left(\frac{1}{\sqrt{\tau}}\right)^3 e^{-\left(\frac{(X'+v_w\tau)^2 + y^2 + z^2}{4\alpha\tau}\right)} d\tau \quad (112)$$

The above equation cannot be solved analytically. In the literature, a numerical solution for temperature distribution is obtained from the non-dimensional equation, but it was time independent in Jaeger's solution. In order to obtain a time-based solution, the following variable substitution method is used, and the obtained equation is solved numerically.

$$T(x, y, z, t) = \frac{q_{pt}v_w}{16K\alpha\pi^{3/2}} e^{-\frac{X'v_w}{2\alpha}} \int_0^{v_w^2 t/4\alpha} \left(\frac{1}{\sqrt{w}}\right)^3 e^{-\left(w+\frac{u^2}{4w}\right)} dw \quad (113)$$

Where,

$$w = \frac{v_w^2 \tau}{4\alpha} \quad (114)$$

$$u = \frac{v_w \sqrt{X'^2 + y^2 + z^2}}{2\alpha} \quad (115)$$

Temperature distribution solution for moving point heat source is presented in equation (113).

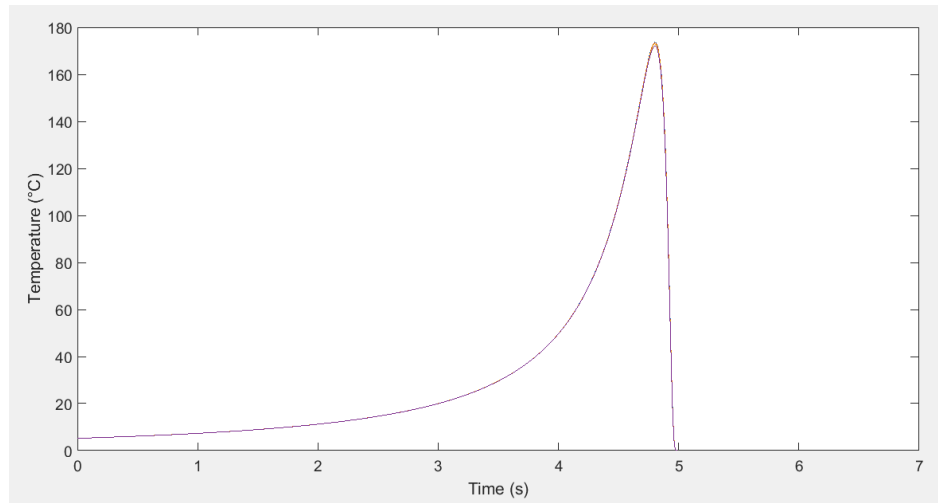


Figure 34: Moving point heat source simulation

The simulation results in this method as in Figure 34, but there is a problem with $w=0$ singularity value and after the temperature reached maximum it gives sharp decrease which is far from reality. In this study, numerical solution is adapted to overcome this problem, as explained in the next section.

4.2.3 Heat Flux Model into Temperature Distribution

Temperature distribution on the workpiece is depended on the heat flux shape and distribution. Jager used triangular heat flux for quasi-state solutions, but different models were developed in the literature since the time-dependent heat flow is changing during movement. In this study first assumption is that a heat source is a plane which is parallel to the workpiece with small angle approximation since thermocouple measurements were done on this surface. Trochoid path of the chip defines the heat flux plane on the workpiece, and it should have more complex geometry than uniform plane. Heat generation increases with the corresponding chip thickness increase. It can be seen that the projected heat flux on the moving plane is parabolic distribution instead of triangular or normal distribution, considering the heat generation on deformation zones.

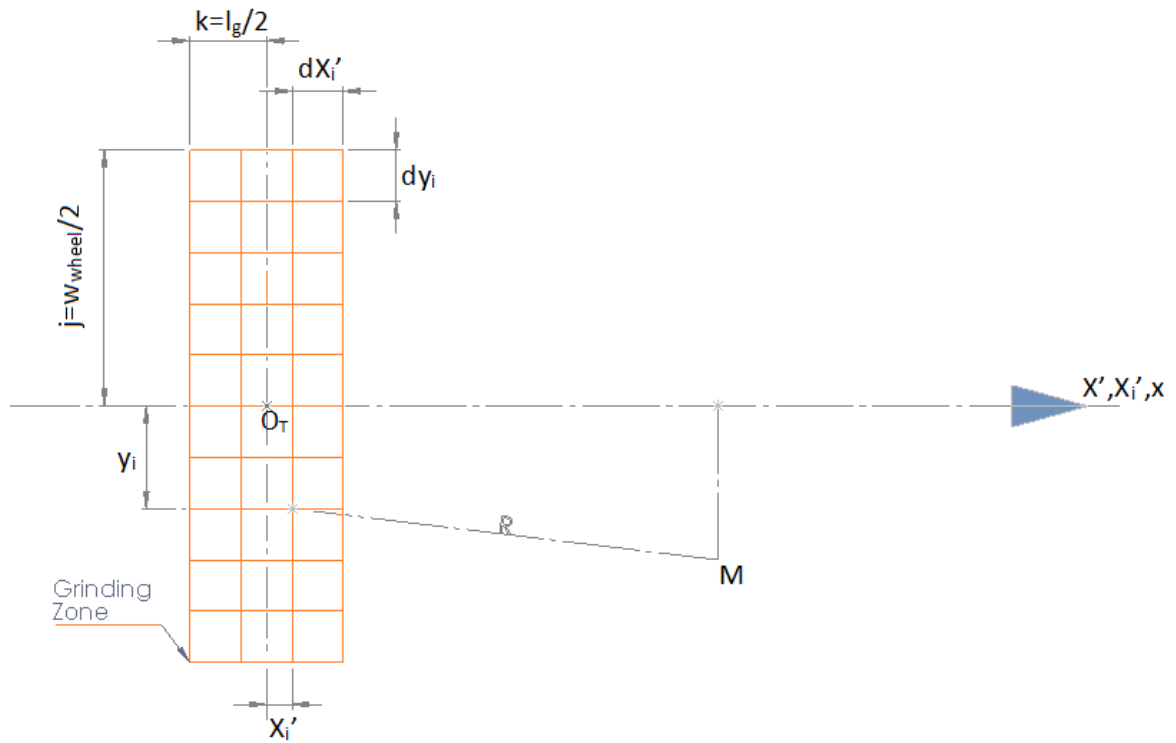


Figure 35: Heat flux distribution on moving coordinate system

Top view of the grinding zone is illustrated in Figure 35 where grinding zone length l_g and wheel width as w_{wheel} . Heat flux is modeled on this zone with corresponding segments of lengths dX_i' and dy_i . Each node on this zone represents a heat source if generated heat is

distributed in this zone with a corresponding coordinate based function starting from O_T . Heat rate for each segment can be attained as in equation (116) if the distribution is uniform as illustrated in Figure 36.

$$q_{segment_uniform} = \frac{q_{workpiece}}{w_{wheel}l_g} dy_i dX_i' \quad (116)$$

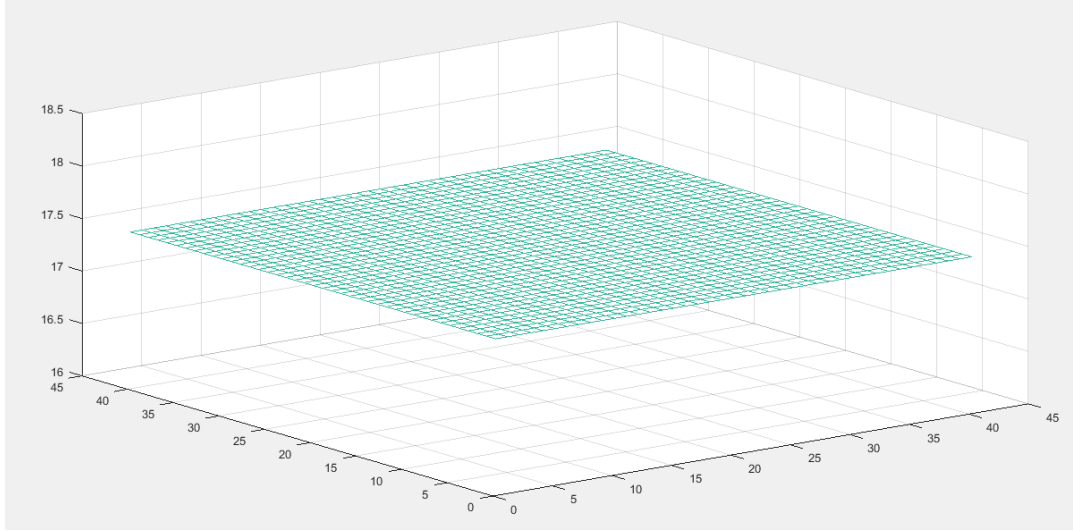


Figure 36: Uniform heat source distribution

On the other hand in the case of functional representation of the heat flux requires $q_{segment}$ calculation with respect to the function to acquire total heat flux unchanged. Total heat flux adjustment coefficient can be modeled within a double integral to find correction value for segments;

$$Total_{coefficients} = \int_{-j}^{+j} \int_{-k}^{+k} distribution_function(f, g) df dg \quad (117)$$

$$q_0 = \frac{q_{workpiece}}{Total_{coefficients}} dy_i dX_i' \quad (118)$$

Temperature rise with triangular heat distribution can be calculated as Jaeger's model with using above equations, but in this study time-dependent transient state is investigated instead of quasi-steady state analyses as in literature. Time-dependent investigations in literature are limited with distribution until the maximum temperature is reached, because of the singularity problem is occurring at that point. In this study, the full solution is presented with

the elimination of the singularity in the analytical calculation with a combination of analytical Bessel solution and numerical solution. As a result, after the maximum temperature reached decreasing temperature profile can be predicted. Triangular solution with investigating single thermocouple position with heat distribution illustration on the grinding zone as follows;

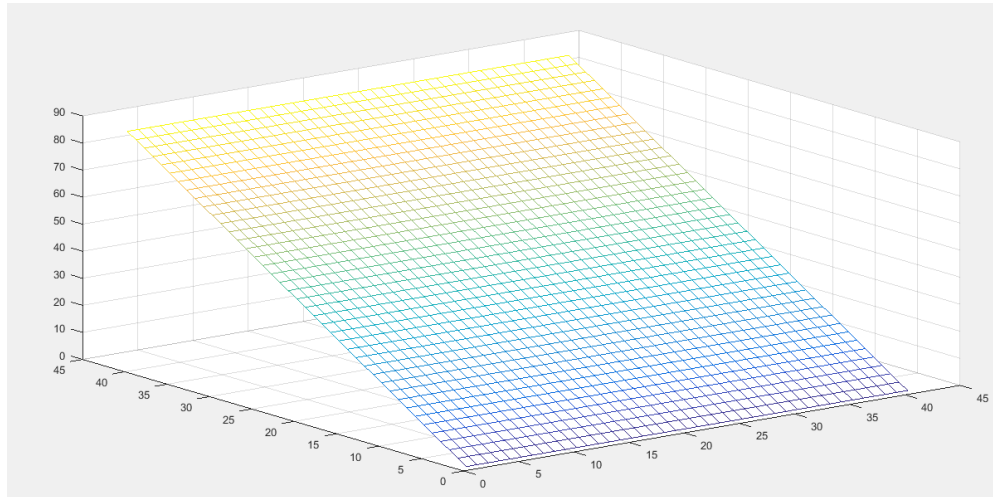


Figure 37: Triangular heat distribution

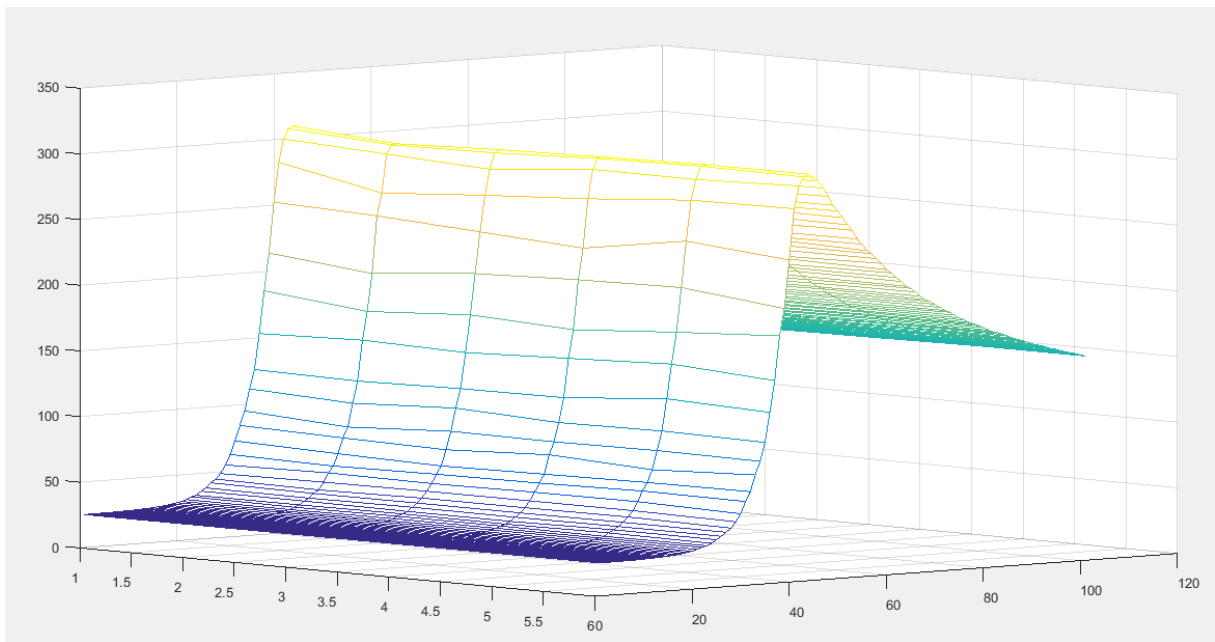


Figure 38: Heat distribution with triangular heat source considering one thermocouple

Moving heat plane is integrated into the 3-D moving point heat source solution as formulated above. As a result, time-dependent 3D temperature distribution solution with parabolic moving heat source formulated as follows;

$$T(x, y, z, t) = \frac{q_0 v_w}{8K\alpha\pi^{3/2}} \int_{-j}^{+j} A \int_{-k}^{+k} B e^{-\frac{(X' - X_i')v_w}{2\alpha}} \int_0^{v_w^2 t / 4\alpha} \left(\frac{1}{\sqrt{w}}\right)^3 e^{-\left(w + \frac{u_i^2}{4w}\right)} d\tau dy_i dX_i' \quad (119)$$

Where,

$$u_i = \frac{v_w}{2\alpha} \sqrt{(X' - X_i')^2 + (y - y_i)^2 + z^2} \quad (120)$$

$$A = 1 \text{ and } B = e^{-\left(\frac{3\pi X_i' - 1}{12k}\right)^2} \quad (121)$$

In this study, the heat distribution depends on the function for flexible usage and A multiply B is described as a distribution function. In the literature, the distribution is modeled as triangular, normal distribution or uniform distribution. However, this flexibility gives possible usage of some heat distribution estimation like heat distribution estimation which is obtained by reverse engineering [54]. The reverse engineered heat flux model is used by the equation (117), and it is illustrated with the result temperature distribution on workpiece as follows;

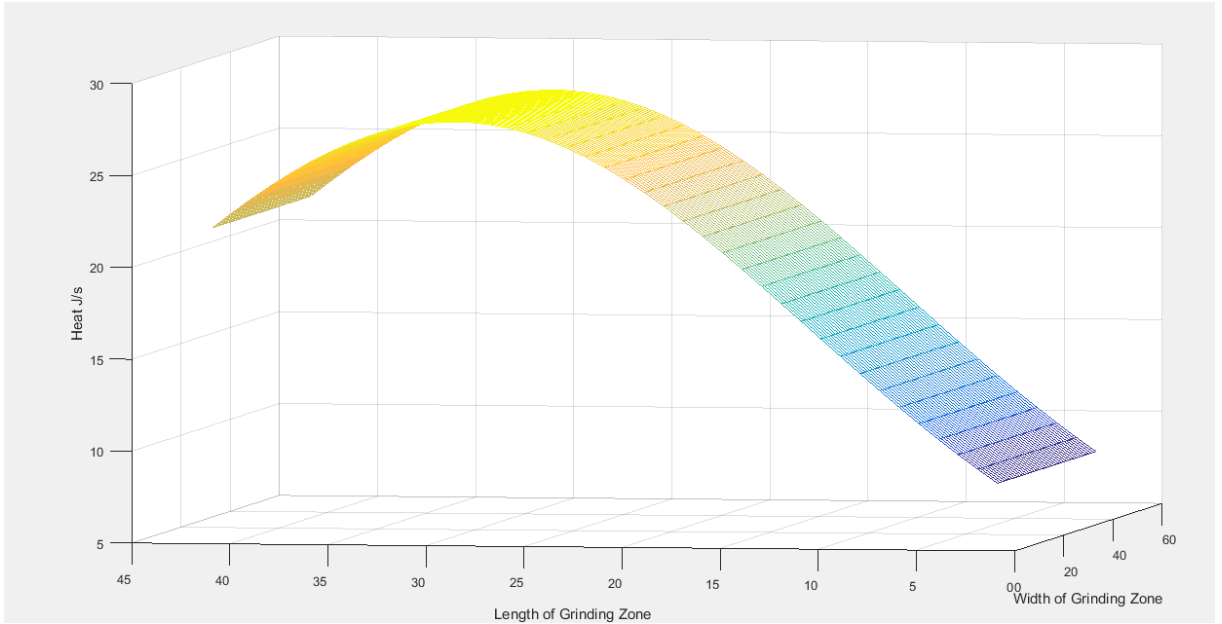


Figure 39: Heat distribution model inspired by Malkin reverse engineering study

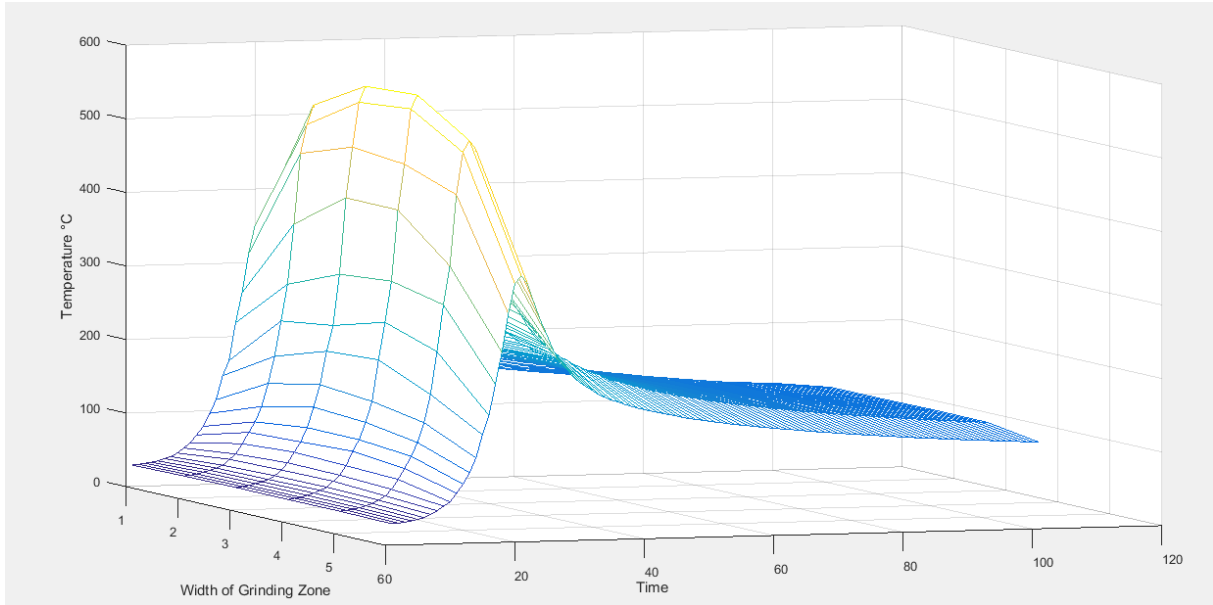


Figure 40: 3D temperature distribution on workpiece considering $z=0$

In Figure 40, thermocouple x position is fixed in one cm away from the origin of the 5 cm long workpiece, and workpiece speed is attained as 50mm/min, and corresponding grinding length l_g is calculated as 3 mm with corresponding $q_{\text{workpiece}}=3.28e7 \text{ W/m}^2$. Temperature distribution along the y-axis is investigated in these conditions, and the pick temperature is observed in the middle of the workpiece as expected. Since active cutting grits are distributed on grinding zone and magnitude of equivalent distance from these source in the y direction is smallest at the mid of workpiece and largest at the edge of grinding zone. The results are investigated in the next section with more detailed and validation with experiments.

In summary, the temperature distribution on the workpiece is modeled with moving heat source theory and grain-based heat partitioning model. As a contribution of this study, heat flow is modeled with the effect of friction on the secondary shear zone and third deformation zone with the help of thermomechanical force model outputs and geometric model outputs. As a new approach, heat flow on the workpiece, which is obtained with literature heat partitioning model, distributed parabola inspired by reverse engineering on the rectangular grinding zone. In addition, the solution procedure is applied with the combination of second kind of Bessel solution and numeric approach of analytical solution to achieve time dependent 3D full temperature distribution.

5 MODEL DISCUSSION AND EXPERIMENTAL VERIFICATION

In this chapter, the proposed models are investigated in different states with corresponding grinding conditions and verified by several experiments in force and temperature measurements.

5.1 Model Discussion

The ultimate goal of this work is to obtain temperature distribution on the workpiece by heat flux which is partitioned power from thermomechanical force model. In this context, geometric model, thermomechanical force model, heat flux and partitioning model and finally temperature distribution with moving heat source model have been established. Geometry model provides grinding zone length l_g and *uncut chip thickness* h parameters for other models. Thermomechanical force model supplies tangential and normal forces with the calculated shear angle, friction angle, and the equivalent rake angle. Heat partitioning and heat flux model combine the force and geometric parameters to generate total heat, and calculate the heat flux into the workpiece depend on material properties and grinding parameters. When the heat flow into the workpiece was found, the temperature distribution model provides solutions within time-dependent three-dimensional adiabatic conditions.

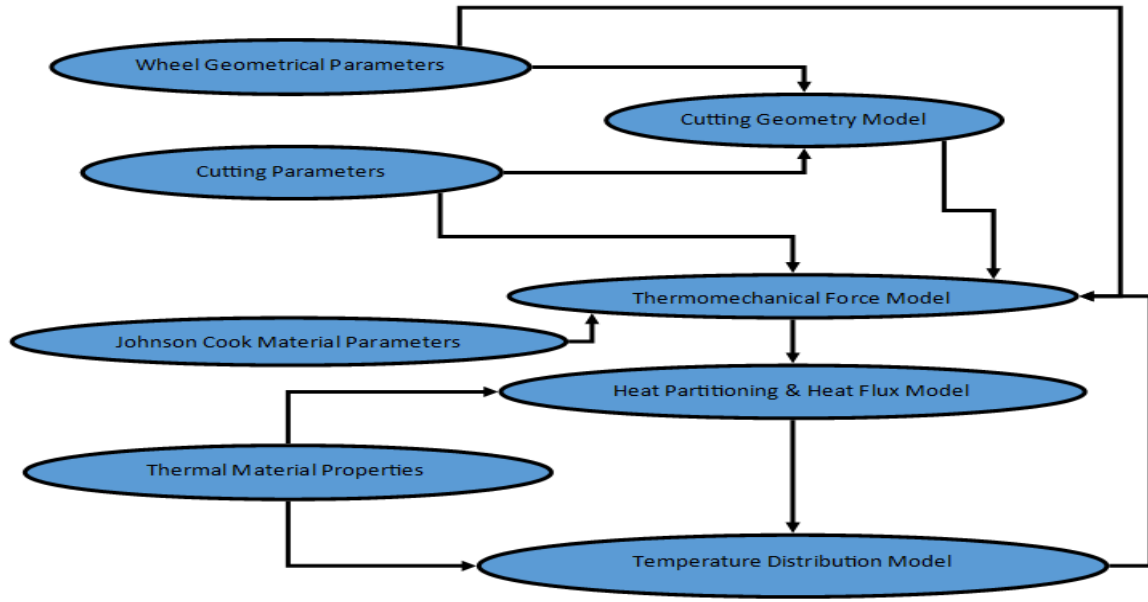


Figure 41: Working diagram of the models

The coolant effects are considered within heat partitioning effect and can be modeled as Vashista's [95]. In this study, the predicted temperature on the process, which is used in the thermomechanical model to predict force, is oriented via combining these models together within the minimum energy principle. In the working way of established models, the process parameters are obtained more precisely.

In this section, the discussion of proposed models is carried with the following grinding parameters in Table 3. The experimental validations for proposed models will be given in the next section.

Grinding Conditions - Up Grinding		
Wheel Diameter, D_s	254,00	mm
Wheel Width, W_{wheel}	7,58	mm
Depth of cut, a	100,00	micron
Wheel velocity, V_s	53,19	m/s
Workpiece moving velocity	30,00	mm/min

Table 3: Grinding conditions for model investigations

5.1.1 Calibration of material model parameters

The Johnson Cook parameters are used for the calculation of primary deformation zone. Shear stress calculation on the shear plane is done by the calculation of the material stress and strain relation within plastic deformation. Each material has unique properties in different conditions, assumptions for primary deformation zone is already given in force model chapter to limit these effects. In this study, common materials are investigated and calibrated for grinding operations as follows;

Material	A(MPA)	B(MPA)	n	m	v	Tmelting (°C)
AISI 1050 Steel	860	500	0,234	0,0134	1	1450
Inconel 718	450,00	1700,00	0,65	0,017	1,30	1570,00
Ti6Al4V	782,70	498,40	0,25	0,03	1,00	1660,00

Table 4: Johnson-Cook material model parameters

The Johnson-Cook material model parameters calibration is effective on the modeling nonlinear regression analysis of shear stress calculation. The parameters for the Johnson-Cook model are obtained from Split Hopkinson Bar Tests in the literature. However, the indication of using these values can end up with inaccurate results, since the cutting geometry has another mechanism to predict this plastic deformation stress. On the other hand, comparing the results with experimental cutting values and calibration of these values can deduce good results.

5.1.2 Calibration of sliding & sticking friction coefficients

The friction models which are used in the dual-zone model to predict process forces as discussed in force chapter. Friction on the cutting grits comes out in three different way, which are sliding, sticking and the combination of these two. Sliding friction, which is mostly proportional to the cutting speed, calculated with Coulomb friction laws. Even in slow cutting speeds sliding friction is observed in the simulations and experiments [96]. Non-cutting tests are conducted at different cutting speeds to predict sliding friction coefficients depends on the contact materials and cutting speeds for CBN-Inconel718 contact. Coulomb friction coefficients for the different material is investigated and calibrated as in Table 5.

Material – Tool	μ_s (V in m/min)
AISI 1050 – CBN	$0,431-0,0007*V$
Inconel 718 - CBN	$0,1484+0,0061*V-0,0002*V^2$
AISI 1050 – Al2O3	$-0,167-0,00092*V^2+0,057*V$
AISI 1050 – SIC	$0,362+0,001*V-0,0003*V^2$

Table 5: Sliding friction equations for different materials

The determination of friction between the abrasive grains and workpiece is an essential element to predict grinding process outputs as force and temperature which are also effective on the wear, surface roughness, and other grinding outputs.

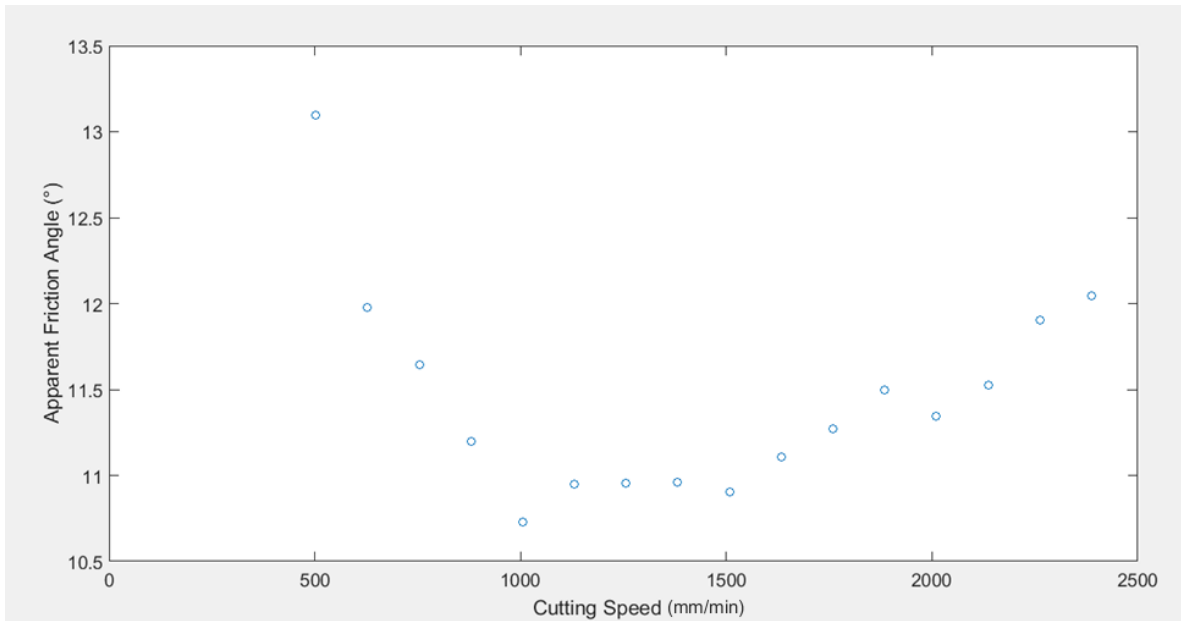


Figure 42: Sticking friction angle vs. cutting speed

Investigation of the friction in grinding is carried out with FEM models through few studies since the experimental investigating is difficult in grinding operations. The main characteristic of grinding operation is the negative shear angle, and it leads to a decrease of the sticking friction coefficient compare to conventional operations like milling and turning. The thermomechanical approach is used to determine friction coefficients in sticking zone and decrease with increasing cutting speed is observed mainly.

When the cutting speed is changed, the friction coefficient behaves as above figure. The results are quite similar to the literature values [97].

5.1.3 Shear angle rake angle predictions

As discussed in Force chapter, the shear angle estimated based on the minimum energy principle, which relies on the crystal bond fraction taking the least challenging path on the material structure. The total cutting energy on chip formation is calculated for each shear angle values, and the minimum power requirements for cutting is selected as shear angle. In the investigation of grinding mechanics the negative rake angle, which is formed by random structured abrasive particle shapes, is the most influence factor in determining the shear angle. In this study shear angle is investigated with the average grit rake angle measurement and applied to the all active grits in cutting zone.

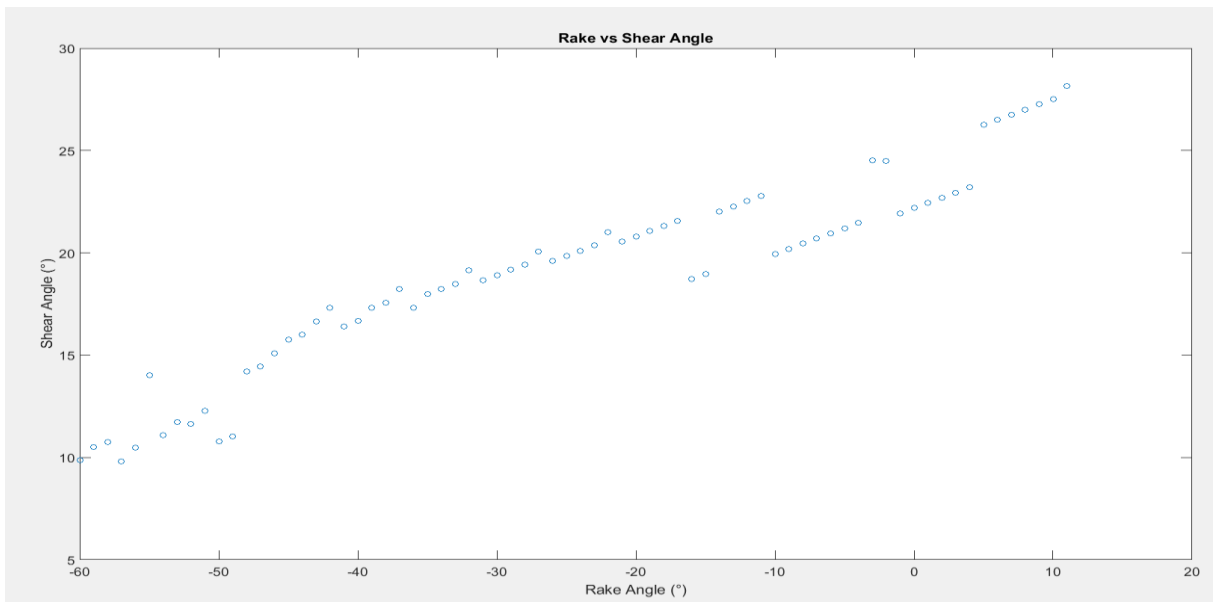


Figure 43: Shear angle vs. rake angle

When the shear angle investigations are done with the corresponding negative rake angle values, the results are in nonlinear behavior since the solution of the thermomechanical model is nonlinear. On the other hand, calculated shear angle is proportional to the rake angle in the general correlation of the data. Shear angle behavior was consistent with the FEM results in the literature [71].

5.1.4 Temperature effect on shear zone

The thermal stress causes to increasing the strain values for ultimate tensile strength of the material which is resulted with decreasing ultimate tensile strength. When temperature induced to the material it becomes more creep and stress requirement for plastic deformation of material becomes lower. Concordantly, the main output of the thermomechanical model is the grinding forces, the initial temperature parameter for Johnson-Cook material model is also crucial to predicting forces in accuracy. The temperature in the grinding zone is much larger and in wider range compare to conventional operations. In order to investigate the temperature effects on the forces following simulation results are obtained within different process temperature values from 50 to 850 Celsius degree.

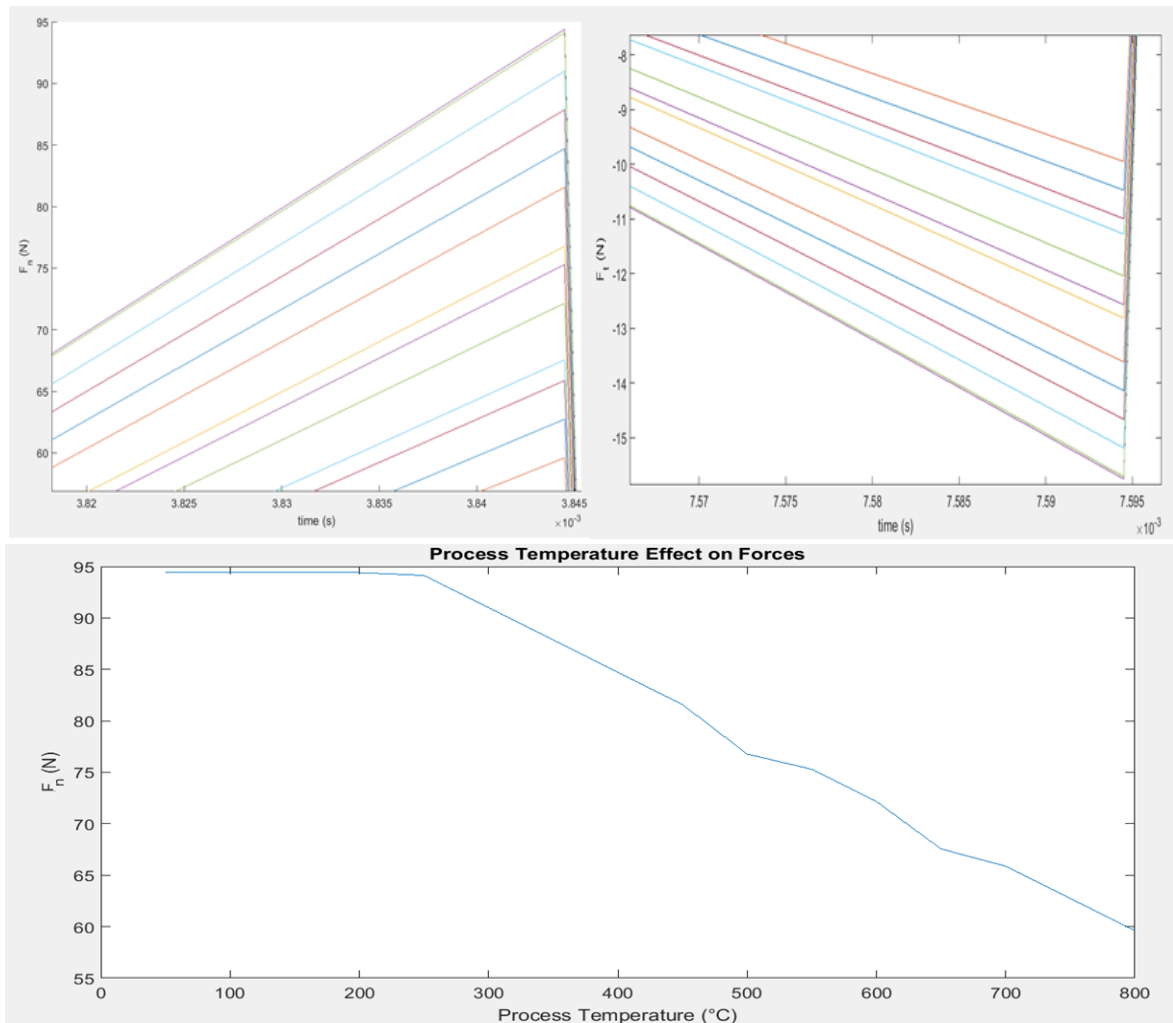


Figure 44: Effect of initial temperature on forces for thermomechanical model

As seen on the above Figure 44, the results are changed drastically depend on process temperature. The following procedure is created to predict initial process temperature better. Thermomechanical force model is solved with different temperature values, and the obtained forces are converted into heat flow with using heat partitioning and heat flux model. Resultant heat flux is moved on the workpiece with corresponding values, and the maximum temperature is calculated via temperature distribution model which is the closest point to the grinding zone in the middle. The calculated and attained temperature values are compared until the error between them lower than 10%. The following detailed results are obtained with the given grinding conditions, and the procedure is applied to the other investigations.

Simulation No	T_attained (°C)	Force_N (N)	Force_T (N)	Q(Calculated) (W/m ²)	T_max (Calculated) (°C)
1	50	94,401	15,759	8,4567E+07	939,75
2	100	94,401	15,759	8,4567E+07	939,75
3	150	94,401	15,759	8,4567E+07	939,75
4	200	94,401	15,759	8,4567E+07	939,75
5	250	94,134	15,7150	8,4328E+07	937
6	300	90,998	15,1916	8,1519E+07	906
7	350	87,863	14,668	7,8710E+07	876
8	400	84,714	14,142	7,5889E+07	845
9	450	81,578	13,619	7,3080E+07	815
10	500	76,775	12,817	6,8777E+07	769
11	550	75,294	12,569	6,7451E+07	754
12	600	72,159	12,046	6,4642E+07	724
13	650	67,558	11,277	6,0520E+07	679
14	700	65,874	10,997	5,9012E+07	663
15	750	62,739	10,473	5,6203E+07	632
16	800	59,603	9,950	5,3394E+07	602
17	850	56,468	9,426	5,0585E+07	572

Table 6: Iteration data for initial temperature prediction

The calculations of the iterative loop values are given in Table 6. The results show that the force requirement to deform material is inversely proportional to temperature. The following graphs corroborate the results of error investigation and selected iteration simulation number is 13 with calculated 679 °C temperature value and 67,56 N normal and 11,3 N tangential forces. Experimental validation is for this iteration is quite similar to the simulation results

with obtained 66 N normal force, 19 N tangential force and 720 °C maximum temperature value.

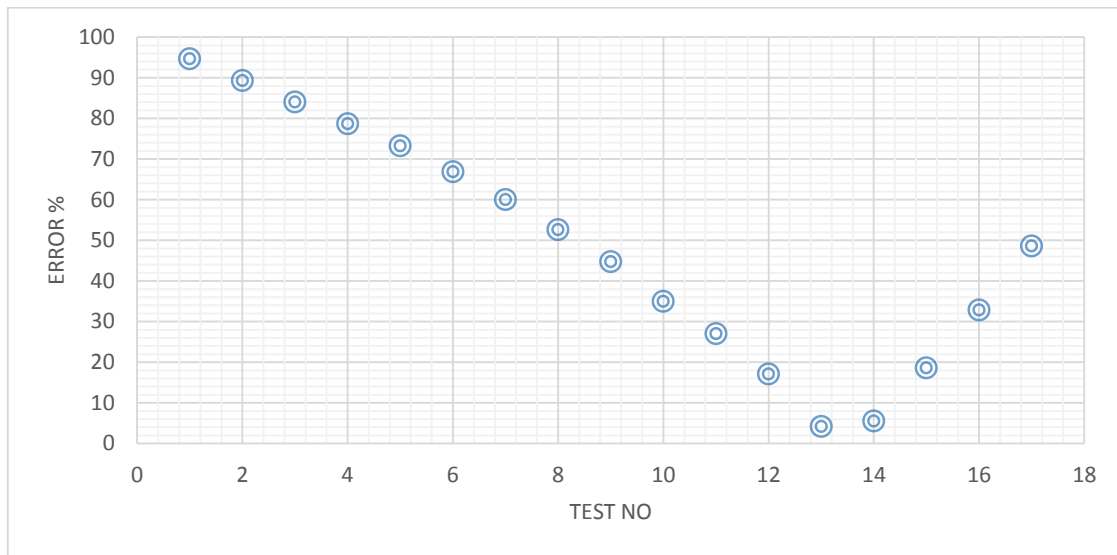


Figure 45: The error ratio for attained and calculated temperature values

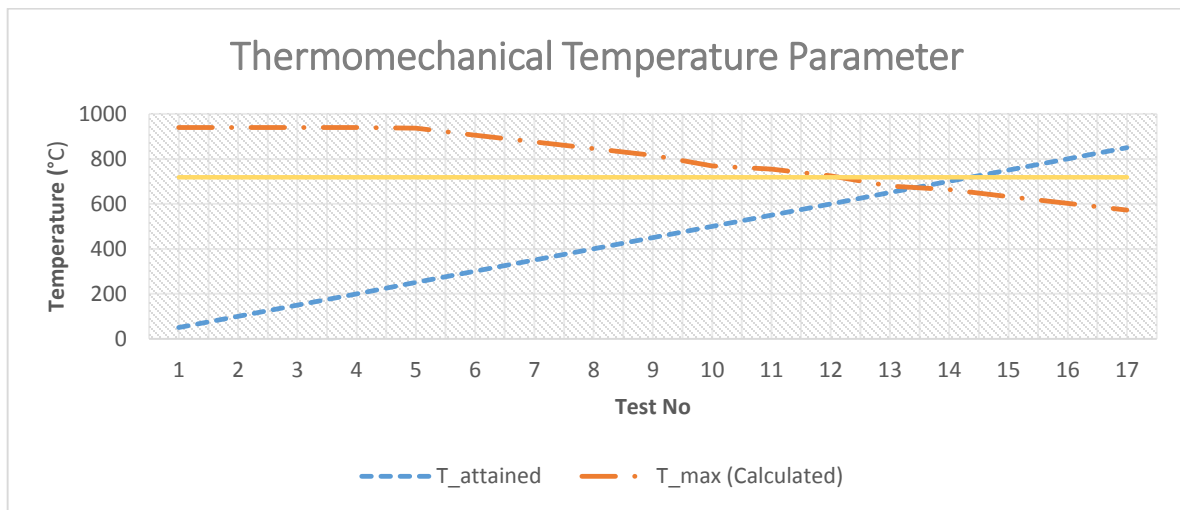


Figure 46: Temperature calculation and estimation graph

The differences between calculated maximum temperature and measured temperature values are due to unavoidable noise on measurements and the model assumptions reasonably differ from real life mechanisms.

5.1.5 Temperature full solution in 3D

The predictions of temperature distribution are necessary to foresee the residual stress and detect burn on the surface which is the chemical reaction triggered by the heat. In this study investigation of the temperature distribution is made on adiabatic condition without phase transformation of the microstructure of the workpiece material.

Below Figure 47 exemplify the three different x positions of the thermocouple on the workpiece, and corresponding temperature distribution solutions were evaluated. The Inconel workpiece with the 50x10x100 mm was established for this simulation. Temperature rise profile is obtained with rising maximum temperature since adiabatic assumption leads to increasing heat energy in the workpiece and the reality just slightly differs in the form of the convective cooling part.

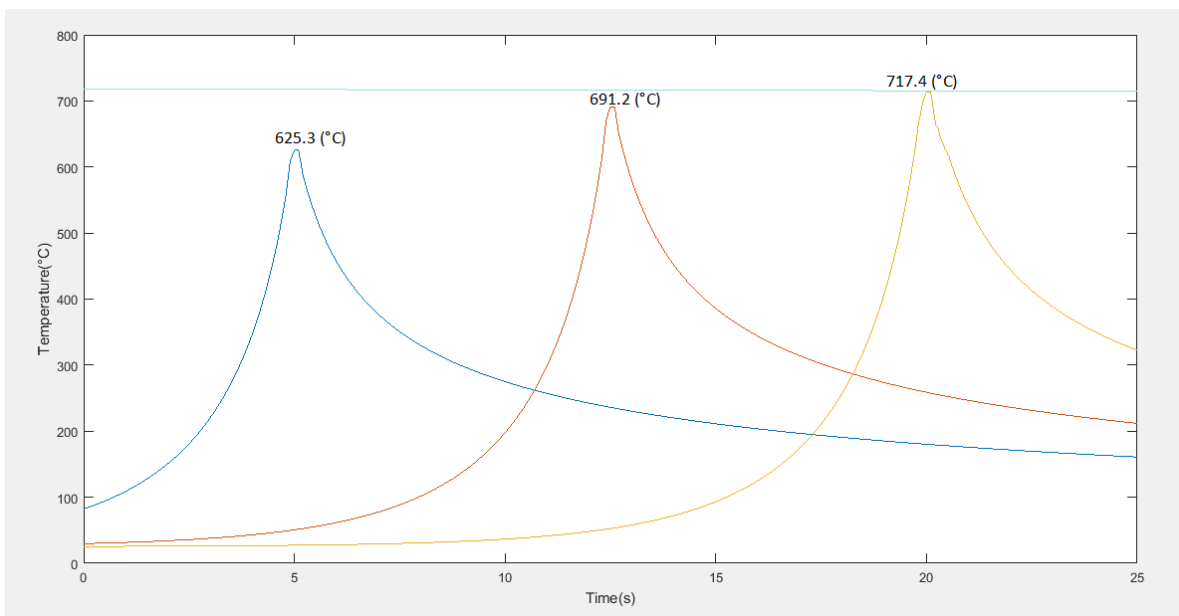


Figure 47: Simulated temperature for different x position

The second investigation has been constructed with various depths of thermocouple beneath at the middle of the workpiece. Significant differences between temperature profiles on various depths were observed as expected since the heat energy can travel faster to bodies with low energy according to laws of thermodynamics. Following investigation has been done from 0-micron depths to 500-micron depth.

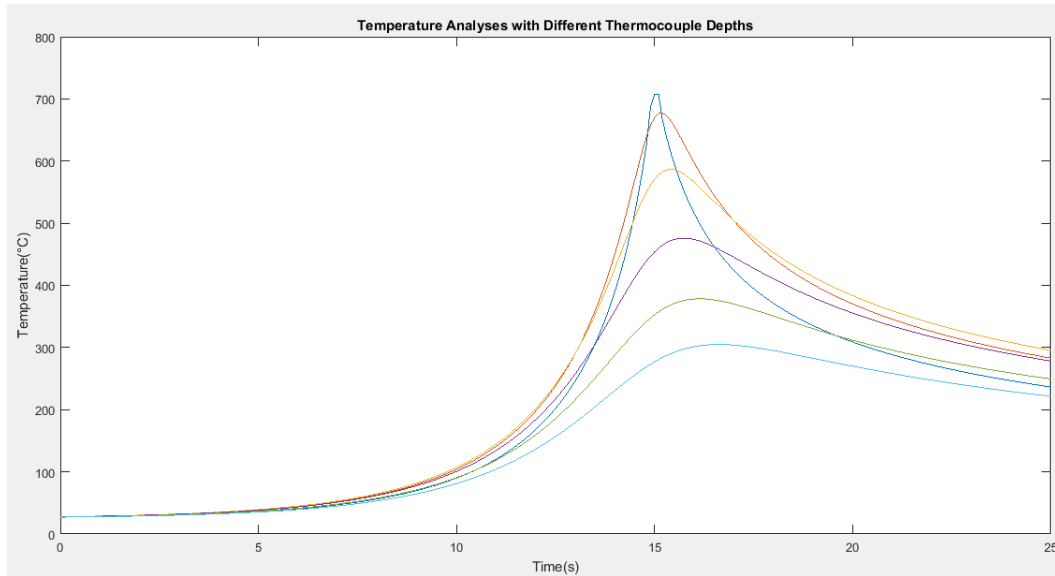


Figure 48: Simulated temperature for different depth beneath the surface

The established full temperature distribution solution in 3D is represented in Figure 49 with combining above investigations.

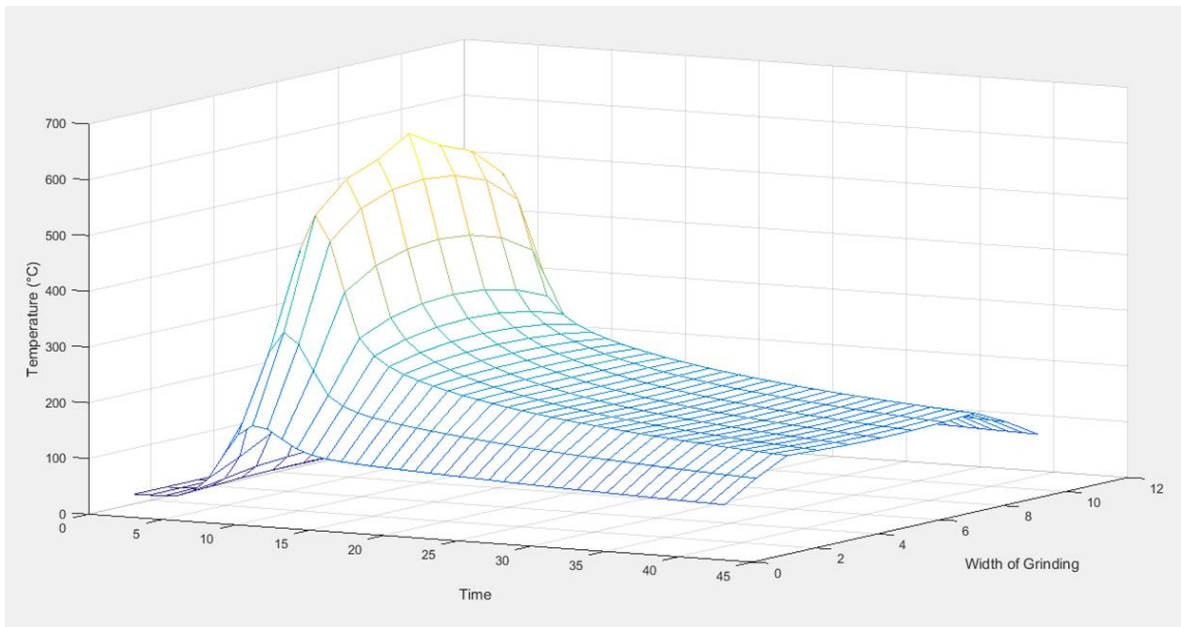


Figure 49: 3D temperature simulation of the workpiece

The geometrical uniformly distributed structure has been created in the grinding zone with respect to the measured and calibrated active cutting grains C where each of them behaves as a heat source. If this distribution is taken into consideration, it can be seen that the center point of the grinding zone is closest to the heat sources whereas edges of the grinding zone

are farthest nodes. Temperature rise profile is larger on the closer points and smaller on distant points to the heat sources. Temperature rise on the grinding zone can be seen in the yellow area, and the uncut area of the workpiece is the rest with corresponding width value. Maximum temperature out of grinding zone is radically smaller than the cutting zone at the workpiece surface.

The difference between the thermal camera and thermocouple measurements could be correlated due to this distribution effect, considering the experimental data. The maximum temperature measurements obtained by the thermal camera has been smaller than the maximum value of thermocouples, and this difference is further increased with grinding wheel width.

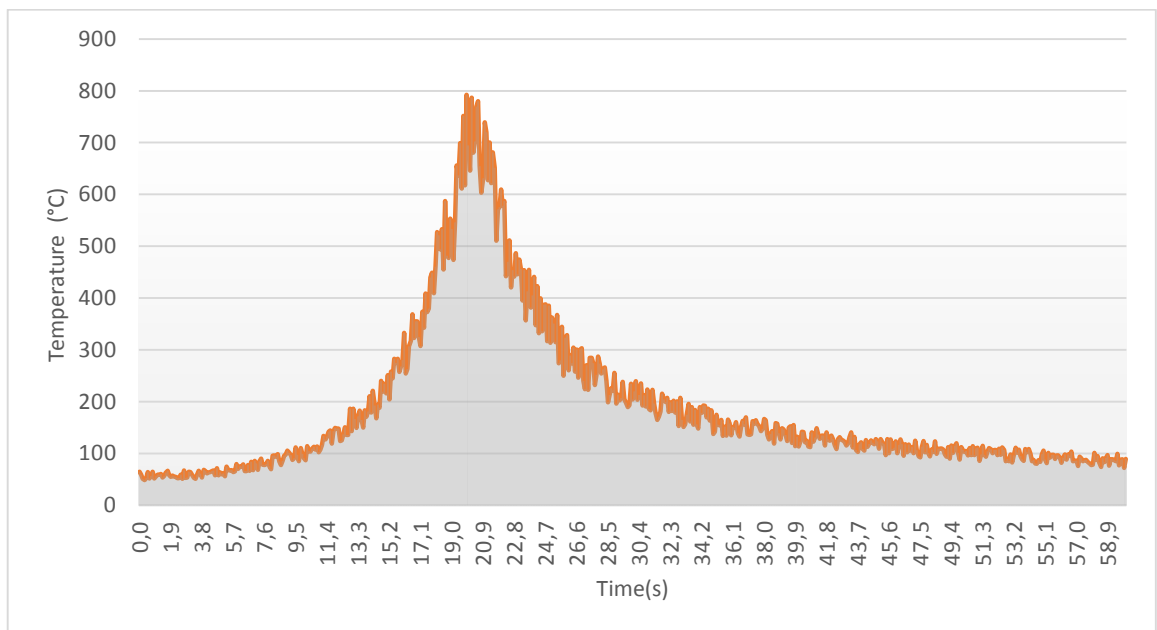


Figure 50: Filtered temperature measurement for the grinding condition

The maximum temperature value was read as 420 Celsius degree on thermal camera when the temperature profile has been observed with thermocouple via low pass filter as in Figure 50 much higher. Also, a thermal camera can be used only for dry cutting conditions since the emissivity problems. For this reason in this study, thermocouple measurements have been done in the middle of grinding zone with different depths beneath workpiece surface. According to this information, the more detailed experimental validations has been made in the next section.

5.1.6 Experimental Setups

In this section, temperature and force calculations are verified by experimental data. The correct use of equipment has great importance for verification of results. The accuracy of the measurement is quite challenging in the grinding operations compare to other machining operations regarding geometrical limitations. It results in high noise generation during measurement process which is caused by a large number of cutting grains with different characteristics. The elimination of these distortion requires appropriate sample rates and low pass filters in measurements, which is much more important in thermal measurement. There are various instruments used for gathering grinding process data. Thermocouple fixation in the workpiece and infrared usage are common methods for thermal measurements along with advantages and disadvantages. The test equipment used in this study were explained below with their properties and limitations.

5.1.6.1 CNC Grinding Machine

Process tests are conducted on the CNC controlled 3-axis surface grinding machine which is Chevalier Smart H/B 818III. The channel operation on the graphic control of the machine and programmable G-Code options have been used with different process parameters.



Figure 51: CNC grinding machine

Although the electromagnet magnetic chuck speeds up the workpiece fixing, electronic device usage on it is limited to the inconsistent data due to the magnetic effect on devices.

5.1.6.2 uSurf Nanofocus

Optical image processing device has been used to investigate the grain characteristics on the wheel, which is one of the most significant factors in process modeling. The grain analyses are conducted on a μ surf explorer nanofocus 3D optical device with a sensitivity of 100 nm in the X and Y plane. The grain analyzing methods were detailed in the grain measurements section.



Figure 52: NanoFocus surface topography measurement equipment (a) small wheel holder (b) large wheel holder

In order to remove possible height disorientation from the position of the wheel, measuring devices were produced in specific dimensions for the corresponding tools as shown in Figure 52. Nonetheless, the deviations that can be caused by angular disorientation were corrected with the help of measurement program in the device.

5.1.6.3 Workpiece

The workpiece was designed as CAD using Solidworks program. The thermocouple holes are designed at different depths beneath the surface as blind holes to observe temperature distribution on the workpiece with coordination effects as illustrated in Figure 53.

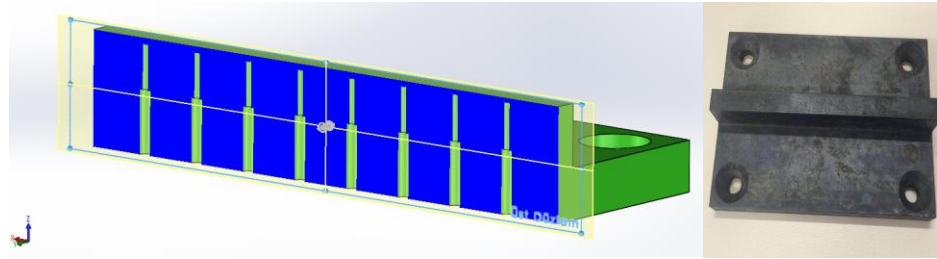


Figure 53: Workpiece design (a) section view for thermocouple holes (b) produced workpiece

The workpiece is composed of two parts, in which the grinding process performed on the narrow green one with thermocouple fixation method. The workpiece assembly with grinding tool and dynamometer shown in Figure 54.

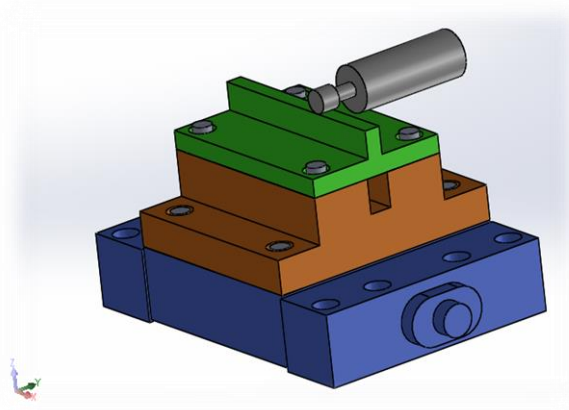


Figure 54: Assembly of the workpiece on dynamometer

In this design, the lower part was produced by hardened aluminum to minimize the magnetic effects from the magnetic chuck. The workpiece AISI1050 is also hardened for CBN wheel usage.

5.1.6.4 Thermocouples

Thermocouples are manufactured with two different materials which are formed as a head at the tip of the cable by the special joining process. When two different conductors are exposed to a temperature gradient, thermoelectric voltage is produced on them which is at the micro voltage level for each degree and should be converted into temperature data via thermal data acquisition device. In this study, thermocouples were selected to provide two conditions; which are thermocouple dimensions must be as small as possible for minor influence on workpiece material characteristic, and the second one is high-temperature measurement range to observe elevated temperature in grinding processes. Although, the measurement sensitivity decreases when the measurement range increase, K-type sensors were selected with 5 Celsius degree error since it is acceptable for high-temperature measurements of grinding. The selected thermocouples have measurement range between -200 and 1250 Celsius degree with a 0.81 mm diameter.



Figure 55: Thermocouple fixation with syringe

Thermocouple fixation has been done with the high-temperature resistant epoxy mixture into the thermocouple channels with a syringe as shown in Figure 55. Fixed thermocouples were tested with a heat gun before grinding operation to minimize distortion on data.

5.1.6.5 Thermal Camera

In this study, FLIR brand industrial thermal camera was used with the 10X lens to observe dry grinding zone temperature with a better focal point. Thermal energy emitted from the objects above -273 Celcius degree and thermal camera capture this energy in the form of infrared waves and process it into temperature values with the corresponding emissivity of

the object. The emissivity values were verified and calibrated via thermocouple measurement to correlate obtained temperature values.



Figure 56: Thermal camera -FLIR

The calibrated emissivity only belongs to workpiece material and if any medium distorts this reflection image the results are unusable. In this manner, the cooling liquid cannot be used for thermal camera measurements. Moreover, maximum temperature occurs in the middle of the workpiece in the thin band could not be detected with a thermal camera.

5.1.6.6 Temperature Data Acquisition Device

Simultaneous temperature measurement from multiple thermocouples required for temperature distribution along workpiece data. In the literature, the temperature measurements usually limited to one point measurements. Although the standard temperature analyzing devices offers multiple thermocouple measurements, the sampling rate drops drastically as one over a second. For this reason, DT9805 Data Translation module was used to obtain process temperature of grinding with a sampling rate of 6250 Hz.



Figure 57: Thermal data acquisition system (a) Device Configuration (b) Device

In this manner, user interface QuickDAQ program was used to calibrate thermocouples within a type of thermocouple and voltage range, and to filter the noise via a low-pass filter. Device and setup are shown in Figure 57.

5.1.6.7 Dynamometer

Force measurements were done with Kistler 9192AA model table type 3-axis dynamometer as shown in Figure 58.

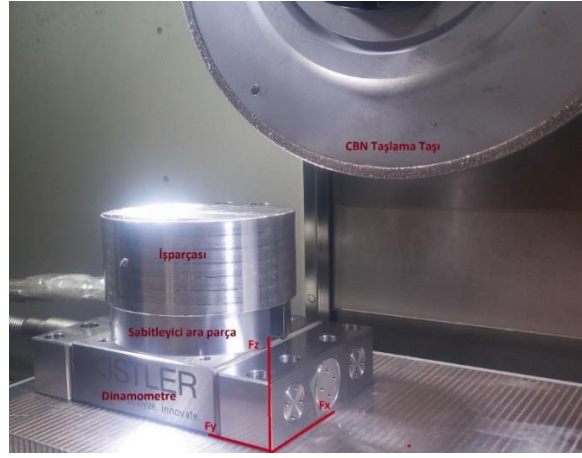


Figure 58: Dynamometer

A model with external signal amplifier was chosen since the magnetic chuck limitations. The voltage values obtained from the piezo sensors were processed to the computer as force via National Instrument data acquisition module through calibrated charge amplifier. Labview program was written to analyze these data.

5.1.7 Grain Measurements & Grinding Wheels Parameters

Determining the cutting grains geometrical properties in grinding plays a critical role in process modeling. Although tool geometry can be precisely determined in milling and turning operations, cutting grains geometry are unpredictable compared to other cutting tools. After determination of the grain geometry, grinding force and temperature of the process could be modeled analytically as mentioned previous chapters. However, the fact that the abrasive particles on grinding wheels are located with random density and shape results in each grinding tool has its cutting tool parameters. On the other hand, Jiang's study showed that cutting abrasive geometry stay in certain range on the wheel type and grain material properties [98]. In this manner, the geometric data obtained for wheels could be used for the same type of grinding wheels also. In this study, CBN and conventional wheels were investigated for the geometrical definition of grinding process models.

5.1.7.1 Grain Parameters Definition Methods

The geometry of the grains was determined by rake angle, oblique angle, height and width of grits, and edge radius parameters. Grit analyses were performed on a different area of the wheel with the help of produced wheel holder devices. Single grit analysis has been done with 50x lens on the NanoFocus device within 0.64 millimeter square for each investigation. After the useable area was defined, highest grit has been examined to obtain data set. This process was repeated for at least 50 particles per grinding wheel to acquire distribution and a characteristic of them. The mean and standard deviation values for grit geometric properties were obtained for each wheel, and these values were used as the cutting tool geometry in the process models.

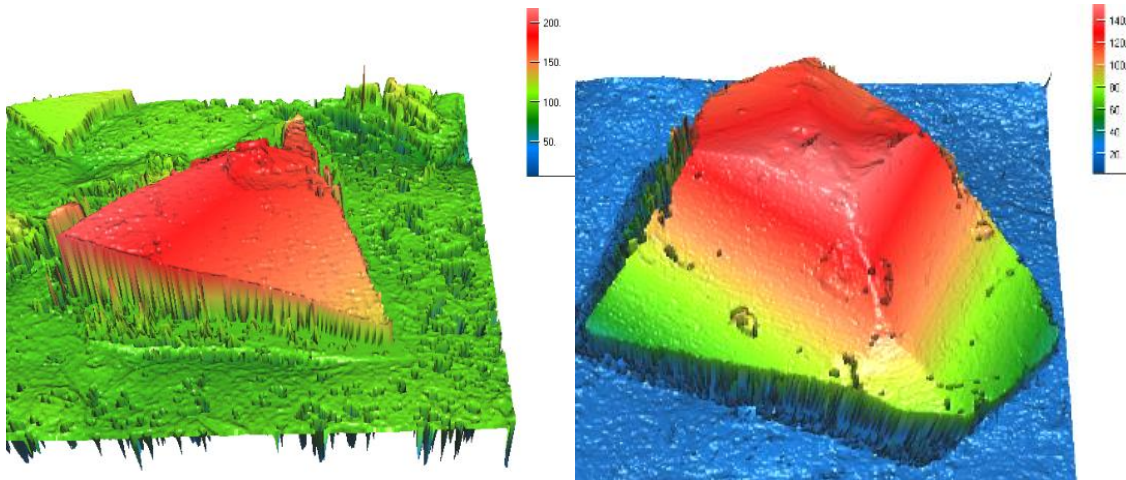


Figure 59: 3D scanned grain images

The topography of the detected abrasive grain was obtained in three-dimensional image as illustrated in Figure 59. Measurement tools on the NanoFocus as a point to point distance and angle measurements were conducted with following steps. The exaggerated illustrations of the single abrasive grains can be seen as oriented into grinding operation in Figure 60.

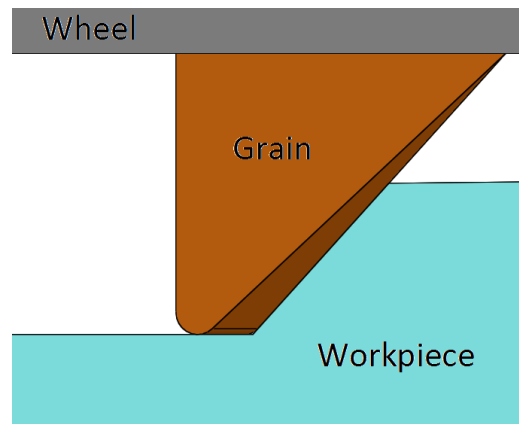


Figure 60: Exaggerated image of grain on cutting

The demonstrated cutting abrasive grain topography has been acquired from the top view as shown in Figure 61a.

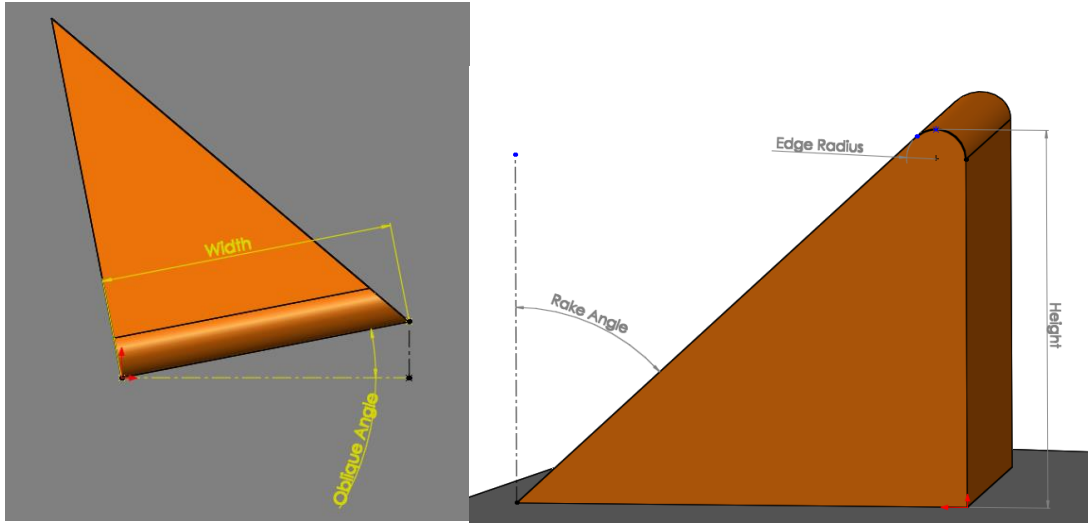


Figure 61: Illustrated grain geometry (a) width and oblique angle (b) height, rake angle and edge radius

The measurements were made on a rigid coordination system which depends on the direction of the workpiece movement to the grain. First of all, the oblique angle has been attained as illustrated in the above Figure 61a. After that calculation, grit was normalized in this direction, and other parameters were calculated as illustrated on the Figure 61b.

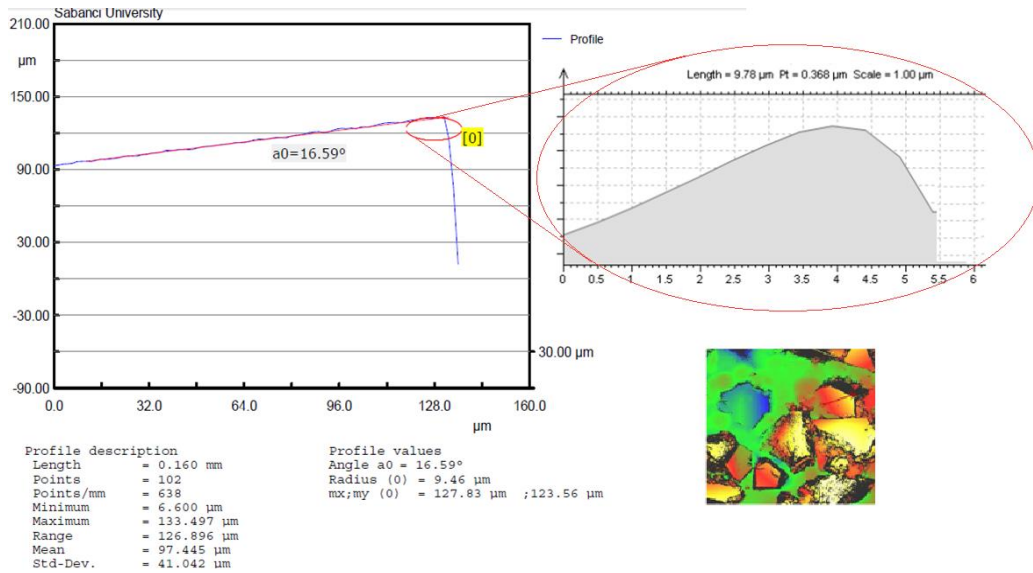


Figure 62: Sample program interface and analysis display

The usage of described analyzing methods for raw data on the program shown in Figure 62. Moreover, edge radius analysis has been performed on another module of the NanoFocus which can be seen with zoomed area in Figure 62.

The geometric features obtained from the measurements were stored and analyzed on the histogram with average and standard deviation values. As an example, the rake angle analysis, which is based on 200-grain measurements in this one, illustrated as follows;

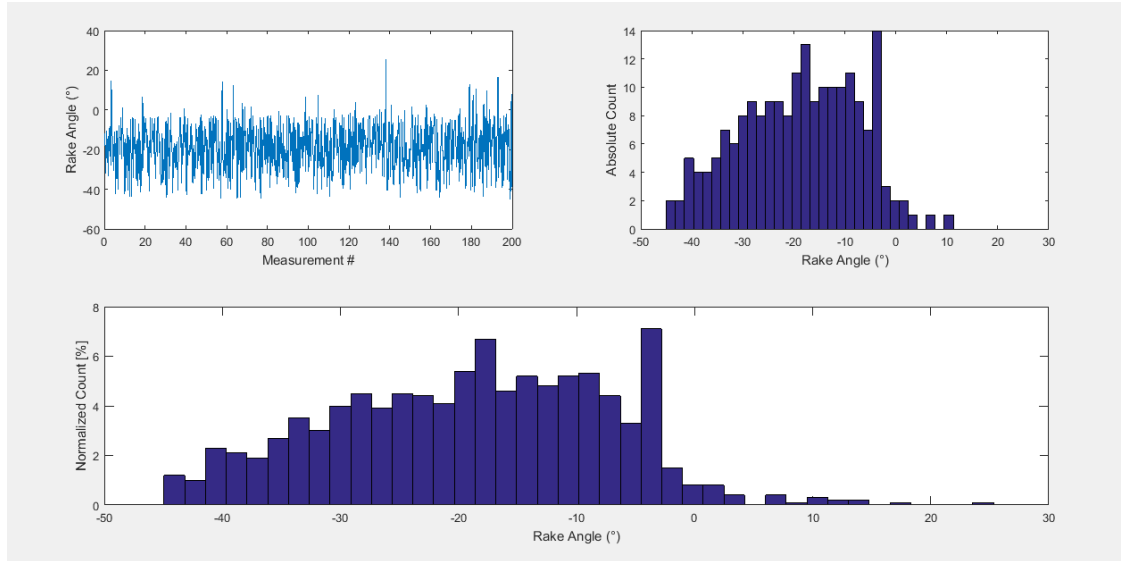


Figure 63: Rake angle investigation on histogram

Rake angle parameter is crucial for process modeling as mentioned on the force chapter. In this context, the grinding wheel has been examined horizontally with produced device to observe grains with positive rake angle. However, results showed that grains with negative rake angle were dominant as seen in Figure 63.

Active cutting grains in millimeter square is defined as C coefficient. In this study, the method of determining the coefficient C was based on the topographical count of the grains which are above the measured average height of the grains. The lowest Z location of the measurement was taken as average grain height from the bottom of the wheel and appearing grains were counted manually as active cutting grits. The 20x lens was used severally to scan a larger area, and observed values are combined and calibrated into C coefficient. However, the number of grains in contact with the workpiece are proportional to the depth of cut and other process parameters also. Despite this effect, rough assumptions and measurements for active grains per unit area resulted in consistent data in range.

5.1.7.2 Wheels Characteristics

In this study CBN, aluminum oxide and silicon carbide grinding tools were used to examine the process variables for conventional and super abrasive particles. Mechanical and thermal properties of the general grain materials are given in Table 7.

Properties	Units	Aluminum Oxide	Silicon Carbide	C-Boron Nitride	Diamond
Density	g/cm ³	3,96	3,15	3,48	3,52
Hardness	HRc	115,00	167,00	362,00	562,00
Young Modulus	GPA	400	396	682	890
Friction co-efficient	-	0,34	0,23	0,19	0,05
Poisson ratio	-	0,20	0,17	0,17	0,0002
Melting point	°C	2050	2730	2973	3700
Specific heat capacity	J/(kgK)	712	628	506	507
Thermal conductivity	w/(mK)	17	92	481	900
Thermal diffusivity	m ² /s	6,17×10 ⁻⁶	45,8×10 ⁻⁶	273×10 ⁻⁶	504×10 ⁻⁶

Table 7: Mechanical and thermal properties of typical grain materials

Active cutting grain and dimensional investigations of conventional wheels are given in Table 8 with the corresponding image of grinding wheels.



Figure 64: Conventional wheels 01,02,03

Grinding Wheel Code	C Coefficient	L-spacing - mm	Grain Density	Dimensions - mm	Material
CONV01	1,49	0,46	4,73	220x20	Al ₂ O ₃
CONV02	1,08	0,55	3,34	150x20	EKR-Al ₂ O ₃
CONV03	0,61	0,70	2,05	150x20	NK-SiC

Table 8: Geometrical properties of conventional wheels

The median value and standard deviation of each geometric parameter are obtained for each wheel as in Table 9.

Grinding Wheel Code	Height (Average/STD) - μm	Width (Average/STD) - μm	Rake Angle (Average/STD) - Degree	Oblique Angle (Average/STD) - Degree	Edge Radius - μm
CONV01	175,13/83,88	359,33/100,86	(-)16,56/3,8	15,72/4,69	11,7
CONV02	307,61/53,69	415,33/127,89	(-)25,41/4,68	16,1/5,96	17,2
CONV03	284,61/88,72	582,33/149,94	(-)26,3/9,88	23,44/8,59	8,3

Table 9: Geometrical properties of grains on conventional wheels

The same procedure was applied to CBN wheels. Active cutting grain and dimensional investigations of CBN wheels are given in Table 10 with the corresponding image of grinding wheels.

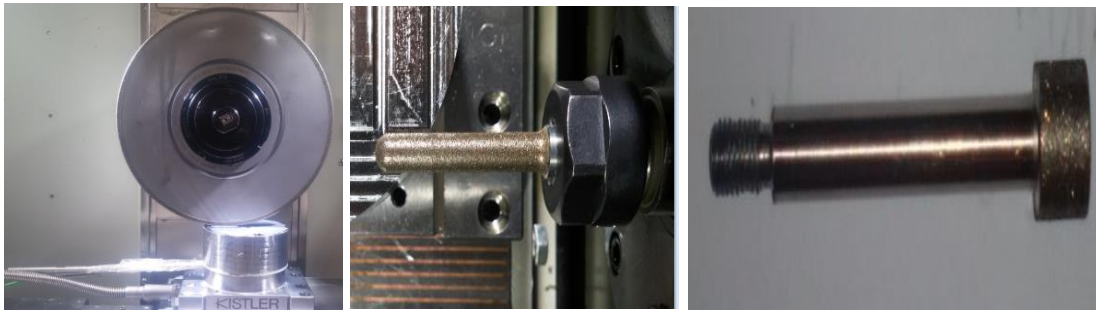


Figure 65: CBN wheels 01,02,03

Grinding Wheel Code	C Coefficient	L-spacing - mm	Grain Density	Dimensions - mm	Material
CBN01	3,2	0,30	10,80	254x7,58	C- Boron Nitride
CBN02	7,8	0,31	23,52	7,16x41	C- Boron Nitride
CBN03	6,1	0,27	14,15	20x8	C- Boron Nitride

Table 10: Geometrical properties of CBN wheels

The median value and standard deviation of each geometric parameter are obtained for each wheel as in Table 11.

Grinding Wheel Code	Height (Average/STD) - μm	Width (Average/STD) - μm	Rake Angle (Average/STD) - Degree	Oblique Angle (Average/STD) - Degree	Edge Radius - μm
CBN01	111,63/27,2	245,7/38,4	(-)28,45/11,2	23,61/14,8	0,18
CBN02	142,12/20,1	73,32/11,3	(-)44,92/4,98	31,8/16,2	0,06
CBN03	47,71/7,8	139,04/32,3	(-)26,2/7,5	24,25/3	0,13

Table 11: Geometrical properties of grains on CBN wheels

According to topography analysis, the CBN tools have a much sharper cutting edge which facilitates easier deformation of the material with lower energy, although process force is also proportional to the number of active grain number. For these reasons, super alloy grinding is much more suitable with CBN wheels.

5.2 Experimental Force Verification

In this study, the process forces were measured with higher than 200 Hz sample rate. It is impossible to measure the force behavior per tool by assigning a sample rate according to the tool geometry and cutting parameters. However, nature of grinding operations makes it impossible to observe single force behavior if it is not a single grain tool. The general behavior of the grinding force was illustrated in Figure 66 by the representative measured raw force data. Normal and tangential forces for each experiment were analyzed with a corresponding maximum value of force.

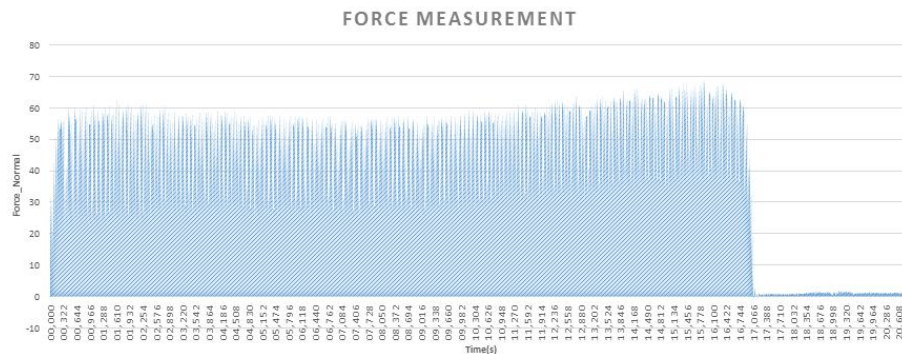


Figure 66: Sample force measurement

In the oblique thermomechanical model, the shear angle was estimated for single grain which was constructed with average geometrical values of the grains. Thermomechanical edge force analysis model was used to calculate force per grain with the shear angle in a geometrical range of grains, and acquired force is multiplied by the number of active cutting grains in grinding zone to obtain process forces.

The conventional grinding test is conducted on the AISI1050 steel with the dry condition and corresponding wheels. Different conventional wheels were investigated and compared with thermomechanical force model with the following

representation;



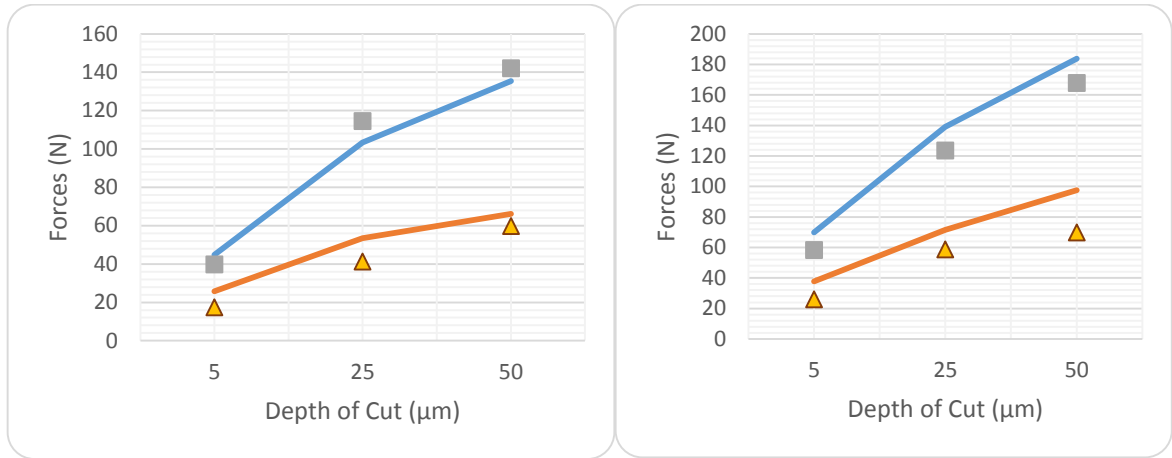


Figure 67: The comparison of grinding forces with CONV01 with wheel speed 23,04 m/s and workpiece velocity (a) 0,0083 m/s (b) 0,0166 m/s

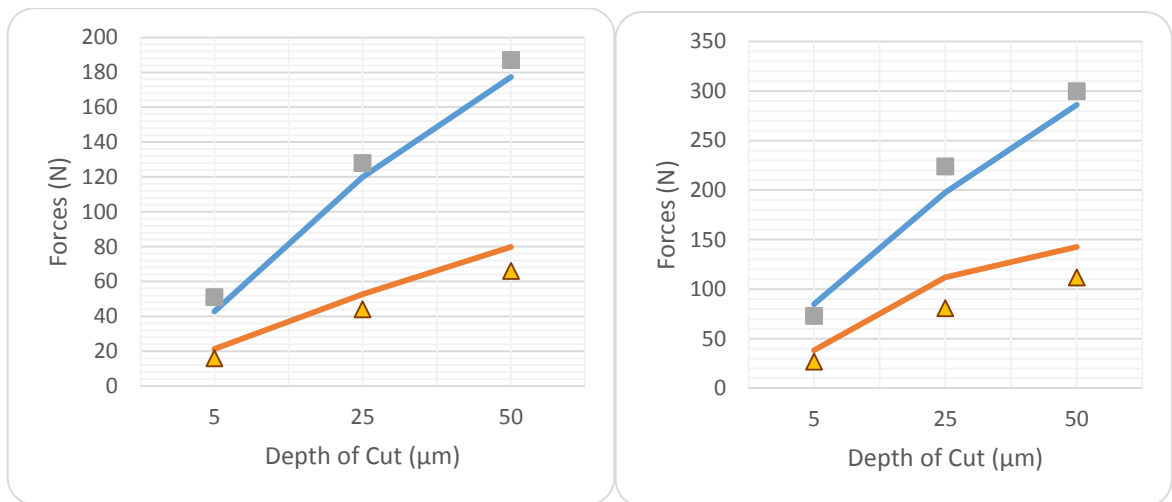


Figure 68: The comparison of grinding forces with CONV02 with wheel speed 15,7 m/s and workpiece velocity (a) 0,0083 m/s (b) 0,0166 m/s

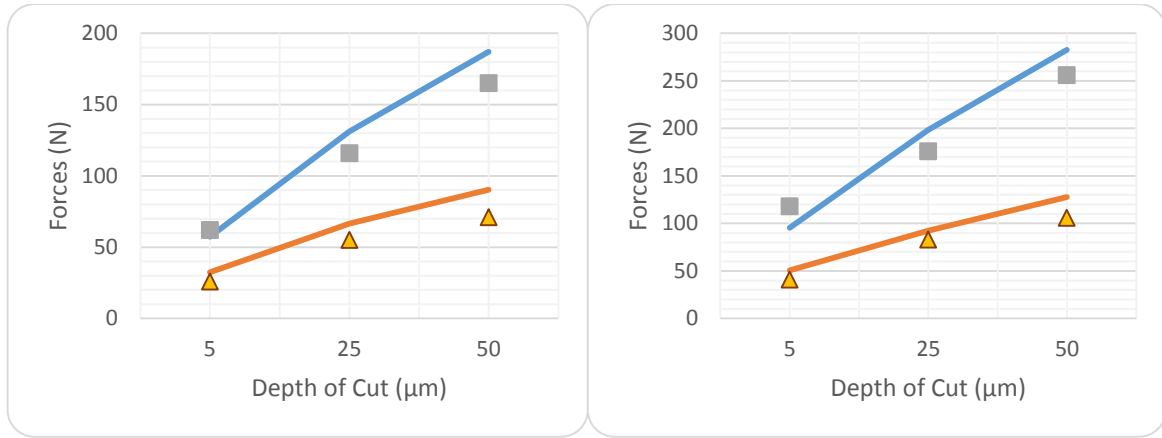


Figure 69: The comparison of grinding forces with CONV03 with wheel speed 15,7 m/s and workpiece velocity (a) 0,0083 m/s (b) 0,0166 m/s

It can be concluded that the thermomechanical force model gives consistent results with experimental data along with iterative temperature prediction module. Another result from these graphs is that tangential force predictions are worse than normal force estimations since the random oblique angles were not considered for each grain on the model. Error increased for force predictions when the feed was higher. On the other hand, process parameters along with wheel grain characteristics effects are in generally good agreement with experimental data.

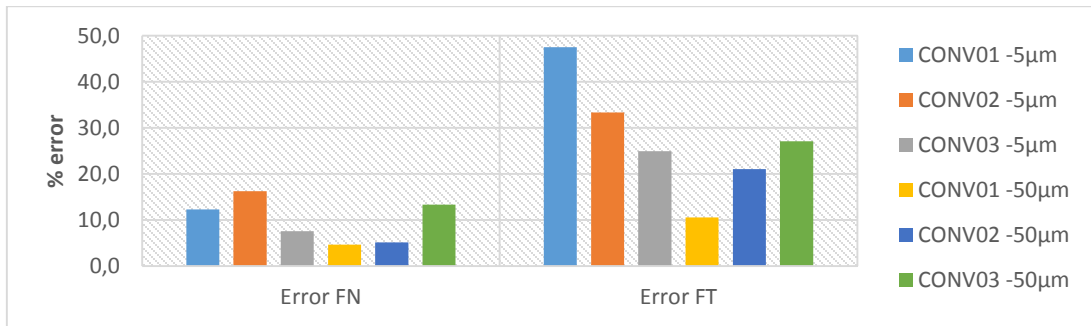


Figure 70: Error comparison of different wheels' forces with 0,083 mm/s feed and different depth of cut

The error between prediction and experiments are getting lower with increasing depth of cut; it can be deduced that the number of active cutting grain prediction cannot be constant. As the depth of cut decreases, the number of active cutting grains also decreases. Moreover, third deformation zone effect could be more influential compared to the higher depth of cuts.

In CBN grinding operations three different wheels used on Inconel718 and AISI1050 steel with the dry condition, and the results are given below.

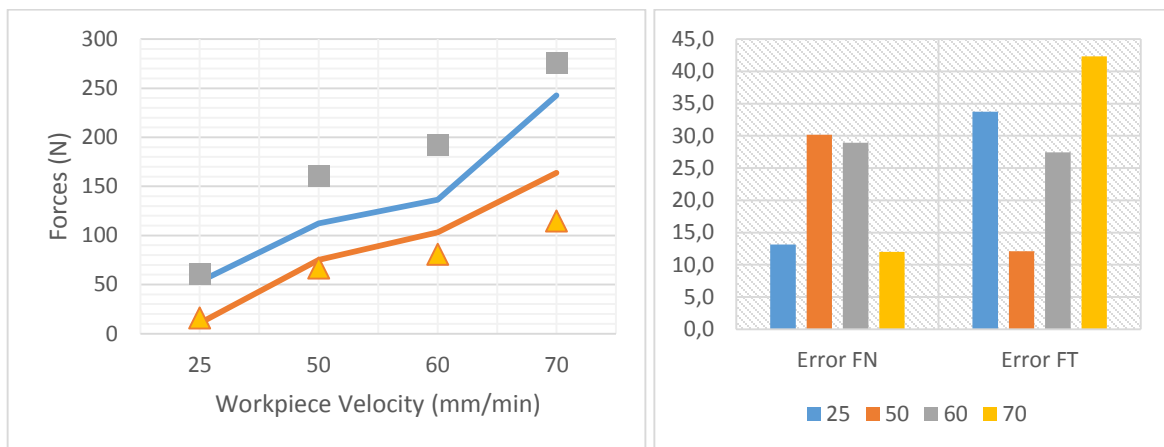


Figure 71: The comparison of grinding forces with CBN01 with wheel speed 53,19 m/s and depth of cut 100 μm on Inconel718 (a) Forces at different workpiece velocity (b) Error comparison

In the first data set of CBN grinding high wheel speed was investigated for feed parameter as Figure 71. The obvious result is forces are increasing with feed. Moreover, tangential force predictions are way worse than normal force prediction and the error for it increasing with feed. It could be because of the sharp edge of CBN grains which could lower the forces than expected.

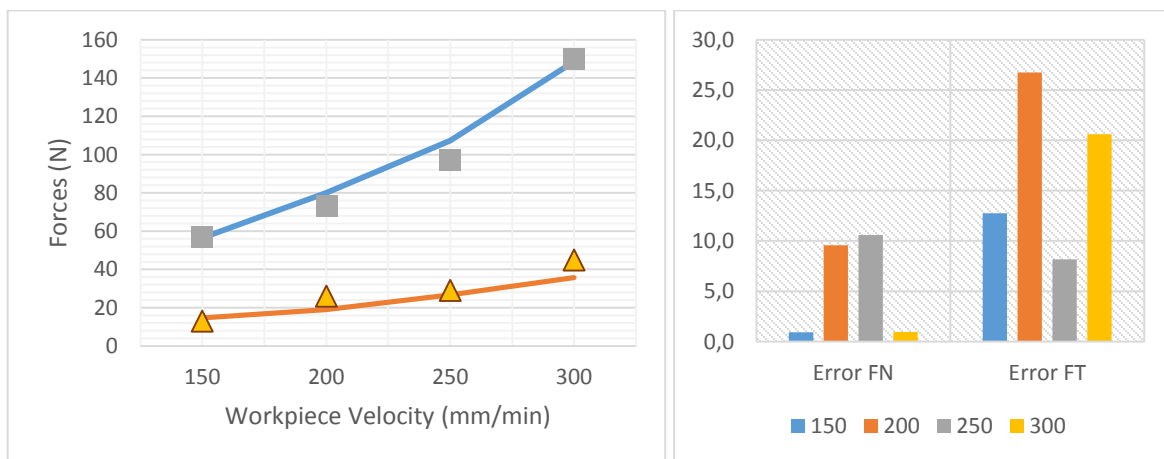


Figure 72: The comparison of grinding forces with CBN02 with wheel speed 13,49 m/s and depth of cut 100 μm on Inconel718 (a) Forces at different workpiece velocity (b) Error comparison

In the second investigation, CBN02 wheel was used with relatively lower wheel speed, and the results were more consistent compared to higher wheel speed. Nonetheless, increasing error behavior with feed is still remained. This error behavior confirms that the first deformation zone with negative rake angle could have another cutting mechanism in it, but the results are quite compatible at this level.

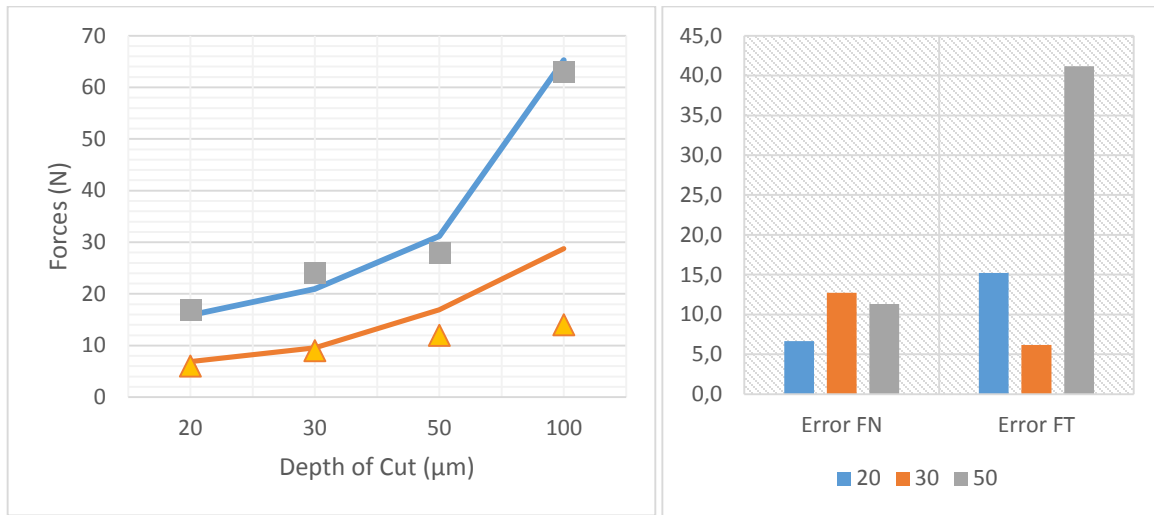


Figure 73: The comparison of grinding forces with CBN03 with wheel speed 15,08 m/s and feed 150 mm/min on AISI1050 Steel (a) Forces at different depth of cut (b) Error comparison

In the last investigation, CBN03 wheel was used to grind AISI1050 steel with different depth of cut and constant workpiece speed. When the cutting depth was increased, a drastic change has occurred in the tangential prediction, but the normal force predictions were still valid.

The agreement between the experimental data and model calculations are found to be good in the normal direction. Overall comparison of the error between normal forces and experiments shown in Figure 74.

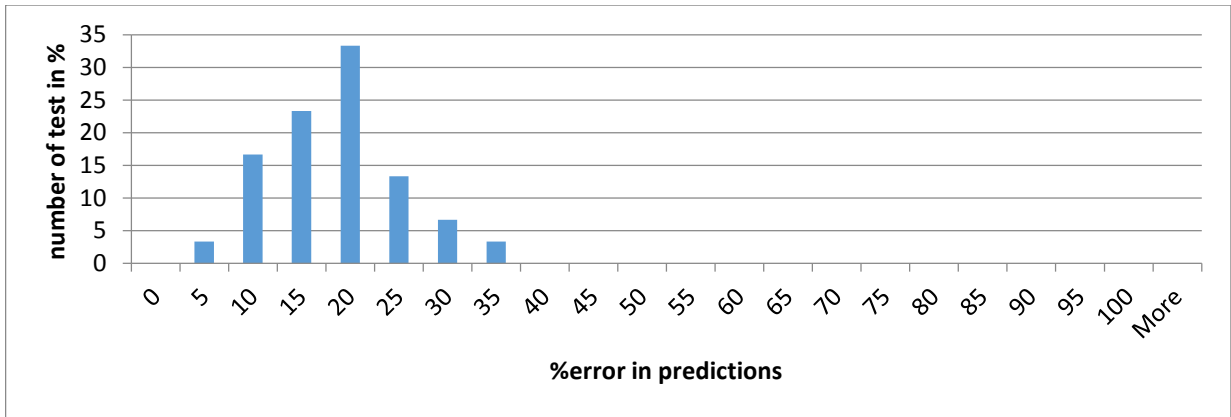


Figure 74: Error histogram between proposed model and experiments in normal forces

Overall comparison of the error between normal forces and experiments shown in Figure 75.

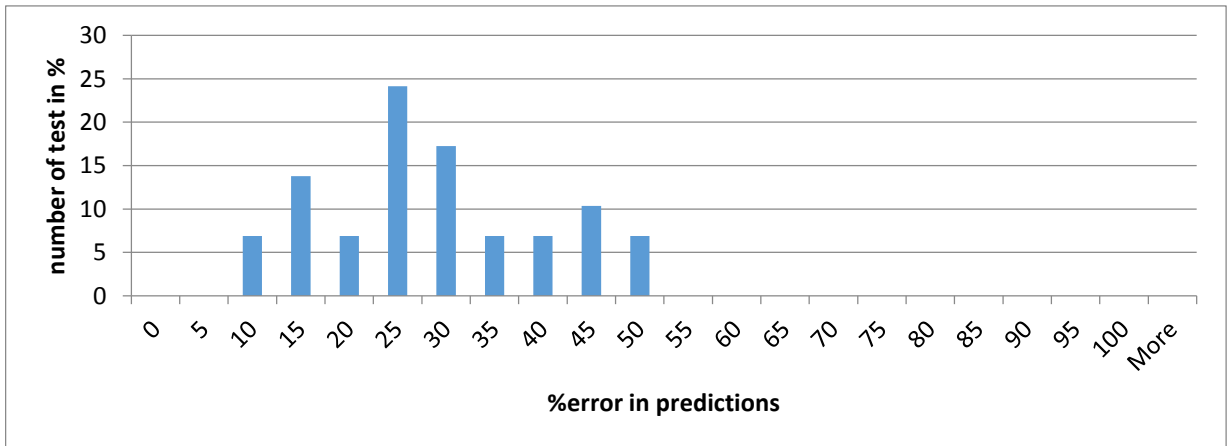


Figure 75: Error histogram between proposed model and experiments in tangential forces

In the evaluation of thermomechanical force model for grinding, high cutting speed increases the error rate. In this manner, it can be deduced that sliding friction coefficients should be calibrated and investigated in more detail for better predictions. Another result of this investigation is; there could be another cutting mechanism with negative rake angle. The last deduction for investigation is active cutting grains, and geometrical approach should be improved for better predictions. Despite all, the established model gives consistent results within a certain range.

5.2.1 Experimental Temperature Verification

Several temperature measurement experiments were conducted to verify the thermomechanical model and temperature distribution model. Up and dry grinding operations were held for this measurement. Firstly conventional wheels were used for experiments along with a thermal camera and dynamometer. The thermal camera calibration was performed by calibrating the emissivity value of the material via matching between the thermocouple on the heated object and thermal camera temperature values as illustrated in Figure 76.

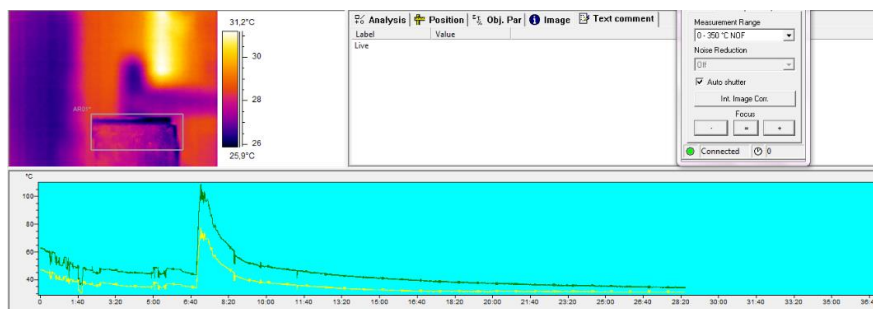


Figure 76: Thermal camera calibration

Simultaneously force and temperature measurements data were gathered, temperature results were below expectations. As it was discussed in the previous chapter, temperature measurements should be done in the middle of the workpiece with a thermocouple for accurate, reliable data.

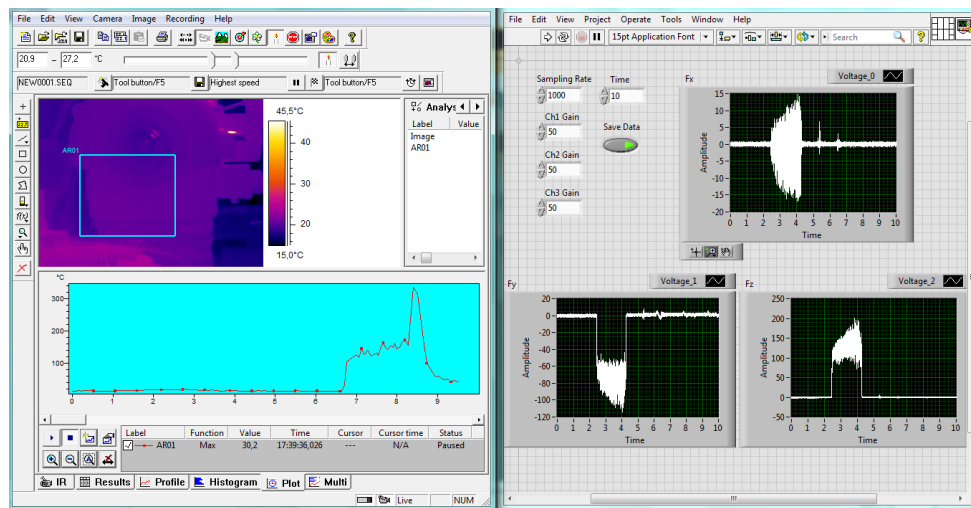


Figure 77: Sample thermal camera measurement along with force measurement

For these reasons, temperature measurements were made on the thermocouple in this part; various raw data are shown in Figure 78 below;

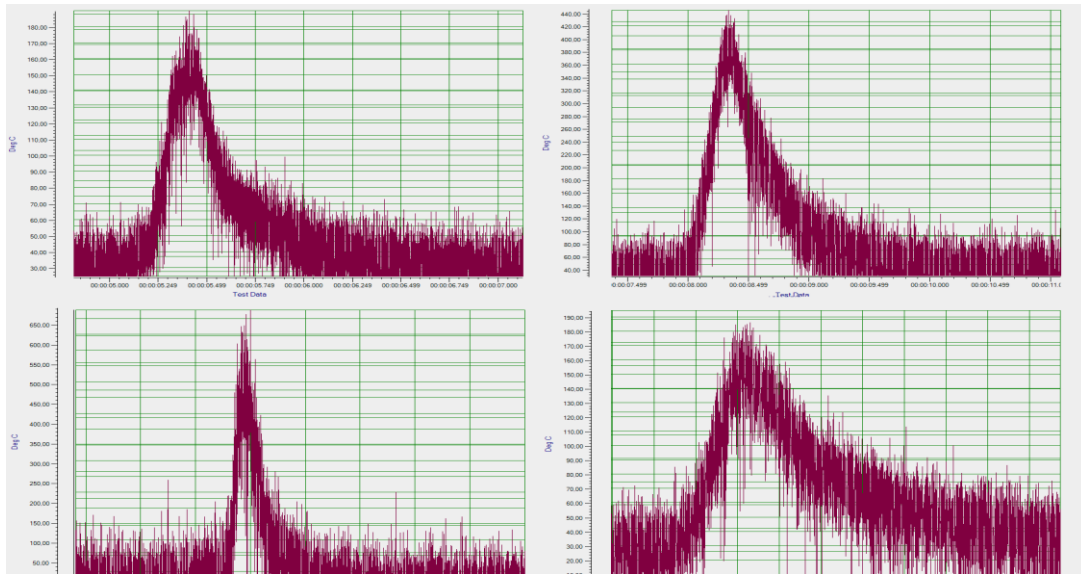


Figure 78: Thermocouple measurements raw data

In this study, main temperature measurements were made on super abrasive grinding operations. Total energy obtained by the calculated force and friction coefficient values and this energy distributed over the workpiece by the heat partitioning model. The heat flow comparison between experiment base calculation and model base calculation for CBN01 operations shown in Figure 79.

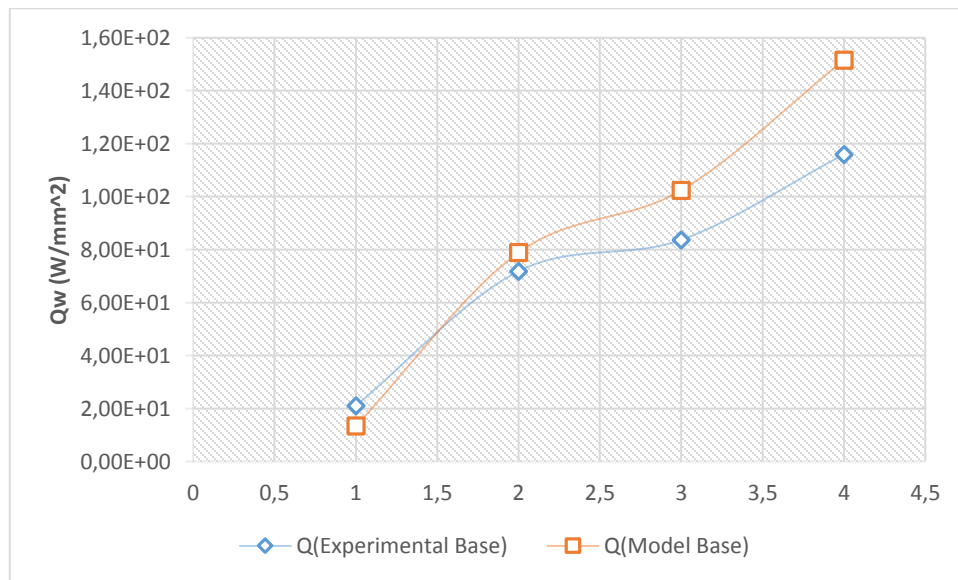


Figure 79: Heat flow comparison between experimental and model base calculations

Following temperature calculations were made with the obtained heat flow values on moving heat source temperature distribution model depending on thermocouple positions. Inconel 718 workpiece was machined with CBN01 wheel grinding conditions and temperature measurements were collected on the ground surface with grinding until the tip of the thermocouple was conducted. Comparative data is shown in Figure 80.



Figure 80: Comparison of CBN01 with Inconel 718 Temperature measurements and predictions

In the next test, CBN03 grinding conditions were used for AISI1050 steel with different depth of cut. Temperature model and experimental data comparison were made in the following Figure 81.

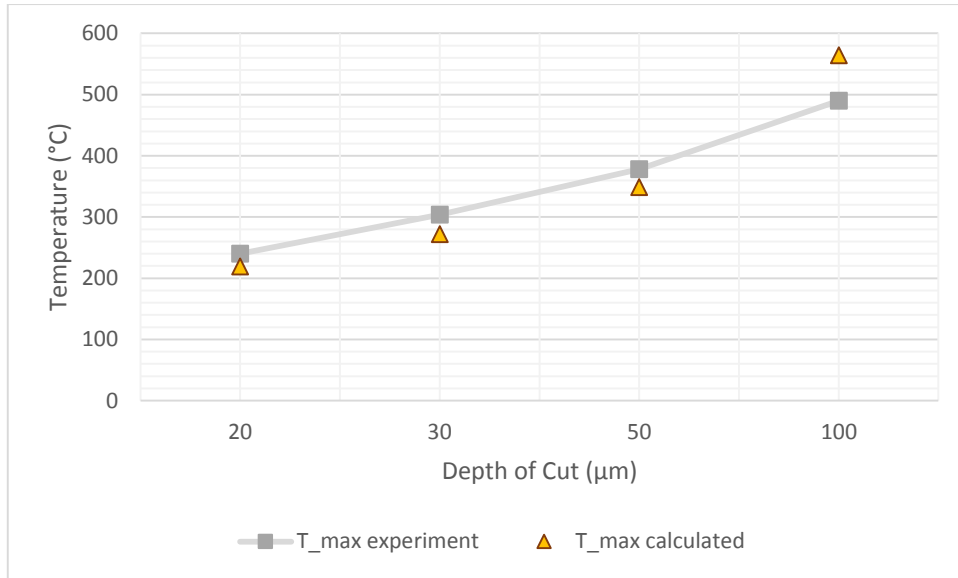


Figure 81: Comparison of CBN03 with AISI1050 temperature measurements and predictions

The temperature distribution in the workpiece was examined with different thermocouple z position beneath the grinding zone with the test setup of CBN03 conditions with 100-micrometer depth of cut.

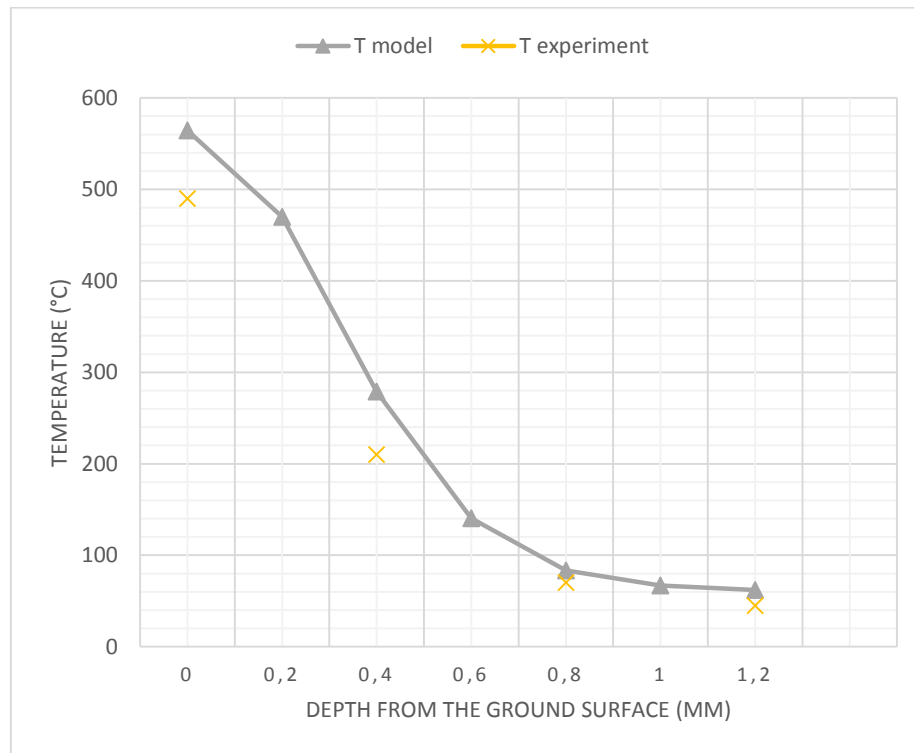


Figure 82: Temperature distribution at various z depth beneath surface

It can be deduced that depth of cut is more effective than workpiece velocity for process temperature since the large specific energy is required for deeper cutting. Total energy for material removal increasing results in greater temperature rise on the workpiece.

Thermal aspects of conventional and super-abrasive wheels investigated with Inconel 718 and AISI1050 steel workpiece and CONV01 and CBN01 wheels tests. Temperature results are shown in Figure 83.

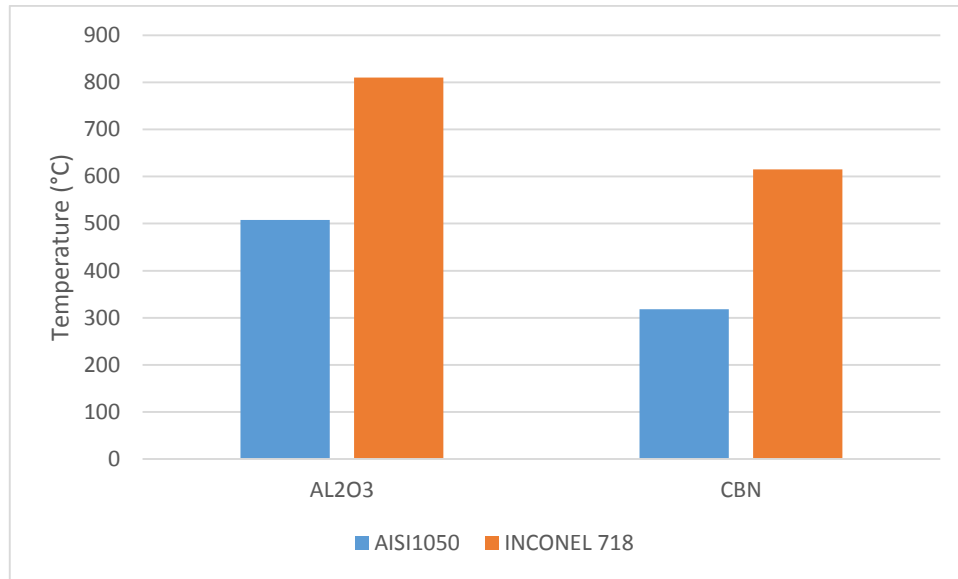


Figure 83: Comparison of different workpieces and wheels for temperature

The temperature was measured by changing the workpiece material and wheel while test conditions were constant. The parameters for the test were 50 microns depth of cut, 50 mm/min workpiece velocity. The results of the experiment also showed that there is less temperature increase on the workpiece in the CBN grinding. In addition, during the grinding of superalloy Inconel 718 more heat is generated compare to steel, which is due to the fact that it is harder to break crystal structure than steel and proportionally required stress for plastic deformation. Breaking these bonds release their energy in the form of heat. As a result, CBN wheels should be used in grinding operations where the low temperature on the workpiece is required.

Temperature predictions and experimental measurements are compared, and average error found around 20% and shown in Figure 84.

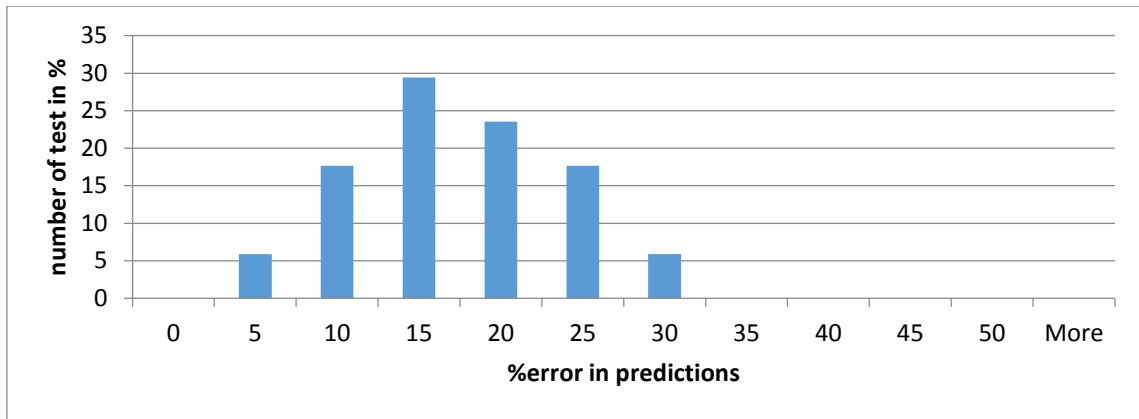


Figure 84: Error histogram between proposed model and experiments in temperature

In a general evaluation, proposed models are consistent with the results. On the other hand, the model can be improved with modeling of C parameter with the effect of cutting parameters and geometrical properties in the way of stochastically approach as in reality. It can be deduced that sliding friction should be investigated in more detail for more accurate results since, the error in the tangential direction is getting larger with workpiece velocity. The proposed solution procedure is working with acceptable errors for the surface grinding. Temperature distribution in the workpiece can be used for residual stress estimations, and geometrical approach can be used for surface roughness predictions in overall models. In the last part of the thesis force vibration for the thermomechanical model was investigated and modeled for insight information on the topic and it can be seen in appendix B.

In summary, iterative solution method of established force and temperature model has been proposed and verified by the experimental data in this section. As the contribution of this study, the initial temperature value of the thermomechanical force model in the grinding operation is solved with the minimum energy principle instead of the experimental data. In addition new experimental setup is established to measure temperature distribution along with workpiece. Results show that the established solution method gives reasonable outcomes within a margin of error. The obtained results show that the force is quite effective on temperature, workpiece velocity and the depth of cut is main reason of temperature rise on the workpiece.

6 SUGGESTIONS FOR FURTHER RESEARCH

Determination of C coefficient is significant in modeling, and it can be deduced that C is changing with corresponding cutting parameters according to experimental and model comparison. If it can be modeled with a geometric approximation, error margin of the predictions will considerably decrease.

In the established force model, each grain can be investigated separately by stochastic application for all geometric properties. Thus, the consistency of the model data will increase.

The whole wheel can be modeled with reverse engineering via 3D laser scanner technology. The 3D scanning technology is still developing, and it is not quite compatible with small parts as grains. However, it can be used to the understanding of the geometry of the grinding wheel more realistically.

In the force model, stagnation point investigation can be performed via orthogonal cutting tests with CBN negative rake angle tools. Third deformation zone model for negative rake angle investigation is still non-existence at the literature and crucial for the micro grinding operations.

In the thermal approach, cooling effects of the dimensional geometry of the part and the cooling fluid can be developed to increase working range of the model and precision of the results.

During temperature measurements, the workpiece is deformed with blind holes for thermocouples and also it is very challenging to get consistent results from thermocouple measurements. PVD film method can be applied for temperature measurement with the advantages of sensitive measurement and adaptable into the very small area.

Process optimization can be investigated with the combination of temperature, force and surface roughness models within the different wheel, workpiece and grinding parameters via optimization methods.

7 RESULTS AND DISCUSSIONS

In this study up-grinding single grain trochoid trajectory is applied with rotational and linear movement of the wheel. Uncut chip thickness, which is critical parameter for process modeling, calculation was made based on this approach. Comparison between conventional and trochoid path approaches show that trochoid should be considered with low wheel diameter over depth of cut ratio like creep feed grinding and micro grinding. However the conventional assumption is still valid for normal grinding operations, since the diameter over depth is high.

Established thermomechanical force model is adapted into surface grinding operations with the milling analogy. Observed friction coefficients are roughly between 0.2 and 0.4 which is much lower than turning and milling operations since the negative rake angle cause it. Another crucial point was the calibration of the coulomb friction coefficient, which is observed from literature data and non-cutting tests. Moreover, the essential point was the initial temperature values for the shearing zone and it is achieved via iterative temperature solution as described in solution procedure. After the calculation of single grain force, it is applied on the grinding zone. Grinding zone is calculated via geometric model and active cutting grains are obtained via model described in appendix A. Obtained process forces are verified through different grinding conditions and different grain properties of wheels. Results show that the main parameter is the workpiece material and grain material. Nonetheless, grain properties are effective on the process parameters. The error margin of the experimental verifications show that the proposed models are quite suitable to observe process forces. However, it should be remind that the assumptions for the models,

measurement errors and calibration of inputs resulted in errors, but it is acceptable in machining case.

Temperature model is created based on the force values obtained in thermomechanical force model. Required power is calculated with the obtained process forces, friction coefficients and user input cutting speed. Total heat flow is calculated with the required power over grinding zone which is calculated by geometrical model. It can be deduced that when contact area increase total heat flow will decrease. Heat partitioning model is used on grain size interaction. It shows that the material properties of the cutting particle is crucial on heat distribution. Maximum temperature rise is lower when CBN wheels are used since the CBN wheels thermal diffusivity almost twice of AL₂O₃. When thermal diffusivity of grain materials is compared to tungsten carbide, it can be seen that why heat is accumulated on the tool in conventional machining. Moreover, the heat partitioning on grinding operations are depended on the grinding parameters. When spindle speed is increased, workpiece heat ratio will increase since the time of contact zone decrease. As in the same mechanism resulted in that increasing depth of cut lower the heat partitioning into workpiece.

Temperature distribution solution is applied via moving heat source theory with obtained heat flow into workpiece. Moving heat source solution applied with the combination of analytical Bessel solution and numerical approach. Bessel solution is similar to constructed equation but not in exact, on the other hand numeric solution has singularity problems. The singularity problems caused by the boundary conditions of the moving heat source equations. It should be considered that the time parameter should be used lower than 0.01 and w parameter should start from 0.005 instead of 0 to obtain consistent results. Calculations and verifications showed that these initial conditions gives accurate results. Another issue was the heat flow distribution which has been usually taken as triangular or uniform. In this study heat flux model is developed in parabolic approach to supply consistency with the reverse engineered observations. Temperature distribution solution is implemented with the established heat flux model on moving coordinate. Simulation results show that the maximum temperature occurs at mid line of grinding zone. Results show that effective temperature rise beneath the surface is effective on thin band which is around 0.5 mm.

Experimental setups and investigations are proposed with advantages and disadvantages. Measurement method for geometrical properties of the abrasive grains are proposed throughout optical topography device. The workpiece is designed for temperature distribution measurements. Thermocouple usage and noise elimination is investigated with data acquisition device. When applying fixation with used method; epoxy should be applied as thin as possible at the tip of thermocouple to achieve accurate results. Thermal camera usage is investigated on surface grinding operations, but the results are quite different than thermocouple measurements since the temperature difference between mid-point and wall as described above. Moreover, the emissivity value is constant in program and it is affected by the vision angle in reality. Different types of materials and wheels are tested in various grinding conditions for verification of the models.

8 CONCLUSIONS

As I have argued that thermomechanical approach is the most comprehensive model that enables the wide use of analytical process modeling. It has been observed that the model is highly dependent on the generated temperature in the deformation zone since thermal dependence of material mechanical properties. In this context, temperature model is established which depends on not only the forces but also the contact length, workpiece velocity, friction coefficient, wheel and workpiece material dependent heat partitioning values. Temperature distribution on the workpiece analytically represented and the solution procedure is proposed with the combination of a solution of Bessel's function and numerical solution of it. 3D time-dependent temperature distribution solution is obtained with the adaptation of heat flux distribution on grinding zone. Geometrical, force and temperature models are combined to predict process parameters within the scope of minimization of calibration and experimental data. Process parameters obtained by models are verified through the experiments. The results show that the iterative solution of temperature and force models allows better calculation of process parameters. In this study, I have suggested why the thermal aspect is necessary for analytical process modeling especially in grinding operations.

Specific contributions of the presented study are listed as follows:

The thermomechanical approach is improved with geometric uncut chip thickness calculation with proposed trochoid path model.

The moving heat source theory is solved with estimation of the new heat flux distribution inspired by reverse engineering estimation to predict temperature distribution more realistically.

Time-dependent 3D solution is represented with a full solution instead of quasi-state, steady state or until maximum temperature solution in the literature.

The initial temperature value in the thermomechanical model is proposed with the combination of these three models in iterative solution procedure, and process parameters can be predicted more accurately.

REFERENCES

- [1] Yao CF, Jin QC, Huang XC, Wu DX, Ren JX, Zhang DH, "Research on surface integrity of grinding Inconel 718," *Int J Adv Manuf Technol*, vol. 65, no. (5–8), p. 1019–1030, 2013.
- [2] Ezugwu EO, Wang ZM, Machado AR, "The machinability of nickel-base alloys: a review," *J Mater Process Technol*, vol. 86, no. 1–16, 1998.
- [3] Pavel R, Srivastava A, "An experimental investigation of temperatures during conventional and CBN grinding," *Int J Adv Manuf Technol*, vol. 33, no. 3-4, pp. 412-418, 2007.
- [4] Hasuda Y, Handa A, Kobori Y, Kinebuchi S, Furusawa T, Harigaya Y, "Grinding of super-alloys using metal-bonded CBN wheel," *Key Eng Mater*, vol. 523–524, p. 143–148, 2012.
- [5] Brinksmeier, E., Aurich J., "Advances in Modelling and Simulation of Grinding Processes," vol. 55, pp. 667-696, 2006.
- [6] Lindsay, R. P., "The effect of parameter variations in precision grinding," *ASME, J. of Eng for Ind.*, vol. 92, p. 683, 1970.
- [7] Fan X, Miller M., "Force analysis for grinding with segmental wheels. Machining Science and Technology," *An International Journal*, vol. 10, pp. 435-455, 2006.
- [8] Hahn, R. S., "On the nature of the grinding process," in *Proceedings of the Third International Conference on Machine Tool Design and Research*, Birmingham, 1962.
- [9] R.P., Lindsay, "The Effect of Contact Time on Forces, Wheelwear Rate and G-ratio during internal and external Grinding," *Annals of the CIRP*, vol. 33, no. 1, p. 193, 1984.
- [10] Outwater JO, Shaw MC, "Surface temperature in Grinding," *Trans ASME*, vol. 74, pp. 73-86, 1952.
- [11] Malkin, Stephen, *Grinding Technology: Theory and Applications of Machining with Abrasives*, Society of Manufacturing Engineers, 1989.
- [12] R.L. Hecker, I.M. Ramoneda, S.Y. Liang, "Analysis of wheel topography and grit force for grinding process modeling," *J Manuf Process*, vol. 5, p. 13–23, 2003.
- [13] T. Siebrecht, D. Biermann, H. Ludwig, S. Rausch, P. Kersting, H. Blum, A. Rademacher, "Simulation of grinding processes using finite element analysis and geometric simulation of individual grains," *Prod Eng*, vol. 8, p. 345–353, 2014.
- [14] Shaw, M, "Fundamentals of Grinding," in *Proceeding of the International Grinding Conference: New Developments in Grinding*, Pittsburgh, Pennsylvania, 1972.
- [15] De Pellegrin DV, Corbin ND, Baldoni G, Torrance AA, "Diamond particle shape: its measurement and influence in abrasive wear," *Tribol Int*, vol. 42, pp. 160-168, 2008.

- [16] Komanduri R, Shaw MC, "Attritious wear of silicon carbide," *ASME Paper*, vol. 75, 1975.
- [17] Gilormini, P., Felder, E., "Theoretical and experimental study of the ploughing of a rigid-plastic semi-infinite body by a rigid pyramidal indenter," *Wear*, pp. 195-206, 1983.
- [18] Qi, H. S., Rowe, W. B. and Mills, B., "Experimental investigation of," *Tribology International*, vol. 30, no. 4, pp. 283-294, 1997.
- [19] J., Verkerk, "The Real Contact Length of Cylindrical Plunge Grinding," *Annals of the CIRP*, vol. 24, no. 1, p. 259, 1975.
- [20] Zhang L, Ge PQ, Zhang JH, Zhang Q, "Study on hardness depth variation of different grinding zone in grind-hardening," *Adv Mater Res*, vol. 24, no. 25, pp. 333-336, 2007.
- [21] Lindsay, R. P., "The Effect of Contact Time on Forces; Power and Metal Removal Rate in Precision Grinding," in *International Grinding Conference Society of Manufacturing Engineers*, Dearborn, Mich, 1984.
- [22] Rowe, W. Brian, *Principles of Modern Grinding Technology*, 2nd Edition, Liverpool: Advanced Manufacturing Technology and Tribology Research Laboratory, 2013.
- [23] Tönshoff H., Peters, "Modelling and Simulation of Grinding Processes," *CIRP Annals – Manufacturing Technology*, vol. 41, pp. 677-688, 1992.
- [24] Y. Liu, A. Warkentin, R. Bauer, Y. Gong, "Investigation of different grain shapes and dressing to predict surface roughness in grinding using kinematic simulations," *Journal of the International Societies for Precision Engineering and Nanotechnology*, vol. 37, pp. 758-764, 2013.
- [25] Hecker R, Liang S, Wu X., "Grinding force and power modeling based on chip thickness analysis," *Int. Journal of Advanced Manuf. Tech.*, vol. 33, pp. 449-459, 2007.
- [26] I.D. Marinescu, W.B. Rowe, B. Dimitrov, H. Ohmori, *Tribology of abrasive machining processes*, Netherland: Elsevier, 2012.
- [27] P. V. Vinay, C. S. Rao, "Grinding Mechanics and Advances -A Review," *Journal of Mechanical Engineering and Technology*, vol. 5, no. 2, 2013.
- [28] Badger, J. A. and Torrance, A. A., "A computer program to predict grinding forces from wheel surface profiles using slip-line fields.," in *Proceedings of the Conference in Advanced Manufacturing Technologies*, San Sebastian, 1998.
- [29] Snoeys, R. and Decneut, A., "Review of results of the co-operative research program of the CIRP grinding group," *Annals of the CIRP*, vol. 19, pp. 507-512, 1971.
- [30] Lee, K. C., Huang, H. P. and Lu, S. S., "Burr detection by using vision," *International Journal of Advanced Manufacturing Technology*, vol. 8, pp. 275-284, 1993.

- [31] S. Malkin, C. Guo, Grinding technology: theory and application of machining with abrasives, USA: McGraw-Hill, 2008.
- [32] Tang, J., Du, J. and Chen, Y., "Modeling and experimental study of grinding forces in surface grinding.," *Journal of Materials Processing Technology*, vol. 209, pp. 2847-2854, 2009.
- [33] Kapoor, A., "A re-evaluation of the life to rupture of ductile metals by cyclic plastic strain," *Fatigue Fract. Eng. Mater. Struct.*, vol. 17, pp. 201-219, 1994.
- [34] Torrance, A. A. and Buckley, T. R., "A slip line field model of abrasive wear," *Wear*, vol. 196, pp. 35-45, 1996.
- [35] Challen, J. M., Oxley, P. L. B., "An explanation of the different regimes of friction and wear using asperity deformation models," *Wear*, vol. 53, pp. 229-243, 1978.
- [36] Oxley, P.L.B., *Mechanics of Machining, an Analytical Approach to Assessing Machinability*, England: Ellis Horwood Limited, 1989.
- [37] Umbrello D, Ambrogio G, Filice L, Shivpuri G, "A hybrid finite element method-artificial neural network approach for predicting residual stresses and the optimal cutting conditions during hard turning of AISI 52100 bearing steel," *Mater Des*, pp. 873-883, 2008.
- [38] Umbrello, D., Saoubi, R., Outeiro, J.C., "The influence of Johnson–Cook material constants on finite element simulation of machining of AISI 316L steel," *Int. J. Machine Tools & Manufacture*, vol. 27, pp. 462-470, 2007.
- [39] Lin, Z.C., Pan, W.C., Lo, S.P., "A study of orthogonal cutting with tool flank wear and sticking behavior on the chip-tool interface," *J. Mat. Proc. Tech*, vol. 52, pp. 524-538, 1995.
- [40] E. Ozlu, A. Molinari, E. Budak, "Two-Zone Analytical Contact Model Applied to Orthogonal Cutting," *Journal of Machining Science and Technology*, pp. 323-343, 2010.
- [41] Molinari, A.; Moufki, A., "The Merchant's model of orthogonal cutting revisited: A new insight into the modeling of chip formation," *Int. J. Mech. Sci.*, vol. 50, pp. 124-131, 2008.
- [42] Molinari, A.; Dudzinski, D., "Stationary shear bands in high speed machining," *Comptes Rendus Acad. Sci.*, pp. 399-405, 1992.
- [43] Moufki, A.; Molinari, A.; Dudzinski, D., "Modelling of orthogonal cutting with a temperature dependent friction law," *J. Mech. Phys. Solids*, vol. 46, no. 10, pp. 2103-2138, 1998.
- [44] Kalpakjian, S., *Manufacturing process for engineering materials*, Menlo Park, California: Addison-Wesley, 1997.
- [45] Tawakoli, T.; Azarhoushang, B.; Rabiey, M., "Ultrasonic assisted dry grinding of 42CrMo4.," *International Journal of Advanced Manufacturing Technology*, vol. 42, pp. 883-891, 2009.

- [46] D.K. Zhang, C.H. Li, D.Z. Jia, Y.B. Zhang, X.W. Zhang, "Specific grinding energy and surface roughness of nanoparticle jet minimum quantity lubrication in grinding," *Chin J Aeronaut*, vol. 28, no. 1, pp. 570-581, 2015.
- [47] Benkai Li, Changhe Li, , Yanbin Zhang, Yaogang Wang, Dongzhou Jia, Min Yang, "Grinding temperature and energy ratio coefficient in MQL grinding of high-temperature nickel-base alloy by using different vegetable oils as base oil," *Chinese Journal of Aeronautics*, vol. 29, no. 4, pp. 1084-1095, 2016.
- [48] Kohli, S., Guo, C., Malkin, S., "Energy partition to the workpiece for grinding with aluminum oxide and CBN abrasive wheels," *Journal of Engineering for Industry Transactions of the ASME*, vol. 117, no. 2, pp. 160-168, 1995.
- [49] Lavine, A.S., Malkin, S., Jen, T.C., "Thermal Aspects of Grinding with CBN Abrasives," *Annals of the CIRP*, vol. 38, no. 1, pp. 557-560, 1989.
- [50] MC, Shaw, "A simplified approach to workpiece temperatures in fine grinding," *Annals CIRP*, vol. 39, no. 1, pp. 345-347, 1990.
- [51] Rowe, W.B., Black, S.C.E., Mills, B. Qi, H.S., "Analysis of grinding temperatures by energy partitioning," *Proc. Inst. Mech Eng*, vol. 210, pp. 579-588, 1996.
- [52] Jaeger, J. C., "Moving sources of heat and temperature at sliding contacts," *Royal Society of New South Wales -- Journal and Proceedings*, pp. 203-224, 1942.
- [53] Hou ZB, Komanduri R, "General solutions for stationary/moving plane heat source problem in manufacturing and tribology," *Int J Heat Mass Transfer*, vol. 43, pp. 1679-1698, 2000.
- [54] Malkin, S., and Guo, C., "Thermal Analysis of Grinding," *CIRP Annal*, vol. 56, pp. 760-782, 2007.
- [55] Lin, Wen Liang Kuo . Jen Fin, "General temperature rise solution for a moving plane heat source," *Int J Adv Manuf Technol*, vol. 31, pp. 268-277, 2006.
- [56] Des Ruisseaux NR, Zerkle RD, "Thermal analysis of the grinding process," *J Eng for Ind Trans ASME*, vol. 92, pp. 428-434, 1970.
- [57] González–Santander, J.L., "Analytic solution for maximum temperature during cut in and cut out in surface dry grinding," *Applied Mathematical Modelling*, vol. 40, no. 1, pp. 2356-2367, 2016.
- [58] Lavine, A.S., "An Exact Solution for Surface Temperature in Down Grinding," *Int. Journal of Heat Mass Transfer*, vol. 43, pp. 4447-4456, 2000.
- [59] Tahlivian, A.M., Champliaud, H., Liu, Z., Hazel, B., "Study of Workpiece Temperature Distribution in the Contact Zone During Robotic Grinding Process Using Finite Element Analysis," in *8th CIRP Conference on Intelligent Computation in Manufacturing Engineering*, Procedia CIRP, 2013.

- [60] Kato T, Fujii H, "Temperature measurement of workpiece in surface grinding by PVD film method," *J Manuf Sci Eng*, vol. 119, pp. 689-694, 1997.
- [61] Dehao Liu, Gang Wang, Zhenguo Nie, Yiming (Kevin) Rong, "An in-situ infrared temperature-measurement method with back focusing on surface for creep-feed grinding," *Measurement*, vol. 94, pp. 645-652, 2016.
- [62] JV, Beck, "Thermocouple temperature disturbances in low conductivity materials.," *J Heat Transfer*, vol. 84, pp. 124-132, 1962.
- [63] Bin Shen, Guoxian Xiao, Changsheng Guo, Stephen Malkin and Albert J. Shih, "Thermocouple Fixation Method for Grinding Temperature Measurement," *J. Manuf. Sci. Eng*, 2008.
- [64] Peklenik, J., "Determination of geometrical and physical parameters for basic grinding research," in *TH Aachen*, Aachen, 1957.
- [65] Hou, Z., Komanduri, R., "On the Mechanics of the Grinding Process – Part I. Stochastic Nature of the Grinding Process," *International Journal of Machine Tools and Manufacture*, vol. 43, pp. 1579-1593, 2003.
- [66] Abdalslam Darafon, Andrew Warkentin, Robert Bauer, "3D metal removal simulation to determine uncut chip thickness, contact length, and surface finish in grinding," *Adv Manuf Technol*, vol. 66, p. 1715, 2013.
- [67] Darafon, A., Warkentin, A., Bauer, R., "Characterization of grinding wheel topography using a white chromatic sensor," *International Journal of Machine Tools and Manufacture*, vol. 70, pp. 22-31, 2013.
- [68] Aslan, Deniz and Kocafe, Mert and Budak, Erhan, "Modeling of surface grinding operation with circumferentially grooved wheels," in *UTIS 2014*, Bursa, 2014.
- [69] Abdalslam Darafon & Andrew Warkentin & Robert Bauer, "3D metal removal simulation to determine uncut chip thickness, contact length, and surface finish in grinding," *Int J Adv Manuf Technol*, 2012.
- [70] P. Koshy, A. Iwasaki, M.A. Elbestawi, "Surface generation with engineered diamond grinding wheels; Insight from simulation," *CIRP Annals - Manufacturing Technology*, vol. 52, no. 1, pp. 271-274, 2007.
- [71] Park, H. W., Liang, S, Y., "Force Modeling of Microscale Grinding Process Incorporating Thermal Effects.," *International Journal of Advanced Manufacturing Technology*, vol. 44, pp. 476-486, 2009.
- [72] Basuray, P. K., Misra, B. K., Lal, G. K., "Transition from ploughing to cutting during machining with blunt tools," *Wear*, vol. 43, no. 3, pp. 341-349, 1977.

- [73] Ikawa, N., Shimada, S., Tanaka, H., Ohmori, G., "Atomistic analysis of nanometric chip removal as affected by tool-work interaction in diamond turning," *Palo Alto*, vol. 40, pp. 551-554, 1991.
- [74] Y. Ichida, "Fractal Analysis of Micro Self-Sharpening Phenomenon in Grinding with Cubic Boron Nitride (cBN) Wheels," in *Scanning Electron Microscopy*, 2012, pp. 953-978.
- [75] Lin, G.C.I, Oxley, P.L.B., "Mechanics of Oblique Machining: Predicting Chip Geometry and Cutting Forces from Work Material Properties and Cutting Conditions.," *Proceedings of the Institution of Mechanical Engineers*, vol. 186, pp. 813-820, 1972.
- [76] Russel, J.K., Brown, R.H., "The Measurement of Chip Flow Direction," *International Journal of Machine Tool Design and Research*, vol. 6, pp. 129-138, 1966.
- [77] Zorev, N.N, *Metal Cutting Mechanics*, Pergamon Press, 1966.
- [78] Whitfeld, R.C., *A Mechanics of Cutting Approach for the Prediction of Forces and Power in Some Commercial Machining Operations*, Melbourne: PhD Thesis, 1986.
- [79] Erhan Budak, Emre Ozlu, Hayri Bakioglu, Zahra Barzegar, "Thermo-mechanical modeling of the third deformation zone in machining for prediction of cutting forces," *CIRP Annals - Manufacturing Technology*, vol. 65, no. 1, pp. 121-124, 2016.
- [80] Zorev, N. N., "Inter-relationship between shear processes occurring along tool," *International Research in Production*, pp. 42-49, 1963.
- [81] Childs, T.H.C., "Friction modeling in metal cutting," *Wear*, vol. 260, pp. 310-318, 2006.
- [82] Rabinowicz, E., *Friction and Wear of Materials: Second Edition*, New York: Wiley-Interscience, 1995.
- [83] Olsson, M., Soderberg, S., Jacobson, S., Hogmark, S., "Simulaton of cutting tool wear by a modified pin-on-disc test," *Int. J. Mach. Tools & Manufacture*, vol. 29, no. 3, pp. 377-390, 1989.
- [84] Fang N., "Slip-line modeling of machining with a rounded-edge tool – Part 1," *Journal of the Mechanics and Physics of Solids*, vol. 51, pp. 715-742, 2003.
- [85] E. B. E. Ozlu, "Thermomechanical Modeling of Orthogonal Cutting Including the Effect of Stick – Slide Regions on the Rake Face," in *10th CIRP International Workshop on Modeling of Machining Operations*, Calabria, Italy, 2007.
- [86] J. C. Maxwell, *Theory of Heat*, London: Longmans Text-Books of Science, 1871.
- [87] K., Kadirgama and M. M., Noor and K. V., Sharma, "Tool Life and Wear Mechanism when Machining Hastelloy C-22HS," *Wear*, vol. 270, no. 3-4, pp. 258-268, 2011.
- [88] C. T. 96, "<http://www.wzl.rwth-aachen.de/>," 10 07 2015. [Online]. Available: <http://www.wzl.rwth-aachen.de/en/3c799d2a5ff42216c125740c003913ba/Binary3.gif>.

- [89] Morgan, M.N., Rowe, W.B., Black, S.C.E., Allonson, D.R., "Effective thermal properties of grinding wheels and grains," *Proc. Inst. Mach. Eng.*, vol. 212, no. B, pp. 661-669, 1998.
- [90] Zishan Ding, Beizhi Li, Omar Fergani, Yamin Shao, Steven Y. Liang, "Investigation of Temperature and Energy Partition During Maraging Steel Micro-grinding," *Procedia CIRP*, vol. 56, pp. 284-288, 2016.
- [91] Miroslav Neslušán, Ivan Mrkvica, Robert Čep, Pero Raos, "Heat Distribution when Nickel Alloy Grinding," *Technical Gazette*, vol. 19, no. 4, pp. 947-951, 2012.
- [92] Stephen Malkin, Changsheng Guo, *Grinding Technology: Theory and Application of Machining with Abrasives*, Industrial Press Inc, 2008.
- [93] J. F. Archard, "Contact and Rubbing of Flat Surfaces," *Journal of Applied Physics*, vol. 24, 1953.
- [94] T.M.A. Maksoud, "Heat transfer model for creep-feed grinding," *Journal of Materials Processing Technology*, vol. 168, pp. 448-463, 2005.
- [95] M. Vashista, S. Paul, "Effect of process parameters on convective heat transfer coefficient of fluid and heat partitioning in high efficiency deep grinding with water based coolant," in *India Manufacturing Technology, Design and Research Conference*, Assam, 2014.
- [96] Filice, L., Micari, F., Rizutti, S., and Umbrello, D., "A critical analysis on the friction modeling in orthogonal machining," *Int. J. Mach. Tools & Manufacture*, vol. 47, pp. 709-714, 2007.
- [97] G.Q Cai, B.F Feng, T Jin, Y.D Gong, "Study on the friction coefficient in grinding," *Journal of Materials Processing Technology*, vol. 129, no. 3, pp. 25-29, 2002.
- [98] Lan Yan, Zhi Xiong Zhou, Feng Jiang, X.K. Li, Yi Ming Rong, "Grain-Workpiece Interaction Study of Grinding Process through Single Grain Cutting Simulation," *Machining and Advanced Manufacturing Technology*, vol. 432, pp. 269-272, 2010.
- [99] A.O. Mohamed, R. Bauer, A. Warkentin, "Application of shallow circumferential grooved wheels to creep-feed grinding," *Journal of Materials Processing Technology*, pp. 700-706, 2013.
- [100] R. S. H. a. R. P. Lindsay, *Principles of Grinding*, new York, N.Y.: Machinery Magazine, 1971.

APPENDICES

APPENDIX A – Active grain percentage with random grain distribution

Active grain calculation take a step with creating stochastic grain cluster on wheel based on static measurements of grain properties. Static grain number is used to create each grain with normal distribution of height within average and standard deviation measurements. When the cluster is created each grain trajectory is calculated with geometrical formulations. After that, each trajectory intersection points are checked whether they are in contact or not. First each contact with workpiece is counted and secondly each intersection between grains are checked to decide which one is active. After that point active grain percentage is calculated in the predicted grinding zone. Results show that the main parameter is the feed speed for defining C number for different test conditions. Simulation results for feed speed is shown below;

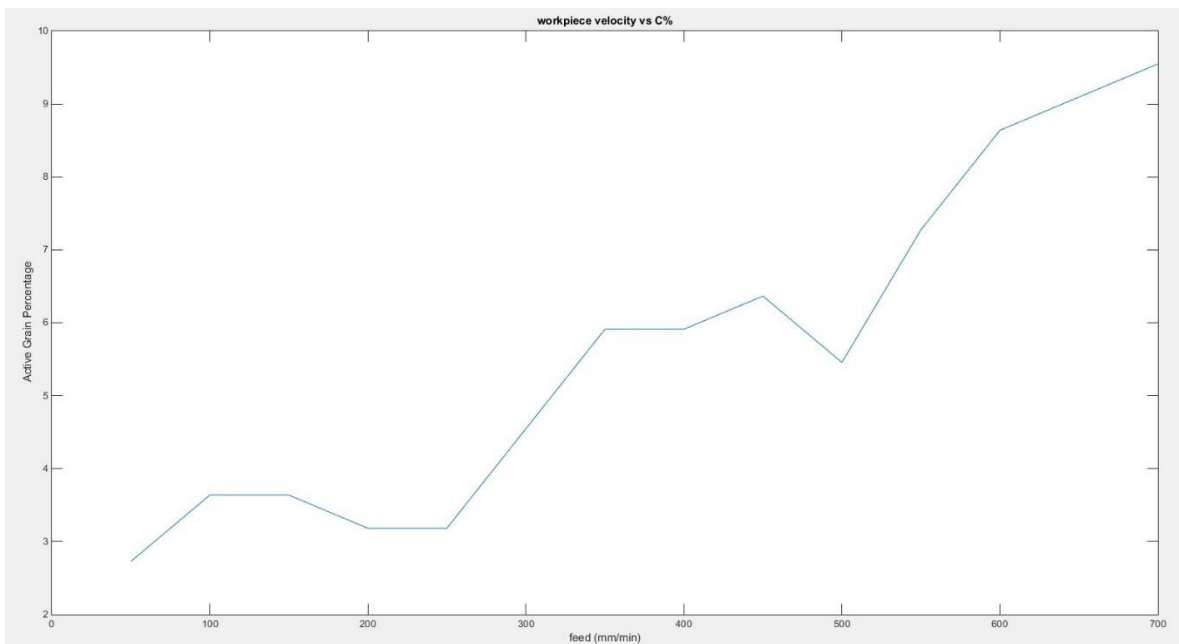


Figure 85: Active Grain Percentage vs Feed

Pseudo code of the simulation is shown with following flow chart;

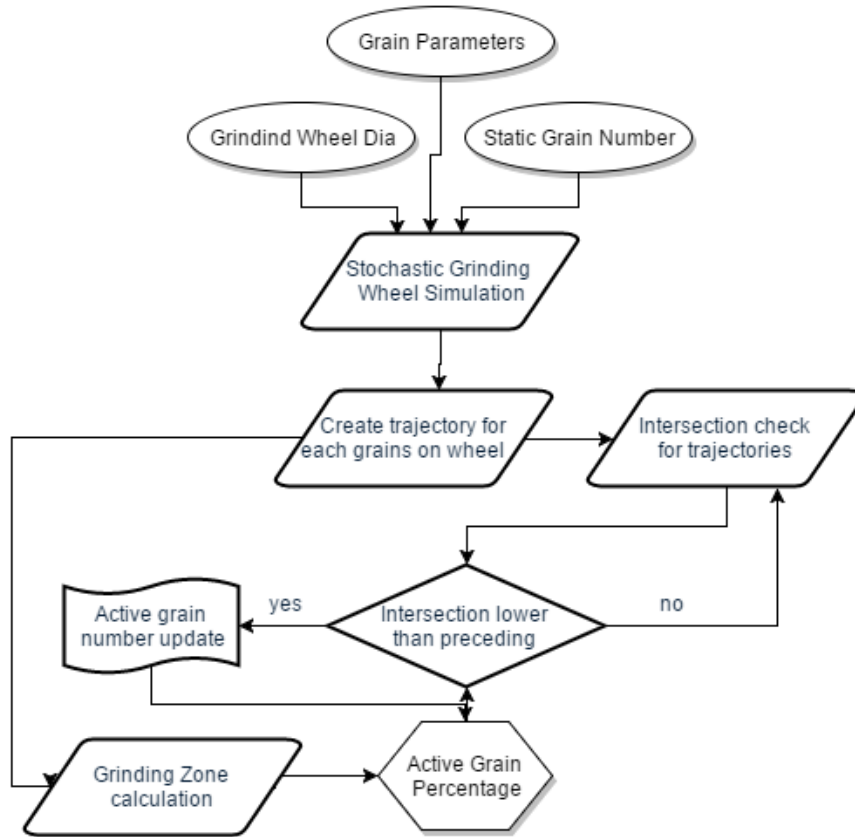


Figure 86: Active Grain Flow Chart

APPENDIX B – Force vibration for grinding

In this study milling time domain force vibration is adapted into thermomechanical force model. It is based on dynamic deflection model. Force is coming from the thermomechanical force model and it cause to deflection. Deflection is calculated in x and y directions and resultant deflection is effects uncut chip thickness. X direction displacement is multiplied with sinus immersion angle and y direction displacement is multiplied with cosines immersion angle to find normal direction vibration value. Following flow chart is used to simulate force vibration in thermomechanical force model.

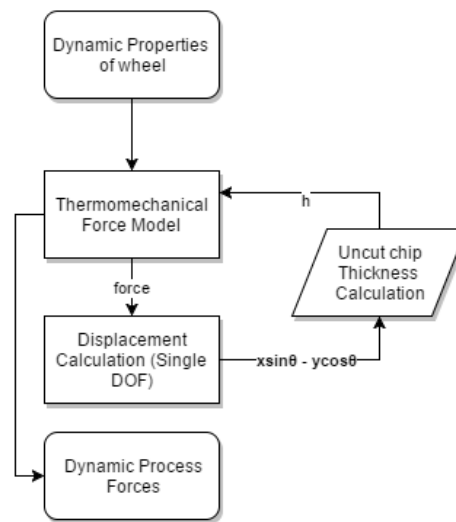


Figure 87: Force vibration flow chart

Parameters are selected as follows for dynamic properties.

kx	8,00E+04
zeta _x	0.02
wn _x	500*2*pi
ky	8,00E+04
zeta _y	0.02
wn _y	500*2*pi

Figure 88: Dynamic properties

And the resultant force and deflections are given in below figures for corresponding parameters.

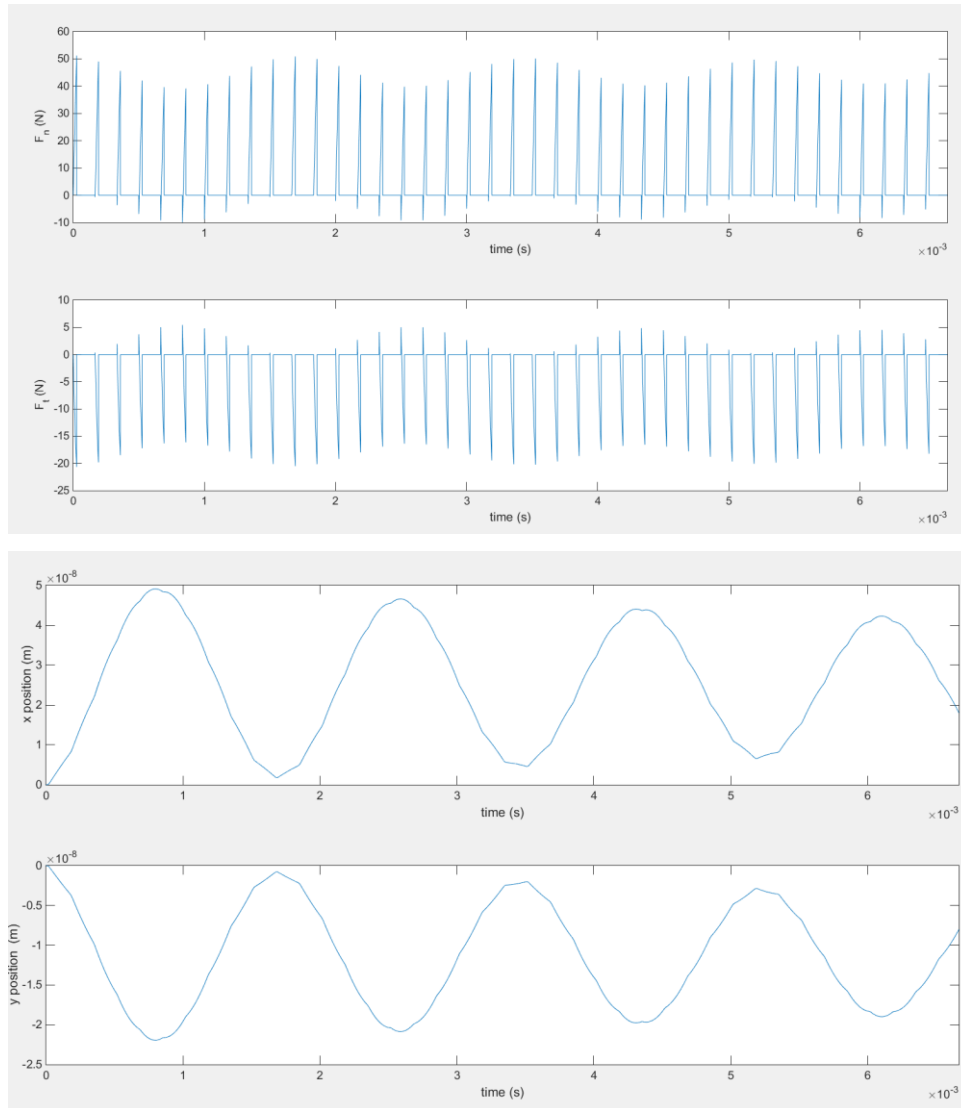


Figure 89: Force vibration on force and deflection

If stiffness of the system increase, vibration effect will be lower as with following parameters;

kx	8,00E+04
zetax	0.05
wnx	900*2*pi
ky	8,00E+04
zetay	0.05
wny	900*2*pi

Figure 90: Dynamic properties

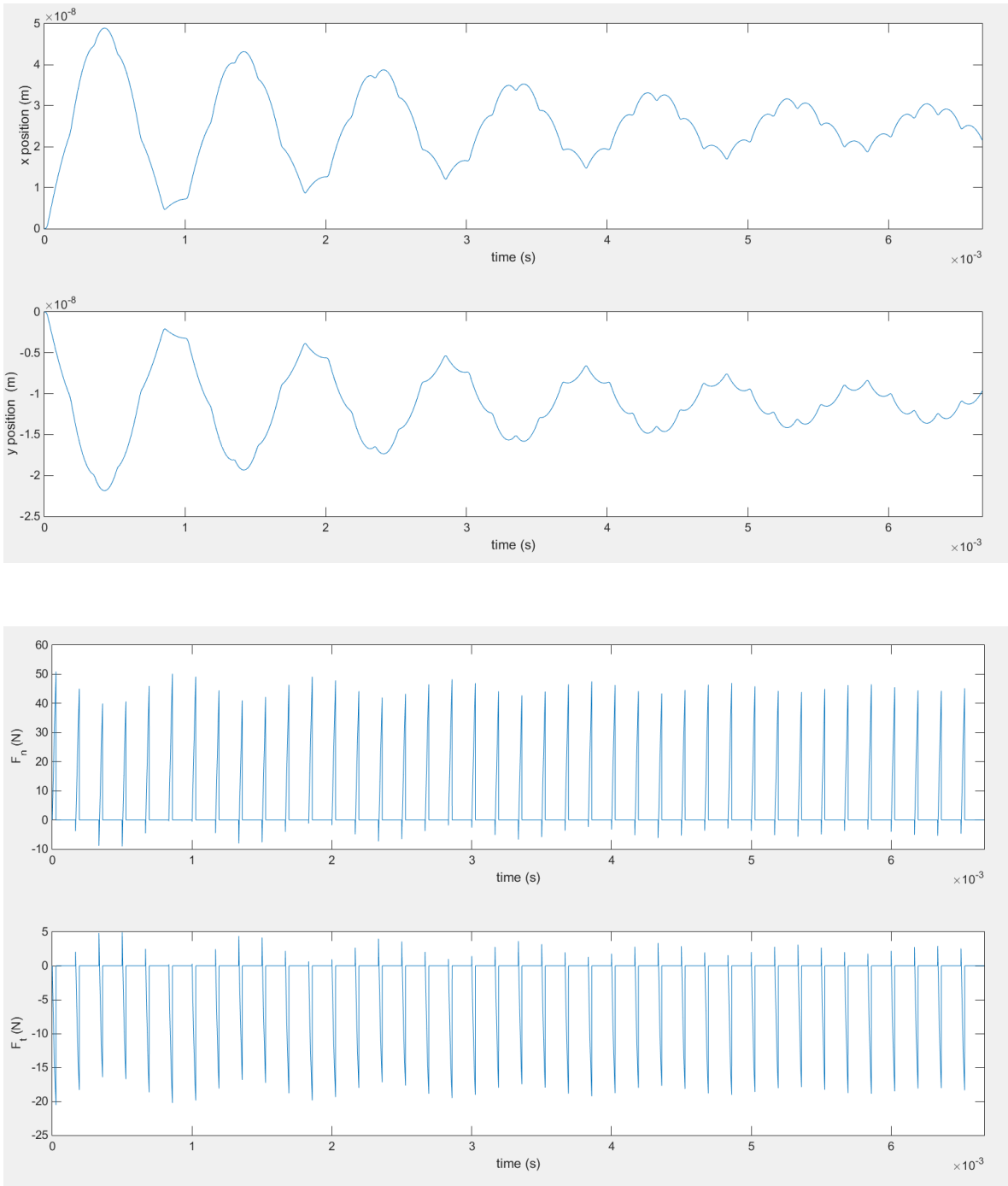


Figure 91: Force vibration on force and deflection